EXPERIMENTAL STUDY OF HYPERGOLIC IGNITION BY DROPLET COLLISIONS

DAWEI ZHANG

PhD

The Hong Kong Polytechnic University

2018

The Hong Kong Polytechnic University
Department of Mechanical Engineering

Experimental Study of Hypergolic Ignition by Droplet Collisions

DAWEI ZHANG

A thesis submitted in partial fulfillment of the requirement for the degree of Doctor of Philosophy

December 2017

CERTIFICATE OF ORIGINALITY

I hereby declare that this thesis is my own work and that, to the best of my knowledge and belief, it reproduces no material previously published or written, nor material that has been accepted for the award of any other degree of diploma, except where due acknowledgement has been made in the text.

_____ _____(Signed)

Zhang Dawei (Name of student)

Abstract

Hypergolic ignition induced by binary droplet collisions of propellants of WFNA/TMEDA and H_2O_2/Ethanolamine solution of $NaBH_4$, and the dynamics of droplet collision of the shearing thinning non-Newtonian liquids have been experimentally studied in the present thesis. A new set of experimental system has been designed and established, in which two special types of droplet generators were in-house made and integrated together with the precisely controlling system to ensure the stable collision of droplets of hypergolic propellants with high chemical activity. A method based on the grayscale levels on the shadowgraphs was developed and employed to calculate the collision conditions and also to help describe the ignition process. The ignition delay time is determined by applying this method in high accuracy.

The hypergolic ignition by head-on collision of TMEDA/WFNA droplets is firstly studied and phenomenologically described based on five stages. A monotonic dependence of IDT on We has been identified and explained by the non-monotonic occurrence of jet-like internal mixing patterns. The droplet size ratio was discovered to affect the ignition by influencing both the mixing and the equivalence ratio. Non-monotonic dependence of IDT on B also is identified and explained as the competence between stretching and reflexive

impact inertia. Droplet size effects on the hypergolic ignition was experimentally studied and theoretically analyzed through multiple time-scaling analysis. Two contradictory effects are identified that when the droplet size is diminishing, on one hand, the heating period will be shortened tending to lead to a shorted IDT; on the other hand, the vaporization will be weakened due to the enhancement of heat lost. As been found, It may even lead to non-ignitability if the droplet size continues decreasing. Similar phenomena exhibit in the collision of droplets of hydrogen peroxide and ethanolamine solution of sodium borohydride. The internal reaction of H_2O_2/Ethanolamine solution of $NaBH_4$ within the merged droplet could be clearly observed during the pre-ignition period. The reaction products would first generate and expand inside the merged droplet and then break through droplet surface before ignition. Non-Newtonian effect of the droplet collision of with shear thinning Carbomer aqueous solution is not obvious at moderate range of We but will exhibits at larger value of We when plashing happens. In the off-center collisions, a distinct strap-shape bouncing regime and exclusive stretching separation modes are exhibiting, caused by the non-Newtonian effect.

Publications

Journals

1. D. Zhang, P. Zhang, Y. Yuan, T. Zhang, Hypergolic ignition by head-on collision of N, N, N′, N′ − tetramethylethylenediamine and white fuming nitric acid droplets, *Combustion and Flame*, 173 (2016) 276-287.

2. D. Zhang, C. He, P. Zhang, C. Tang, Mass Interminglement and Hypergolic Ignition of TMEDA and WFNA Droplets by Off-center Collision, Combustion and Flame, Accepted.

Conference

1. D. Zhang and P. Zhang, Hypergolic Ignition Induced by Binary Collision of TMEDA and WFNA Droplets: Non-monotonic Effects of Impact Parameter, The 11th Asia-Pacific Conference on Combustion, 2017, Sydney.

2. 张大尉，张鹏，四甲基乙二胺和白色发烟硝酸液滴碰撞点火延迟的实验研究，中国工程热物理学会－燃烧学术年会，2016，马鞍山。

Acknowledgement

The author would like to express his deepest gratitude and highest respect to his chief supervisor, Dr. Peng Zhang, not only for the interesting and carefully selected research topics, but more importantly, for his rigorous attitude and strict requirements to academic research, which has encouraged the author's confidence and led him on the right track of research. His great mentorship and guidance will be profoundly influence the author in both career and life.

The author is also grateful to Prof. Chih-Yung Wen and Prof. Chun-Wah Leung for their encouragements and insightful suggestions to the author's research.

A special acknowledgement to all the students and staff in Dr. Zhang's Fundamental Combustion Research Laboratory, who created a perfect environment for intellectual development and personal life.

The author is sincerely grateful to Prof. Fan's group in the Institute of Mechanics, Chinese Academy of Sciences for their generous support of both equipment and technology in my experiments in Beijing. What memorable days!

Special thanks to my family, friends and people showing loving cares for me!

Contents

Table of Figures

1. Overview

1.1 Hypergolic ignition

Being of great relevance to many fundamental and practical problems, the ignition of propellants plays an essential role in the rocket engines[1-4] which are more vulnerable than other types such as internal combustion engine and gas turbine engines. In a rocket engine, reactants, fuel and oxidizer, are contained in high concentration to achieve extremely elevated level of temperature within a limited chamber size. Therefore, improperly timed ignition could result in objectionable events or even lead to destruction to the rocket engine.

In terms of ignition in rocket engine, it should be noted that the governing physical mechanisms at start, e.g. at ambient conditions, are distinct from those governing the flame initiation under steady-state circumstance[1]. The heterogeneous ignition process at start follows the process of injection of propellants from injectors into cold chamber. We consider in what follows only the issues of ignition at start.

According to the characteristics of ignition events in rocket engine, it is reasonable to describe ignition by distinguishing the propellants into two broad general categories[1]: (1) hypergolic propellants that ignite spontaneously after the fuel and oxidizer contact with each other without any source of external energy, and (2) non-hypergolic propellants that

are inert under standard injection conditions and require an external source of energy to initiate the reaction.

In fact, the substantial difference between the hypergolic and non-hypergolic propellants is the condensed-phase chemical reaction rate between the fuel and oxidizer under the condition where they mix[3]. Particularly, the hypergolic fuel and oxidizer as, with low reactivation energy, react quickly enough at the temperature they mix together so that the heat released from the reactions could lead the propellants to the condition that can be described as an ignition. While the reaction rate for non-hypergolic propellants at ambient temperature is much slower than that for hypergolic propellants such that the limited amount of heat generated from the reactions will be lost to the cold surroundings as quickly as it is liberated. The temperature of non-hypergolic propellants therefore cannot increase appreciably so that the reaction rate remains the level that can never lead the propellants to ignition if there is no external heat source. However, the non-hypergolic propellants could be transformed into hypergolic ones once they are set at appropriate contact conditions. For example, if the non-hypergolic kerosene-liquid oxygen is set into an environment with sufficiently high temperature, they will also ignite spontaneously after some certain time delay, because the chemical reaction between kerosene and oxygen will turn to be violent enough herein and the heat is not readily lost to the warmed surroundings.

Based on the discussion above, the non-hypergolic propellants could be regarded as that, at ambient temperature and pressure, it will take infinite long time for them to get to the ignition, while the infinite long time would be shortened to measurable ones if one appropriately changes the contact condition or elaborately prohibits any heat lost to the surroundings. Therefore, for the present study, it is an investigation focusing on the time duration from the moment of contact of the fuel and oxidizer to that when ignition happens rather than on the ignition phenomenon itself.

As already known, for the phenomenon of ignition there should be an inducting period before the violent chemical reaction taking place. Once ignition occurs, the temperature starts to go up very sharply within a much shorter time period than the inducting period. It is hence reasonable to believe that it is of little difference for choosing various properties to describe occurrence of ignition.

Various criterions are employed in defining the ignition time. The definition based on the thermal runaway is mathematical definition embedded within activation energy asymptotics. Other experimental definitions include the time at which a sufficient high temperature reaches or specific rate of increase of temperature exhibits, and the time at which luminous radiant output is first observed or radiation in a selected wavelength is detected [5].

Hereto, it has already been known that the main distinction between hypergolic and non-hypergolic propellants is reaction rate at ambient temperature. For hypergolic propellants, the reaction is violent enough to 'bootstrap' themselves to ignition, otherwise is the non-hypergolic ones. In fact, hypergolic propellants are always regarded as to be very suitable for some special requirement in the rocket or spacecraft engines in simplifying the engine design, allowing restart, performing multiple pulses and easily controlling orbit and attitude of rockets[4].

1.2 Binary droplet collisions

Droplet collision is always regarded as frequent event especially downstream the injectors where there is a high density of small fuel and oxidizer droplets. Recent interests in gelled hypergolic propellants (GHP) [14, 15, 34] further signify the study of hypergolic ignition by droplet collision. Because of the reduced vapor pressure of propellants by gelling, the ignition of GHPs can be only triggered in liquid phase after a succession of fluid-dynamical processes: the collision, the coalescence and the mixing of the fuel and oxidizer droplets. It is nevertheless known that a collision of two liquid droplets unnecessarily results in a coalescence, which in turn cannot warrant a sufficient and rapid mixing within the coalesced droplet. Consequently, it is worthwhile to briefly summarize

the current understanding in droplet collision dynamics, especially those pertinent to the droplet internal mixing, in the following subsection.

Being of importance in understanding many industrial and natural processes, binary droplet collision in a gaseous medium has been a subject of considerable interest for decades [35, 36]. The majority of earlier experiment research was focused on identifying various collision outcomes of two identical droplets and on their variation with the controlling parameters: the collision Weber number, *We*, measuring the relative importance of droplet inertia compared with its surface tension, and the impact parameter, *B*, characterizing the deviation of droplet trajectories from the head-on condition. For water, alkanes and alcohols, five distinct collision outcomes are effected by varying *We* and *B*: (I) coalescence after minor deformation, (II) bouncing, (III) coalescence after substantial deformation, (IV) coalescence followed by separation for near head-on collision (a.k.a. reflective separation with small *B*), and (V) coalescence followed by off-center collision (a.k.a. stretching separation with large *B*). Droplet splattering occurs at the higher *We*s, often over a thousand, which are infrequently encountered in real engine conditions [35].

Theoretical efforts have been made to understand the experimental observations. Zhang and Law [37] developed a comprehensive theory to explain the nonmonotonic transitions from Regime (I) to (II) and from (II) to (III). The theory reveals that the

occurrence of droplet coalescence or bouncing depends on whether or not the clearance between the impacting interfaces can reach the critical range (typically tens of nanometers) of the van der Waals force before the droplets have totally lost the translational kinetic energy of their relative motion. Several contributing physical factors, such as the rarefied nature of the intervening gas flow between the droplets, the viscous dissipation of the droplet internal motion, and the van der Waals force between the droplet interfaces, were identified and incorporated into the theory. Various models have also been proposed to explain the transition between Regime (III) to (IV) [6-8] and the formation of satellite droplets for Regime (V)[38, 39] . The viscous dissipation through the internal motion of merged droplet was found to suppress the droplet separation and therefore stabilize the droplet.

The ambient pressure influences the collision outcomes[8, 40]. Specifically, droplets tend to bounce back with increasing the ambient pressure because the increased inertia of the gas film separating the droplets becomes more resistant to be drained out to effect the interface merging [41]. By the same token, droplets tend to coalesce with decreasing the ambient pressure. For instance, bouncing is absent for water droplets at atmospheric pressure but present at reduced pressures; coalescence is present for n-tetradecane droplets at atmospheric pressure but absent at elevated pressures.

The size ratio, Δ, usually defined by the ratio of the diameter of the bigger droplet to that of the smaller one, affects substantially the collision outcomes. Previous studies [7, 37, 42] have demonstrated that droplet separation is suppressed and hence droplet coalescence is promoted by increasing the size ratio. It is known that droplet separation occurs, at relatively high Weber numbers, when the surface tension of the temporarily coalesced droplet cannot hold the excess kinetic energy of the collision. Increasing the size ratio tends to increase the viscous dissipation within the coalesced droplet, which stabilizes the droplet by dissipating the excess energy.

The effects of liquid viscosity on the collision outcomes, particularly on suppressing the droplet separation through the viscous dissipation, were observed by Jiang et al. [6] and Qian and Law [8], and further confirmed and characterized in subsequent studies [38, 43, 44]. The Volume-of-Fluid simulation of Dai and Schmidt [44]on the head-on collision of equal-size droplets shows that the dependence of the dissipated energy and the maximum deformation on the collision Reynolds number decreases with increasing the Reynolds number up to 200. Their results suggest that the viscosity effect on the maximum deformation becomes insignificant at sufficiently high Reynolds number. The experiments of Gotaas et al. [38] on the collision of equal-size droplets of wide ranges of viscosity from 0.9×10^{-3} kg/(m·s) to 48×10^{-3} kg/(m·s) and the Weber number from 10 to 420 show that the

transition Weber number for the droplet separation linearly increases with the Ohnesorge number (Oh) for the droplets with Oh<0.04 and exponentially increases with the Oh for the highly viscous droplets with Oh>0.04.

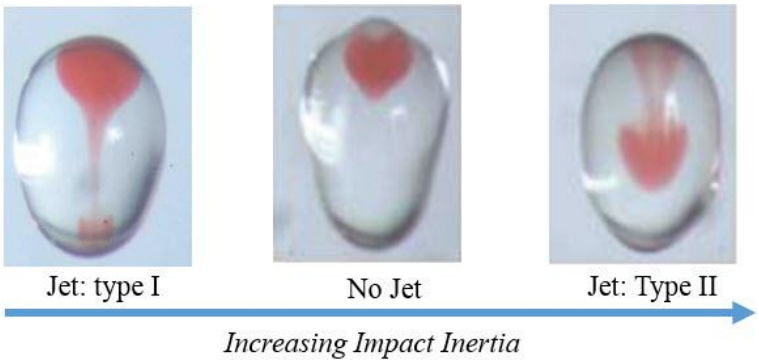

Figure 1.1 Experimental images (adapted from [35]) of the head-on collision of unequal-size water droplets, showing the non-monotonic emergence of jet-like mixing patterns. The size ratio is fixed at 2.5 and the Weber numbers from left to right are 4.7, 8.1 and 28.7, respectively.

Another important aspect of droplet coalescence is the subsequent internal mixing, which has gained increasing attentions in recent years for its relevance in the microfluidics and hypergolic propellant systems involving liquid-phase reactions [45-51]. An important understanding gained from the recent studies is that the internal mixing is minimal for the head-on collision of two identical droplets due to the intrinsic symmetry across the collision plane. Effective mixing requires breaking the symmetry by introducing differences between the droplets to either surface tensions, or viscosities, or diameters. Tang et al. [48] investigated experimentally and numerically the internal mixing of unequal-size droplets and identified the jet-like mixing patterns varying with *We* and Δ, as shown in Fig. 1.1. For

droplets with a relatively small viscosity (for example, water and n-decane), the internal mixing in the coalesced droplet is facilitated by the emergence of jet-like patterns at small and large Weber numbers, and however such jet-like mixing patterns do not develop at intermediate Weber numbers. Mechanically, the jet formation at small *We*s is driven by the capillary pressure difference of the droplets; it is suppressed by the substantial droplet deformation at intermediate *We*s; it reemerges at large *We*s due to the droplet stretching in the direction of the large impact inertia. In addition, the jet-like mixing is enhanced by increasing the size ratio because it favors the concentrated impact inertia of the smaller droplet. The jet-like mixing is suppressed for liquids with large viscosities (for example, n-tetradecane) that reduce the impact energy through viscous dissipation.

Several inferences of the above understanding on droplet coalescence and mixing can be drawn for hypergolic ignition by droplet collision. First, hypergolic ignition may favor relatively low ambient pressures because droplet coalescence is the prerequisite for the subsequent droplet mixing but it is suppressed at elevated pressures. Second, hypergolic ignition may favor a large size disparity for enhanced droplet coalescence and mixing. Third, hypergolic ignition may vary significantly with *We* because the degree of droplet mixing depends on *We* non-monotonically through the jet-like mixing patterns. It is also

noted that these inferences may be reformed when droplet collision and mixing are coupled with chemical reactions.

1.3 Hypergolic propellant fuels and oxidizers

Traditionally, the most widely used hypergolic fuel is hydrazine and its derivative such as Monomethylhydrazine (MMH, CH_3NHNH_2) due to their appropriate physical and thermal characteristics, and also due to their violent chemical reaction with the oxidizers such as NTO and HNO_3[12, 13]. However, strong carcinogenicity of hydrazine and MMH and fierce corrosivity of HNO_3 make the hypergolic propellants troublesome for maneuverability and dangerous to the human beings as well as the vulnerable devices.

The demand for safely operating propellants but do not sacrifice the ignition and combustion performance has been increasing during the last decades. One promising solution is to gel the toxic and corrosive hypergolic propellants by the shear thinning gelling agents[14-16]. The behavior of these types of non-Newtonian gellants under no or low shear resembles as solid, while it becomes similar to pure liquid under large level of shear tress force. As results, the gelled propellants are easily to be stored and handled, reducing the probability of leakage hazard, through the advantage of solid-like property and also gain the ability to suspend energetic metal additives. Meanwhile, the hypergolic

ignition property still remains since they perform as liquid propellants when injected into the chamber under large level of shear stress. Nevertheless, although the gelled propellants would be squeezed into liquid-like form from the solid-like status at storage, the mixing of gelled propellants droplets should be quite different with that within the originally pure liquid propellants because the viscosity of non-Newtonian fluid is changing all the time. Therefore, the interaction and mixing mode between the droplets with non-Newtonian properties and the hypergolic ignition induced by the collision of such gelled propellant droplets merits efforts to be studied.

Another way to avoid the issue of poisonousness and corrosion of hypergolic propellants is to use the more 'friendly', alternative fuels or oxidizers. TMEDA has been tested as an alternative, 'green' hypergolic propellant for future rocket and missile engines to replace the acutely toxic and potentially carcinogenic hydrazine and its derivatives. Compared with the widely-used MMH, TMEDA remains as a liquid in a wider range of temperatures and is 8.4 times less toxic based on the LD_{50} data, and therefore reduces the threat of its vapor exposure to the personnel and environment during its storage and handling. Furthermore, when used with nitric acids (NA) as the oxidizer, such as RFNA and WFNA, TMEDA has comparable specific impulses, density impulses and ignition delays, making TMEDA an attractive MMH substitute.

Compared with the extensively studied MMH and other amines, the TMEDA/NA system was recently investigated in only a few theoretical and experimental studies. McQuaid et al. [52, 53] performed the ab initio quantum chemistry and molecular dynamics studies of various multi-amines and correlated the advantageous hypergolicity of TMEDA to the orientation of its amino lone pair electrons. The density functional theory (DFT) study of Liu et al. [54] identifies two key reactions affecting the ignition delay of TMEDA/NA: the exothermic proton transfer reaction from NA to TMEDA to form the dinitrate salt, TMEDADN, in liquid phase,

$$\mathrm{TMEDA} + 2\mathrm{HNO_3} \rightarrow \mathrm{TMEDADN}, \quad (1)$$

and the subsequent gas-phase reactions between TMEDA and NO_2, the major product from the thermal decomposition of NA. The important role of the exothermicity of liquid-phase reactions in determining the hypergolic ignition delay was also confirmed by Zhang et al.[55], whose DFT study employs eight different theoretical methods to compare the TMEDA/NA system with that of 2−azido−N,N−dimethylethanamine (DMAZ) and NA.

Dambach et al. [32] conducted drop contact tests and drop tests to study the hypergolic ignition of TMEDA/RFNA. Ignition was observed for all the drop tests but not for the drop contact tests, implying that the droplet impact promotes the ignition by

enhancing the mixing. Their drop contact tests also show that ignition does not occur when the volume ratios of TMEDA to RFNA are small.

Wang et al. [28, 56] used a confined interaction setup resembling the jet impinging apparatus and a drop test to study the hypergolic ignition of TMEDA with an NA of 90% purity. Their Fourier transform infrared spectrometry measurement of species confirms the existence of TMEDADN, which appears as a solid particulate cloud. The exothermic salt formation reaction was found crucial for the heat needed for evaporating the reactants, decomposing NA to NO_2, and the subsequent reactions of TMEDA and NO_2.

Recently, as the Space X Co. first achieved a successful landing and recovery of a first stage of rocket through their reusable rocket launch system[19, 20], pursuit of optimal propellants utilized for modern spacecraft propulsion have gained an increasing interest[21]. A number of green propellant were proposed and considered, among which the hydrogen peroxide (H_2O_2) is one of the most promising candidates. Being able to be used as an oxidizer in hypergolic bi-propellants and also as a monopropellant, H_2O_2 has been studied for rocket engine use for quite a few decades[22].

Historically, hydrogen peroxide has been displaced by other typies of propellants for an extended period due to the limited specific impulse (in the range of 165s-185s) [22]as well as the concerns of its storability since it is very reactive and thermodynamically

unstable even at the ambient conditions. The concerns of its storability however has always been debated. There is some certain amount of reports saying that hydrogen peroxide can used safely if handled appropriately. Moreover, as the recycling and reusable rocket concept has been brought to the forefront, the green propellant of hydrogen peroxide regains interest in the last 10 years[21].

Since H_2O_2 would decompose into gas phase oxygen even at the storable circumstance, the interaction and mixing of between the H_2O_2 and hypergolic fuel would be different with that in other types of hypergolic propellants. In addition, due to its active chemical characteristics, the characteristics of ignition where H_2O_2 serves as the oxidizer also should distinct with that by order types of oxidizers.

1.4 Scope of the study in present thesis

Based on the all considerations to the spontaneous ignition induced by the hypergolic propellants in terms of their droplet collisions with or without the gelling agents, the present thesis mainly consists of five parts: (1) experimental study of hypergolic ignition by the head-on collision of WFNA and TMEDA droplets; (2) experimental and numerical study of impact parameter effect within the droplet collision process on the hypergolic ignition; (3) experimental and theoretical study of droplet size effect on the

hypergolic ignition; (4) experimental study of dynamic characteristics of non-Newtonian droplet collisions and the hypergolic ignition by the gelled propellants droplet collisions; (5) experimental study of hypergolic ignition by the collision of hydrogen peroxide and the ethanolamine droplets.

2. Hypergolic Ignition by Head-on Collision of *TMEDA* and *WFNA* Droplets

2.1 introduction

Spontaneous ignition of a hypergolic propellant occurs upon the contact with an oxidizer without external heat sources such as flames, sparks, hot gases and surfaces [1-4]. Using hypergolic propellants in rocket engines simplifies the engine design, allows the engine restart, and thereby increases the engine maneuverability. In a typical rocket engine combustor, the initially separated liquid fuel and oxidizer are brought together to react by the impingement of fuel and oxidizer jets. A lapse can be detected between the first contact of fuel and oxidizer and the occurrence of ignition, which is often characterized by rapid heat release and possibly concomitant visible light emission. Unlike the autoignition of a homogeneous mixture of non-hypergolic reactants, which can be defined characterized as by a “rapid” rise of temperature or pressure, the hypergolic ignition is inherently a physicochemical process involving mixing and reactions in both liquid and gas phases, and its definition is usually descriptive and system-dependent.

Many experimental methods have been developed for studying the ignition process of hypergolic propellants from different aspects and comprehensively summarized in a few reviews [2, 3]. Fletcher and Morrell indicated that the fundamental difference among these

methods arises from the different modes of mixing [2]. The prevalent experimental methods are schematically shown in Fig.2.1(a)-2.1(d) in the order of approximately descending degree of premixing before reaction. Figure 2.1(a) schematizes the piston-driven apparatus, in which the reactants are rapidly mixed within a few milliseconds or less before being injected into a constant-volume reactor [23-26]. The observed ignition process is dominantly determined by chemical reactions and can be separated into three temporally sequential stages [3, 25, 26]: the first stage is the fast liquid-phase reactions yielding heat and gaseous species; the second stage is the relatively slow mixing and reactions in gas phase; and the third stage is the gas-phase ignition and combustion. Furthermore, the ignition delay is found to rely on the duration of the second stage, which is sensitive to the heat release from the liquid-phase reactions in the first stage. Figure 2.1(b) schematizes the impinging jet test, in which the fuel and oxidizer are partially premixed before they are injected by the impinging nozzles into a confined chamber [27-29]. This apparatus can be used to simulate various temperature, pressure and concentration conditions met in rocket engine combustors. Figure 2.1(c) schematizes the widespread drop test for prescreening potential hypergolic propellants [30, 31]. In the test, a fuel drop is made to impact a small amount of oxidizer pool in either a glass cuvette or a flat tray. The fuel and oxidizer have minimal premixing before their liquid-phase reactions occur. Figure 2.1(d) schematizes the

drop contact test, in which a suspended droplet of one propellant gradually approaches to an unrestrained pool of the other propellant [31-33]. Such a test was recently developed to resemble the hypergolic ignition initiated by droplet-droplet collisions with small impact inertia [31].

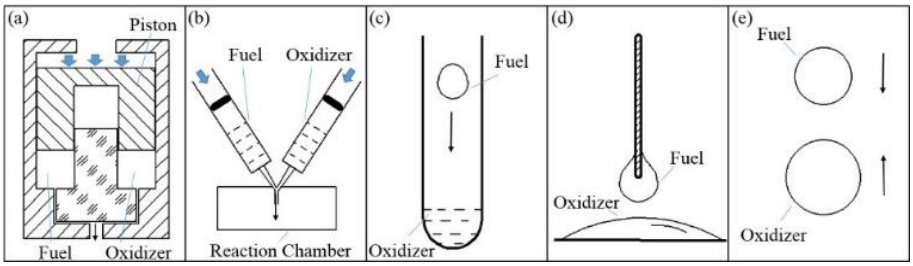

Figure 2.1 Schematic of experimental methodologies for hypergolic ignition in (a) a piston-driven apparatus with rapid mixing, (b) an impinging jet test, (c) a drop test, (d) a drop contact test, and by (e) binary droplet collision.

In spite of the worthy understanding in hypergolic ignition obtained with the experimental methods shown above, the influence of liquid-phase mixing in determining the ignition delay are either designedly eliminated from the rapid-mixing reactors, or partially suppressed in the impinging jet tests, or inseparably present in the drop tests. Moreover, it is difficult (if not impossible) to quantify the liquid-phase mixing in the drop tests because of the "wall effect" introduced by the cuvette walls, or the quartz rod or filament for suspending the droplet, or the surface supporting the unstrained liquid pool. In view of that the impinging jets of hypergolic propellants are atomized into droplets in rocket engine combustors, and that the frequent collisions of propellant droplets tend to

promote the liquid-phase fuel-oxidizer mixing and therefore the ignition, an experimental method-free from any wall effect as shown in Fig. 2.1(e)-for studying the hypergolic ignition initiated by the binary collision of droplets, as shown in Fig. 2.1(e), is desirable but has not been attempted.

The present experimental study attempts to study the hypergolic ignition by the binary, head-on collision of a smaller TMEDA droplet and a larger WFNA droplet in atmospheric air, with the emphasis on the influence of the collision parameters, such as *We* and Δ, on the ignition delays. Only head-on collisions (B=0) are considered in the study to avoid the additional complexity of off-center collisions ($B\neq0$), which merit future studies. Because unequal-size droplet collisions promote droplet coalescence and mixing, the size ratio is another crucial variable besides the Weber number. Furthermore, WFNA is used to minimize the intervention of other components contained in RFNA or in other NAs. We shall present the study as follows. The experimental apparatus and the measurement methods are expatiated in Section 2. The results for a representative case are presented in Section 3 to illustrate the hypergolic ignition processes. A *We*-Δ regime nomogram for the hypergolic ignitability is also presented in the section. The influences of *We* and Δ on the ignition delays are discussed in Sections 4 and 5, respectively, followed by concluding remarks, in Section 6.

2.2 Experimental Apparatus and Measurement Methodology

2.2.1 Droplet Collision Apparatus

The schematic of the droplet collision apparatus established for the present study is shown in Fig. 2.2. Droplets are generated by two independent droplet nozzles, (1) for WFNA and (2) for TMEDA, and collected by a tray (3). The nozzles are connected to the pressurized liquid tanks (4) and the pressure of pure nitrogen from the gas tank (5) is regulated by two SMC pressure reducing valves (6) with an accuracy of 0.1kPa and are powered by a 24V direct current (7).

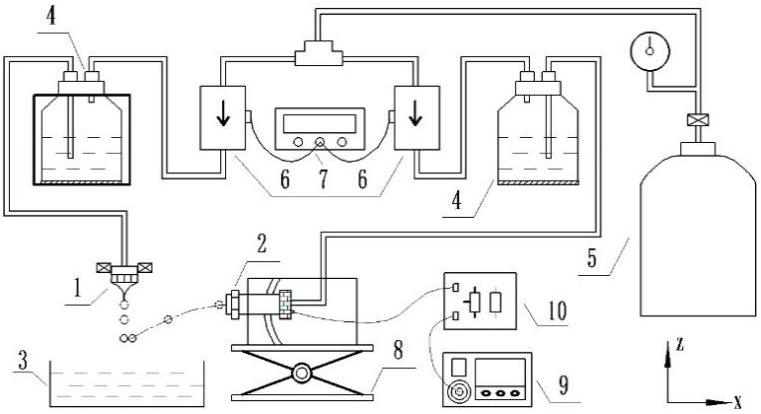

Figure 2.2 Schematic of the experimental apparatus for hypergolic ignition by binary collision of TMEDA and WFNA droplets. (1) WFNA droplet generator, (2) TMEDA droplet generator, (3) Collection tray, (4) Pressurized liquid tank, (5) Gas tank, (6) Pressure regulator, (7) DC power supply, (8) XYZ and angle displacement stage, (9) Function generator, (10) Controlling circuits.

The key component of the TMEDA droplet generator is an electromagnetically controlled micro valve, SMLD 300G, made by Fritz Gyger AG. The valve has a typical

response time of 400μs, a maximum dispensing frequency of 3000Hz, and a repeat accuracy of higher than 95%. The droplet generator is mounted on a micrometric *XYZ* stage (8) to precisely adjust the positions and angles of the dispensing TMEDA droplets. The droplet generator is triggered by a function generator with tunable time delays, so the droplet can be spatially and temporally regulated to collide with the WFNA droplet generated separately. The sizes of the TMEDA droplets vary from 0.5mm to 1.2mm in the present study and are mainly determined by the orifice diameter of the valve nozzle. The switch-on duration of the nozzle, which is controlled by the pulse generator (9) through a controlling circus (10), moderately affects the droplet size. The dispensing velocity of the TMEDA droplets can be changed with the nitrogen gas pressure through the pressure reducing valve (6).

Because WFNA is strongly corrosive to the SMLD 300G valve and other commercial droplet generators, a simple but functional droplet generation nozzle was designed and manufactured for the present study. The needle-shape nozzle with a diameter of 0.2mm is made of Teflon (Polytetrafluoroethylene) and mounted downwardly to generate WFNA droplets of 1.45 mm with a frequency of 2-3 Hz by the pressurized nitrogen gas. Once a WFNA droplet is collided by a TMEDA droplet, their motion will substantially deviate from the trajectories of the other WFNA and TMEDA droplets. As a

result, the droplet collision and subsequent ignition processes are not intervened by other droplets generated from the nozzles.

2.2.2 Measurement Methodology

The experimental setup for the shadowgraph imaging, photoelectric and infrared detections is shown in Fig. 2.3. The temporally resolved shadowgraph images are recorded by a Phantom V711 camera (1), with an imaging speed of 5000 frames per second. Each image consists of 1024 × 800 pixels and one pixel represents a physical two-dimensional grid of 20μm × 20μm. With the enlarging optical lenses, the camera is able to capture an about 4cm × 3cm region (one pixel represents 40μm×40μm), which is sufficiently large for observing the entire collision and ignition processes. A light-emitting diode (2) is placed oppositely to the high-speed camera as a back light source.

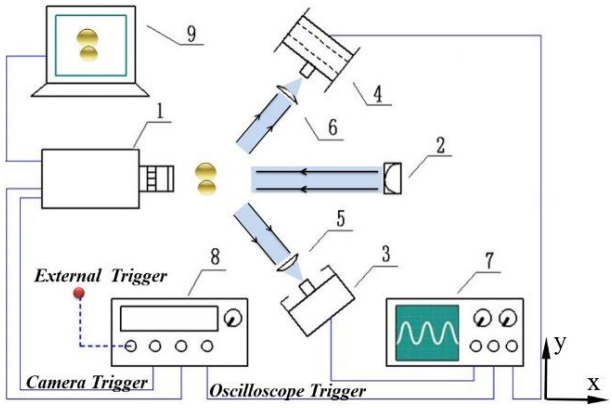

Figure 2.3 Schematic of experimental setup for visualizing the hypergolic ignition by time-resolved shadowgraph, visible light detection and infrared radiation detection. (1) High speed camera, (2) Light-emitting diode, (3) Photoelectric detector, (4) Infrared radiation detector,

(5) Plano-convex lens, (6) Infrared enhanced mirror, (7) Oscilloscope, (8) Pulse generator, (9) Computer.

Because the hypergolic ignition of TMEDA/WFNA is accompanied with luminous flames and a large amount of heat release, visible and infrared radiations are measured to detect the occurrence of the ignition. The THORLABS DET10A photodetector (3) has a wavelength range of 200nm ~ 1100nm and a rise time of 1ns. The liquid-nitrogen-cooled infrared detector (4) of Infrared Associates, Inc. has a wavelength of 2μm ~ 5μm and a response time of 1μs. It will be seen shortly that these two measurements with high responsivities provide validations to the ignition delay time determined by analyzing the time-resolved shadowgraph images.

The photodetector and the infrared detector are placed at the same horizontal level as that of the high-speed camera. The convex lens for visible lights (5) and the one with infrared antireflection coatings (6) are 2 inches in diameter. Synchronized with the high-speed camera and externally triggered by a pulse generator (8), the oscilloscope (7) collects and displaces the voltage signals from the visible light photodetector and the infrared radiation detector.

The diameters, the relative velocity and the collision impact parameter of the TMEDA and WFNA droplets are measured from the shadowgraph images, as shown in Fig. 2.4. The grayscale images of the shadow photographs are stored with a resolution of

8 bits per sample pixel, which results in 256 different grayscale levels for the shade of gray. The lowest level, 0, denotes the darkest and the highest level, 256, the brightest. With the average grayscale level set to be 100, the grayscale levels are lower than 5 in the region occupied by droplets and the opaque gaseous species, and are higher than 250 in the region occupied by luminous flames. The small, bright spots in the centers of the droplets are due to the light reflection.

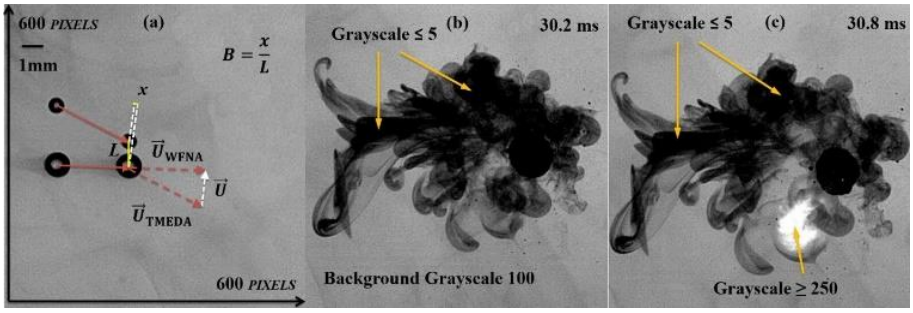

Figure 2.4 Grayscale level analysis of the representative shadowgraph images of the hypergolic ignition (a) before droplet collision, (b) before luminous flames appear, and (c) after luminous flames appear.

Because of the large difference of grayscale levels in the shadowgraph images, we can use the MATLAB software to count the grayscale level for each pixel, compute the local gradient of grayscale levels and identify the outmost edge of the droplet surface, where the largest gradients are obtained. Consequently, the droplet shape can be determined with an accuracy of one pixel and the measured droplet diameters have errors less than 7%, as the smallest droplet occupies about 15 pixels. The droplet velocity can be determined, within an error of 3%–8%, by locating the droplet center in five successive

images within 1.0 ms, and subsequently calculating and averaging the time derivatives of the coordinates of the droplet center. The impact parameter is defined by $B = x/L$, in which x is the projection of the separation distance L between the droplet centers in the direction normal to the relative velocity and can be determined after the velocities of the two droplets are obtained. In the present study, the impact parameter is controlled to be smaller than 0.1 to minimize the influence of off-center collisions.

2.3. Ignition Phenomena, Ignition Delay Time and Ignitability

2.3.1 Descriptions of Ignition Phenomena

The phenomena of the hypergolic ignition by the collision of a smaller TMEDA droplet and a larger WFNA droplet are described by using a representative case of $We = 60.9$ and $\Delta = 1.6$. Choosing WFNA as the excess propellant is suggested by the stoichiometry of the exothermic liquid-phase reaction (1) and have been used in previous drop tests [28, 56]. The Weber number is defined by $We = \rho_O D_O U^2/\sigma_O$ and the size ratio by $\Delta = D_O/D_F$, where ρ, σ, and D are the density, the surface tension and the diameter of the droplets; U is the relative velocity between the droplets; the subscript "O" denotes WFNA and "F" TMEDA. These nondimensional numbers are based on the physical properties of the WFNA droplet because D_O is fixed at 1.45mm in the present experiment.

Dimension analysis shows that the collision of two unlike, miscible droplets relies on not only *We* and Δ but also the Ohnesorge number, $Oh = \mu_O/\sqrt{\rho_O \sigma_O D_O}$; the density ratio, ρ_O/ρ_F; the viscosity ratio, μ_O/μ_F; the surface tension ratio, σ_O/σ_F; the gas-liquid density ratio, ρ_g/ρ_O; and the gas-liquid viscosity ratio, μ_g/μ_O. The fluid-dynamic effect of liquid viscosity, particularly on suppressing the droplet separation through the viscous dissipation of the droplet internal motion, can be characterized by either the Ohnesorge number or the Reynolds number, $Re = \rho_O D_O U/\mu_O$, but not both at the same time because they are interdependent by $Re = \sqrt{We}/Oh$ when *We* is given. As the physical properties of the two propellants, the ambient gas, and D_O are fixed in the present experiment, only *We* and Δ can be independently varied by changing the impact velocity and the size of the TMEDA droplet; the Ohnesorge number, $Oh = 2.5 \times 10^{-3}$, is fixed in the present study; $Re = \sqrt{We}/Oh$ varies accordingly with *We*; the other ratios are fixed as constant parameters.

For a unified description, we have introduced and presented the nondimensional time $T = t/t_{\mathrm{osc}}$ where $t_{\mathrm{osc}} = \sqrt{\rho_o R_o^3/\sigma_o}$is approximately the natural oscillation time of the WFNA droplet and is fixed at $3.3ms$ in the present study. Considering the present problem is not a purely surface-tension-driven flow and the droplet impact inertia play an important role, we have also presented another characteristic time defined by $\mathrm{t_{inertia}} =$

$D_o/U = 9.3ms/\sqrt{We}$ for comparison. It is noted that physical times in lieu of the nondimensional times will be referred to throughout the below discussion.

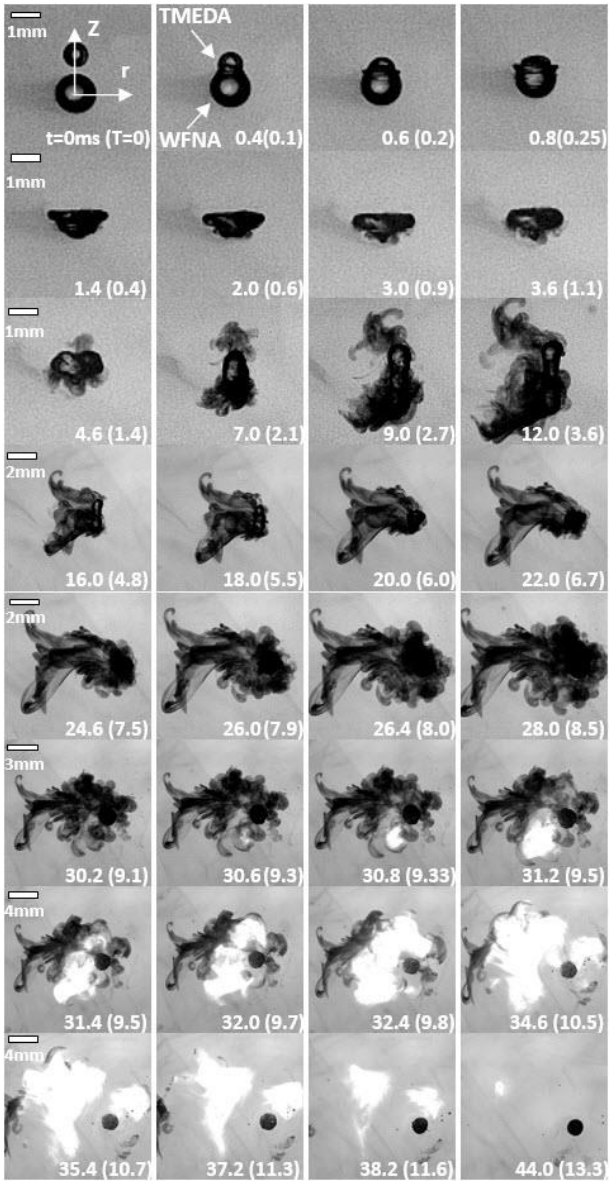

Figure 2.5 Shadowgraph images of the hypergolic ignition at selected times for a representative case with We=60.9 and Δ=1.6. $t_{inertia}$ =1.19ms.

The shadowgraph images at selected times are shown in Fig. 2.5, where $t = 0$ is defined as the moment when the droplets are about to collide. An axisymmetric coordinate

system is established on the WFNA droplet so that the head-on collision is along the z-direction. It is noted that different reference lengths are used for a clear presentation of the entire process, which spatially expands from a few hundred microns to a couple of centimeters. Resembling the drop tests of TMEDA/NA by Wang et al. [28, 56], the observed phenomena can be visually divided into five stages as follows.

Stage I (0ms – about 4.0ms): droplet coalescence and deformation. The dominant phenomena in this stage are droplet collision, coalescence and deformation, which are similar to those observed in the collision of two nonreactive droplets [37, 48]. A slightly dark "tail" behind the WFNA droplet is the shadow of NA vapor, which is negligible during this stage because of the relatively low droplet temperature and the short time. The droplet surface becomes increasingly blurry after about 2.0ms because the exothermic TMEDA/NA liquid-phase reaction starts increasing the droplet temperature and thereby expediting the droplet vaporization.

Stage II (about 4.0ms – about 20.0ms): droplet heating and vaporization. This stage is characterized by the spread of the blurred droplet surface, which is quickly concealed by the expansion of the opaque vapors and gaseous species. We can infer that droplet is being heated up from the inside to the surface, because the exothermic liquid-phase reaction occurs with the merged droplet where the effective mixing of TMEDA and WFNA can be

achieved by forming the jet-like flow patterns, as discussed in Introduction. This inference is consolidated by the vortex ring formation observed in Wang et al.'s drop tests [28, 56], which is a well-known counterpart of the jet formation in the drop-pool interaction. Because of the droplet heating, the surface temperature has not been fully increased in this stage and there by droplet vaporization is slower than that in the subsequent stage.

Stage III (about 20.0ms – about 30.0ms): rapid vaporization and reactions. The droplet vaporization and the reactions in both liquid and gas phases become significantly faster because of the increased droplet temperature. It is seen that, a large amount of vapors and gaseous species are produced; they appear as a large opaque area in the images.

Stage IV (about 30.0ms – about 31.0ms): ignition in gas phase. The ignition occurs at 30.6ms as the emergence of a bright kernel within the opaque area, implying the over-exposed luminous flame. The temporally resolved images enable the visual determination of the ignition delay time to be between 30.2ms and 30.8ms. Meanwhile, the shape and area of the opaque region do not have significant changes, but the grayscale levels of the ignition kernel vary substantially.

Stage V (after about 31.0ms): flame propagation and combustion. The luminous flame outwardly propagates in the gaseous species, as the opaque region recedes while the bright region expands within 4–5ms. When the opaque gaseous species are consumed

exhaustively, the flame extinguishes and a nonflammable condensed-phase product is left behind, as clearly seen in Fig. 2.6 for its solid-like surface appearance. It is also seen that, the volume of the product does not significantly change from 32.4ms to 44.0ms, and therefore substantiates its non-flammability.

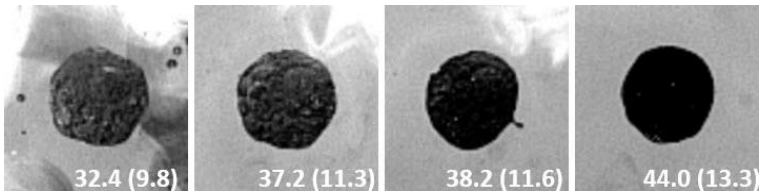

Figure 2.6. Nonflammable condensed-phase products from the representative case shown in Fig. 2.5.

2.3.2 Determination of Ignition Delay Time

As discussed in Introduction, the definition of hypergolic ignition is usually descriptive and system-dependent. For example, the hypergolic ignition in the common drop-test is defined as either the appearance of a flame as an indicator of reactivity [54] or the emergence of a visible luminous kernel in the gas phase above the liquid surface [28]. In the drop contact test of Dambach et al., the hypergolic ignition is defined as a highly transient phenomenon, which produces a flame after a multitude of complex coupled physical and chemical processes have occurred [31]. To accurately determine the ignition delay time in the present experiment, a method based on analyzing the grayscale levels of the shadowgraph images is used in the present study. As has been discussed in Section 2,

the average grayscale level of the background in each shadowgraph image is set to be 100; the dark areas representing either the droplets or the opaque gaseous species have the grayscale levels below a lower threshold value such as $G_{low} = 5$; the bright areas representing the luminous flames have grayscale levels above a higher threshold value such as $G_{high} = 250$. Consequently, two time-dependent ratios can be defined by

$$r_d = N_d(t|G < G_{low})/N, \quad r_b = N_b\big(t|G > G_{high}\big)/N \tag{2}$$

$N_d(t|G < G_{low})$ and $N_d\big(t|G > G_{high}\big)$ are the total numbers of pixels having the grayscale levels, G, lower than G_{low} and higher than G_{high}, respectively; N is the total number of pixels in the image.

Figure 2.7(a) shows the procedure of the grayscale level analysis. The monotonic rise of r_d from 0ms to about 30ms indicates the increased amount of opaque gaseous species from the droplet vaporization and the gas-phase reactions. Meanwhile, r_b remains a negligibly small value because ignition has not occurred. Stages I-III identified in Section 3.1 are manifest in this figure: r_d remains constant during Stage I (0ms–4ms), implying little liquid vaporization; Stage II (4ms–22ms) is characterized an approximately linear increase of r_d; Stage III (22ms–30ms) shows another approximately linear increase of r_d with a larger slope, implying the faster droplet vaporization after the completion of droplet heating.

During Stage IV (30ms–35ms), r_d decreases rapidly due to the consumption of the opaque gaseous species; r_b increases simultaneously because of the emergence and expansion of the luminous flames. The ignition delay time (abbreviated as IDT hereinafter) can be unambiguously defined as the instant corresponding to the turning point of r_d and r_b, namely, 30.6ms with an uncertainty of less than 0.2ms. Stage V starts at 35.6ms when r_b reaches its peak value, as a result of the full expansion of the luminous flames. This stage ends at around 44.0ms, when the luminous flames disappear. The value of r_d at 44.0ms is slightly larger than that at the initial time because of the opaque unburned gases and the condensed-phase products.

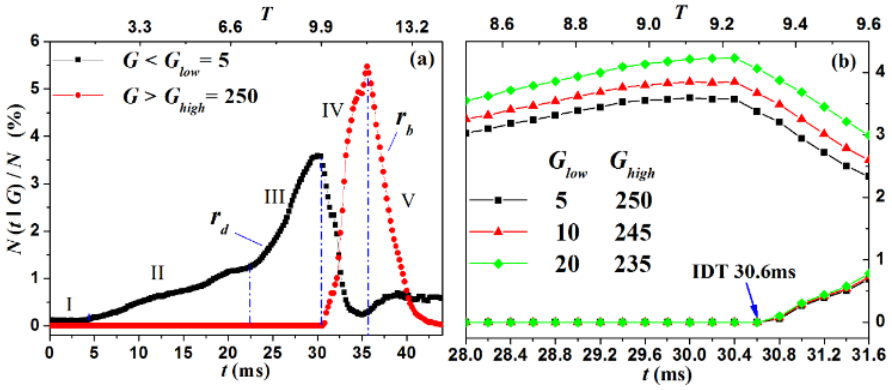

Figure 2.7. Grayscale level analysis of r_d and r_b for the representative case shown in Fig. 2.5, (a) during the entire process, and (b) around the ignition.

To quantify the sensitivity of the IDT to the arbitrarily chosen threshold values in Equation (2), we repeated the above analysis by using another two combinations of G_{low} and G_{high} and compared the results in Fig. 2.7(b). It is seen that the turn points of r_d and

r_b remain almost unchanged to the different threshold values and the uncertainty is less than 0.1ms. For consistency, $G_{low} = 5$ and $G_{high} = 250$ were used in the present study for determining all the IDTs.

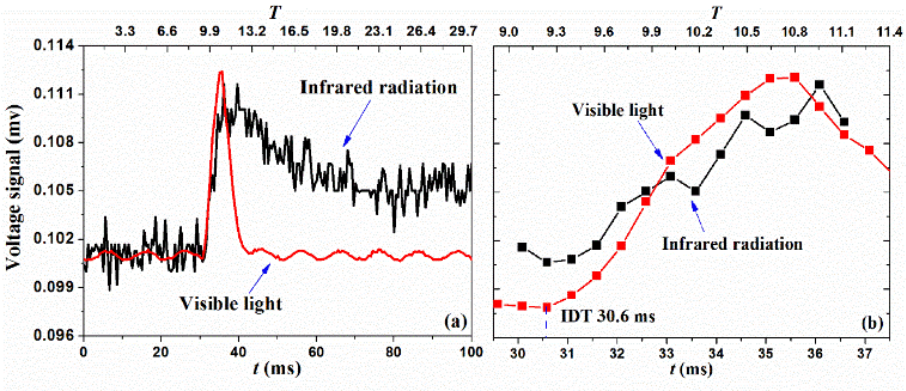

Figure 2.8. Voltage signals denoting the intensities of visible lights and infrared radiations (a) during the entire process and (b) around the ignition for the presentative case shown in Fig. 2.5.

To further validate the grayscale level analysis of shadowgraph images, we measured visible lights and the infrared radiation, as shown in Fig. 2.8(a). During the first three stages, the two voltage signals denoting the intensities of the visible lights and the infrared radiations remain constants regardless of the fluctuations due to the background noise. The occurrence of ignition is indicated by the simultaneous increases of both signals at 30.6ms, as shown clearly in Fig. 2.8(b), which is identical with the result from the grayscale analysis. It is also seen that the intensity signal of the visible lights increases to the peak value at about 35ms and subsequently decreases to its initial value after 40ms. Although the intensity signal of the infrared radiation increases almost synchronously with

that of the visible lights, it gradually decreases after 40ms, because the gas temperature slowly decrease due to the heat loss to the environment.

2.3.3 Regime Nomogram of Ignitability

A large number of experiments on the hypergolic ignitability by droplet collision have been conducted and the results are presented as a regime nomogram in the *We*-Δ parameter space, as shown in Fig. 2.9. An approximately straight line, fitted as Δ_{cr} = 0.0044*We* + 1.82, separates the *We*-Δ subspace of *We* = 20–220 and Δ = 1.2–2.9 into two regimes: the ignitable regime below the line and the non-ignitable regime above it. It is seen that increasing the size ratio suppresses the ignition and therefore a larger Weber

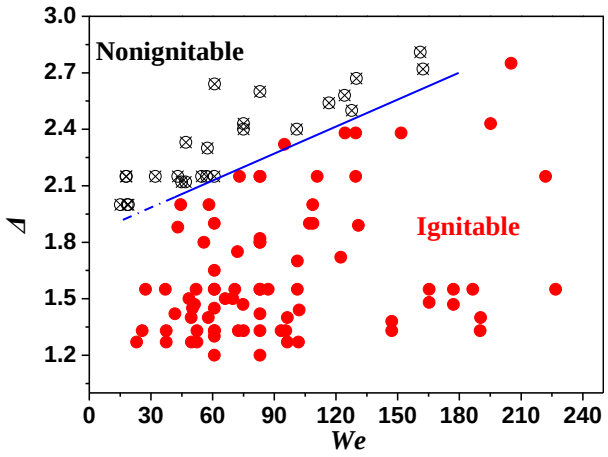

Figure 2.9. Ignitability regime nomogram in the We-Δ subspace of We = 20~220 and Δ = 1.2~2.9.

number is required to promote ignition. In the regime nomogram, the variation of *We* not only affects the internal mixing within the coalesced droplet but also causes the droplet

separation, which may drastically change the subsequent chemical reactions in both liquid and gas phases. The detailed discussions on the effects of *We* and Δ will be presented in the following sections.

2.4. Weber Number Effects on Ignition Delay

In order to illustrate the effects of the Weber number, *We*, on the IDT, the temporally resolved shadowgraphs for four cases are shown in Fig. 2.10(a)–(d). Only sixteen images at selected times are presented for each case for simplicity and clarity: the first four images for Stage I, the second four for Stage II, the third four for Stage III and the last four for Stages IV and V. The four cases have the same size ratio, Δ = 1.6, as that of the representative case discussed in Section 2.3, but two have the smaller *We* = 37.0 and *We* = 52.0, compared with *We* = 60.9 of the representative case, and the other two have the larger *We* = 70.8 and *We* = 83.0.

Compared with the representative case, the case with *We* = 37.0 has a longer Stage II as seen in Figure 2.10(a), which implies a slower droplet heating process as the result of a probably less degree of droplet mixing at the smaller impact inertia. Meanwhile, the prolonged droplet heating process may result in more heat loss to the environment, which

in turn results in a prolonged Stage III and a postponed ignition. The IDT of this case is 41.6ms.

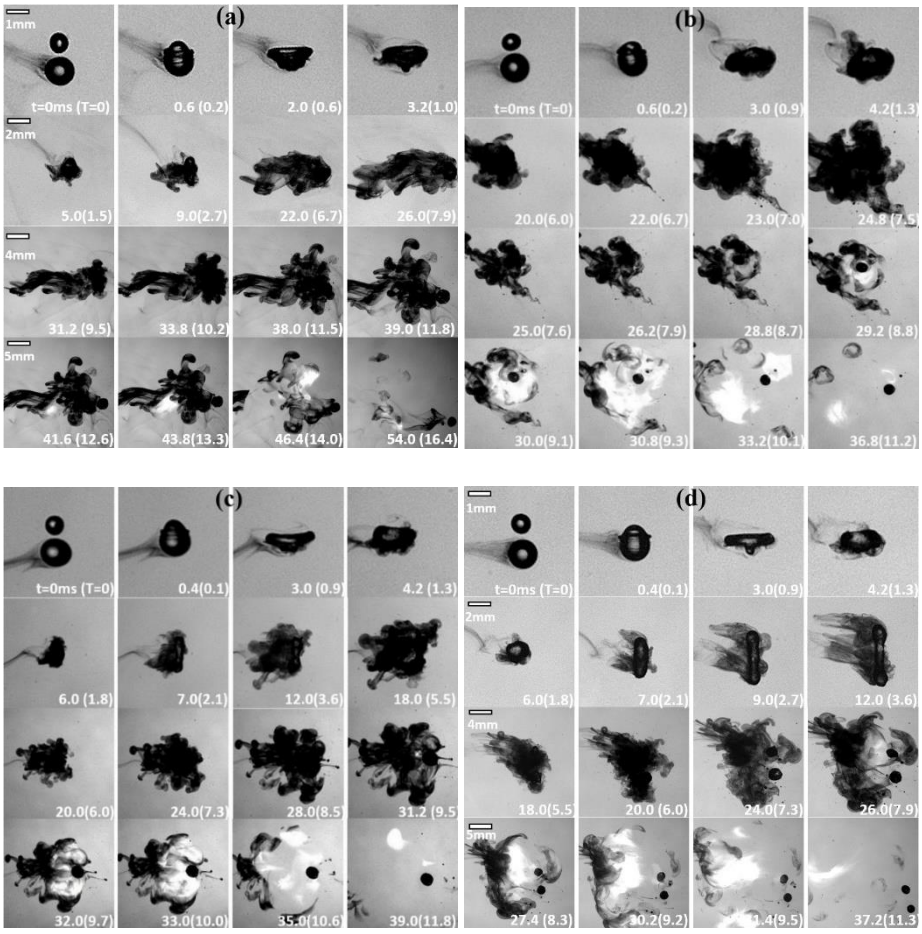

Figure 2.10. Shadowgraph images of the hypergolic ignition by collisions with a fixed Δ = 1.6, (a) *We* = 37.0, $t_{inertia}$ = 1.5ms, (b) *We* = 52.0, $t_{inertia}$ = 1.3ms, (c) *We* = 70.8, $t_{inertia}$ = 1.1ms, and (d) *We* = 83.0, $t_{inertia}$ = 1.0ms.

As the *We* increases to 52.0, one may expect to observe an IDT between 30.6ms (at *We* = 60.9) and 41.6ms (at *We* = 37.0). Surprisingly, a substantially smaller IDT of 29.2ms was observed and mainly attributable to the significantly expedited droplet vaporization, as clearly seen in Fig. 2.11(b). A possible explanation to the observation is the non-

monotonic emergence of the jet-like mixing patterns with varying the Weber number, as discussed in Introduction. The decrease of the IDT from 41.6ms at *We* = 37.0 to 29.2ms at *We* = 52.0 can be attributed to the mixing enhancement by increasing the Weber number. The increase of the IDT to 30.6ms at *We* = 60.9 may be caused by the suppression or disappearance of the jet-like mixing pattern. This speculation is further consolidated by the case with *We* = 70.8, in which a longer IDT of 31.2ms is seen in Figure 2.10(c). A direct visualization of the droplet mixing is however not available in the present study but merits future study.

Further increasing the Weber numbers can effect the decrease of IDT as the result of either the re-emergence of the jet-like mixing pattern, or the substantially increased droplet deformation, or both. The jet formation promotes the droplet internal mixing and the liquid-phase reaction; the droplet deformation augments the droplet surface area and hence the vaporization rate. As shown in Fig. 2.11(d) for the case with We = 83.0, the coalesced droplet substantially stretches along the direction of collision and results in a disk-shape deformation at 9.0ms. The significantly deformed droplet provides a larger surface area for the vaporization, as showed by a large amount of opaque gaseous species at 18.0ms. Although the droplet separation eventually occurs, as clearly seen at the times after 24ms, a shorter IDT of 26.0ms is obtained in comparison with those of smaller Weber

numbers. The two separated condensed-phase products are the proof of the droplet separation.

The dependence of the IDTs on the Weber numbers at the various size ratios of 1.3, 1.6 and 2.2 are shown in Fig. 2.11. Several observations can be made from the results. First, the IDT has an overall tendency of decreasing with increasing *We* because of the enhanced droplet deformation and mixing, both of which expedite the droplet vaporization and hence

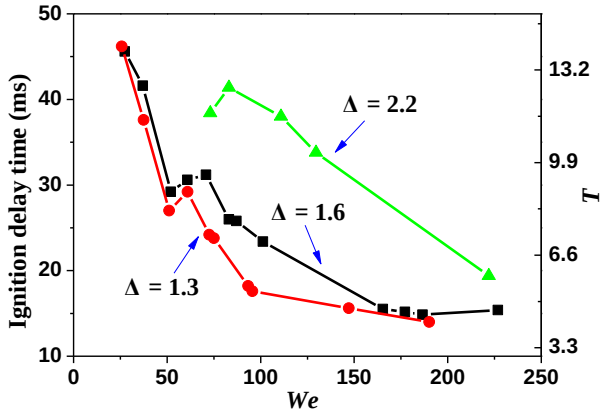

Figure 2.11 Dependence of ignition delay times on the Weber number at various droplet size ratios of 1.3, 1.6 and 2.2.

the subsequent gas-phase ignition. Second, the subtle, non-monotonic variation of the IDT with *We* can be found at all the size ratios, probably attributed to the non-monotonic emergence of jet-like mixing pattern. Third, as the *We* increases to be sufficiently high, the IDTs are as small as 15ms and do not show significant changes with *We*. This substantiates that the IDT at high *We*s will be independent of mixing but controlled by the chemical reactions of the propellants. Fourth, in the case of Δ = 2.2, no ignition was observed for the

*We*s smaller than 60.9. In addition, the IDTs tend to increase with the size ratios: the curve presenting for Δ = 2.2 is above that for Δ = 1.6, which in turn is above that for Δ = 1.3. These results imply that the size ratio plays a vital role in the ignition process, which will be discussed in the next section.

2.5. Size Ratio Effects on Ignition Delay

In order to illustrate the effects of the droplet size ratio, Δ, on the IDTs, the temporally resolved shadowgraphs for three cases are shown in Figure 2.12. The three cases have the same Weber number, 60.9, as that of the representative case discussed in Section 3, but one has a smaller Δ = 1.2 and the other two have larger Δ = 2.2 and Δ = 2.8.

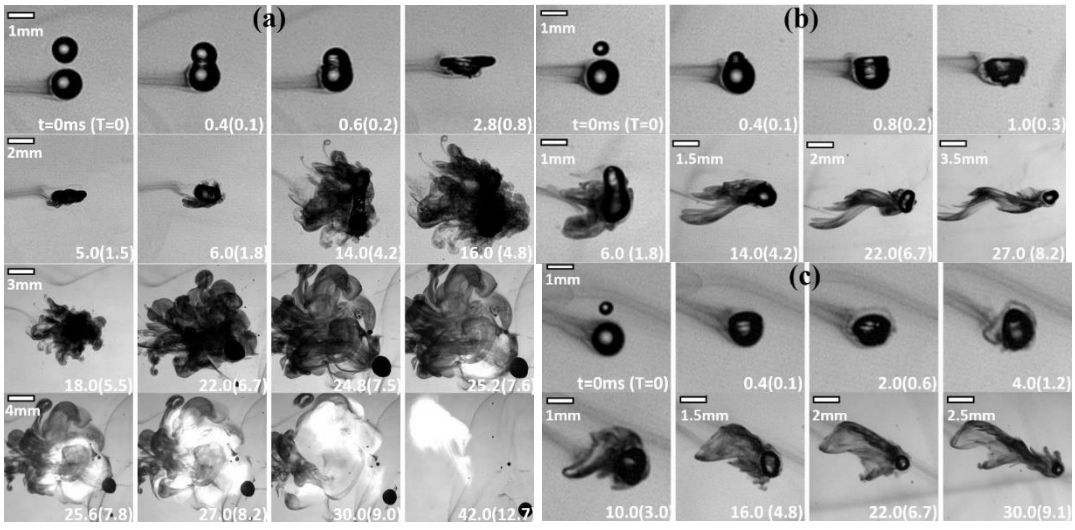

Figure 2.12 Shadowgraph images of the hypergolic ignition by collisions with a fixed *We* = 60.9 and (a) Δ = 1.2, (b) Δ = 2.2, and (c) Δ = 2.8. $t_{inertia}$ = 1.2ms for (a), (b) and (c).

Compared with the representative case with Δ = 1.6, the case with Δ = 1.2 exhibits similar droplet collision and ignition processes, as seen in Fig. 2.12(a). Nevertheless, the shorter ignition delay time of 25.2ms seems to contradict with the argument that increasing the size ratio enhances the droplet mixing and therefore expedites the ignition. This contradiction can be resolved by considering the chemical stoichiometry of the liquid-phase reaction (1). The overall equivalence ratio [57, 58] for the TMEDA/NA liquid-phase reaction can be defined as

$$\Phi_{\text{overall}} = \frac{M_{\text{TMEDA}}/M_{\text{NA}}}{(M_{\text{TMEDA}}/M_{\text{NA}})_{st}} = \frac{\tilde{V}_{\text{NA}}}{\tilde{V}_{\text{TMEDA}}}\frac{2}{\Delta^3} \approx \frac{0.56}{\Delta^3} \tag{2.3}$$

Where $\tilde{V}_{\text{NA}} = 41.65$ cm^3/mol and $\tilde{V}_{\text{TMEDA}} = 149.66$ cm^3/mol are the molar volumes. It is noted that the reaction does not occur at Φ_{overall} in the present non-premixed system, that Φ_{overall} has an indirect effect on the reaction, and that Φ_{overall} can be used as an indicator for the amount of maximally possible reaction heat release.

Using Eq. (2.3), we can have $\Phi_{\text{overall}} = 0.32$ for Δ = 1.2, and $\Phi_{\text{overall}} = 0.15$ for Δ = 1.6. The larger Φ_{overall} in the case with Δ = 1.2 may result in a larger amount of heat release, which has been proven to be critical to the subsequent fuel vaporization and decomposition. In addition, we can infer that, although the ignition favors the enhanced mixing by increasing the sizer ratio, it is more sensitive to the overall equivalence ratio,

which decreases cubically with the size ratio. This inference is confirmed by the two cases of Δ = 2.2 and 2.8, in which no ignition happens as shown in Fig 2.13(b)-(c). The possible reason for the non-ignitability of these two cases is that their overall equivalence ratios ($\Phi_{overall} = 0.05$ and $\Phi_{overall} = 0.025$) are too small for the liquid-phase reaction to generate enough heat for fuel vaporization. The deficient vaporization is manifestly seen in the shadowgraph images.

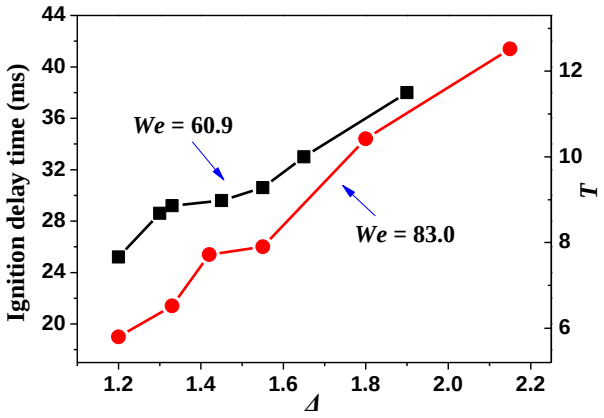

Figure 2.13 Dependence of the ignition delay times on the size ratio at the Weber numbers of 60.9 ($t_{inertia}$=1.2ms) and 83.0 ($t_{inertia}$=1.0ms).

Figure 2.13 shows the dependence of the ignition delay times on the size ratio at We = 60.9 and We = 83.0. With regard to the liquid-phase reaction between WFNA and TMEDA, the unity overall equivalence ratio corresponds to Δ = 0.8. Therefore, all the cases shown in the figure can be considered "fuel lean" and the ignition tends to increase monotonically with increasing Δ and hence decreasing $\Phi_{overall}$. A plateau of the IDTs can be observed for Δ = 1.33~1.55 at *We* = 60.9, and for Δ = 1.4~1.55 at *We* = 83.0. This may

be caused by the competition between the liquid-phase reaction, favoring small Δs, and the droplet mixing, favoring large Δs. As the overall equivalence ratio cubically decreases with Δ, the liquid-phase reaction dominates over the mixing enhancement in determining the IDT.

2.6. Concluding Remarks

Hypergolic ignition by a smaller TMEDA droplet colliding head-on with a larger WFNA droplet was experimentally studied for its relevance to rocket propulsion with hypergolic propellants. The newly established experimental apparatus eliminates the wall effect existing in the standard drop tests and enables to mimic the hypergolic ignition by the collision of two freely moving droplets. The present study was focused on understanding the influence of the droplet collision and mixing, which vary with the Weber number (We) and the size ratio (Δ) while at a fixed $Oh=2.5\times10^{-3}$, on the hypergolic ignitability and the ignition delay times. The hypergolic ignition processes were visually captured by time-resolved shadowgraph. The ignition delay times were determined, with an uncertainty of less than 0.2ms, by the grayscale level analysis of the shadowgraph images, which has been validated by the photoelectric methods based on visible lights and infrared radiations.

The hypergolic ignitability of TMEDA/WFNA can be characterized by a regime nomogram in the We-Δ parameter subspace of We = 20–220 and Δ = 1.2–2.9. An approximately linear line fitted as $\Delta_{cr} = 0.0044We + 1.82$ divides the subspace to the "ignitable" regime below Δ_{cr} and the "non-ignitable" regime above. These results suggest that the hypergolic ignition occurs when the size ratio is sufficiently small, and that increasing the Weber number augments the critical size ratio.

The effects of the size ratio on the hypergolic ignitability can be understood from two aspects. From the physical aspect, increasing the size ratio enhances the droplet mixing and hence the exothermic liquid-phase reaction, which is crucial for droplet heating, vaporization and decomposition of the propellants. From the chemical aspect, increasing the size ratio cubically deviates from the chemical stoichiometry of the liquid-phase reaction, TMEDA + 2NA → TMEDADN, because the WFNA droplet size is fixed in the present study and a larger size ratio means a smaller TMEDA droplet. The dominant chemical effect of the size ratio over its physical effect results in the favor of the hypergolic ignition to smaller size ratios. For the ignitable cases, the ignition delay times tend to increase with Δ. The appearance of the plateaus of IDTs, as the result of the competition of droplet mixing and chemical stoichiometry, consolidates the above explanation.

Increasing *We* often tends to enhance the droplet mixing and hence the liquid-phase reaction heat release, yielding a larger critical size ratio for the hypergolic ignitability. By the same token, the ignition delay times tend to decrease with increasing *We*. A seemingly counterintuitive result has been obtained in the present study that, in a certain (relying on Δ) range of *We*, the ignition delay times increase with *We*. This result can be speculatively attributed to the recently identified phenomena in droplet coalescence and internal mixing: the jet-like mixing patterns emerge at relatively small and large *We*s but disappear at intermediate *We*s. Future studies are merited to seek direct evidence to the speculation.

It is noted that all the above discussions are based on the situation where the WFNA droplet is larger than the TMEDA droplet. It merits a separate, future study to explore the hypergolic ignitability for the cases of $\Delta < 1$, namely, the WFNA droplet is smaller than the TMEDA droplet. For advocating such a study, we have conducted three exploratory experiments, at $We = 30.1$ and $\Delta = 0.5$, $We = 80.3$ and $\Delta = 0.5$, $We = 30.1$ and $\Delta = 0.7$, in which the size of the WFNA droplet is fixed at 0.3mm. No ignition was observed for all the three cases. A possible explanation is that these droplets are too small to generate sufficient heat release through the liquid-phase reaction, and additionally the large surface-volume ratios increase the heat loss to the environment.

In the present study, the Ohnesorge number is fixed so that the effects of liquid viscosity remain to be characterized. The thermal effect of the viscous dissipation on the hypergolic ignition delay is unlikely to be significant compared with the chemical heat release from the liquid-phase reaction of TMEDA and HNO_3. The fluid-dynamic influence of viscosity on the droplet separation and in turn the hypergolic ignition may be of interest and merits future study. Independent variation of *Oh* in the present problem can be only realized by varying D_O because the physical properties of WFNA are fixed. Adopting larger droplets in the experiment may cause the asphericity of droplets while adopting smaller droplets would signify the additional physics of heat loss in the present problem.

The above considerations urge a future study on the comprehensive characterization of the viscosity and size effects. Future efforts can be also made to enclose the experimental apparatus in a pure nitrogen environment with variable pressures to mimic the real engine conditions without atmospheric oxygen.

3. Mass Interminglement and Hypergolic Ignition of TMEDA and WFNA Droplets by Off-center Collision

3.1. Introduction

3.1.1. Hypergolic Ignition by Head-on Collision of TMEDA and WFNA Droplets

In order to focus on understanding the influence of droplet mixing on the hypergolic ignition and to avoid dealing with many factors at a time, the authors deliberately limited the scope of their experimental study in Chapter 2 to the head-on collision at variable collision Weber number ($We = 20 - 220$) and droplet size ratio ($\Delta = 1.2 - 2.9$) but at a fixed Ohnesorge number ($Oh = 2.5 \times 10^{-3}$) by fixing the size of the WFNA droplet. The TMEDA/WFNA hypergolic system was chosen for the study because it has been recently proposed as a promising substitute for the highly toxic hydrazine propellants. The experimental method can be applied to study other hypergolic systems. The most notable experimental discovery in the study is the non-monotonic variation of hypergolic ignition delay time with increasing We. The underlying physics is the non-monotonic emergence of a "jet-like" internal mixing within the coalesced droplet with increasing We, a fluid dynamical phenomenon that was recently identified by Tang *et al.* [48] in unequal-size droplet collision. The "jet-like" internal mixing facilitates the exothermic liquid-phase reaction, TMEDA + $2HNO_3$ → TMEDADN, whose heat release is crucial to the

subsequent droplet heating and vaporization, the decomposition of the propellants, and eventually the gas-phase ignition [28, 56]. Another notable experimental discovery is that Δ significantly affects the hypergolic ignition not only through its influence on the liquid-phase mixing but also by changing the available mass of the propellants participating the chemical reaction.

3.1.2. Off-center Collision and Mixing of Binary Droplets

In spite of the above findings about the hypergolic ignition by the head-on collision of TMEDA and WFNA droplets, it should be recognized that head-on collision is a rare event in reality and that off-center collisions are significantly more frequent. Figure 3.1 illustrates the off-center collision of two droplets of diameters D_S and D_L (the subscript "*S*" denotes the smaller droplet and "*L*" the larger one). The impact parameter, $B = 2\chi/(D_S + D_L)$, measures the deviation of droplet trajectory from the head-on situation and is defined as the ratio of the projection of the separation distance of two droplet centers in the direction of their relative velocity, χ, to the sum of the two droplet radii, $(D_S + D_L)/2$. Head-on collision occurs at $B = 0$, grazing collision at $B = 1$, and off-center collision at $0 < B < 1$. The relative importance of droplet inertia to its surface tension is characterized by the

collision Weber number, $We = \rho_L D_L U^2/\sigma_L$, and the effects of the size disparity by the size ratio, $\Delta = D_L/D_S$.

Most previous droplet collision experiments were focused on identifying various collision outcomes and quantifying the effects of various controlling parameters. Although the identified collision outcomes, such as bouncing, coalescence, separation and splashing, depend on not only We, B and Δ but also the ambient pressure and other liquid properties [6, 8], it can be generally concluded that bouncing occurs at relatively small $We \sim O(1)$, splashing occurs at sufficiently large $We \sim O(10^2)$, and coalescence and separation occur at intermediate $We \sim O(10)$ that concerns the present study.

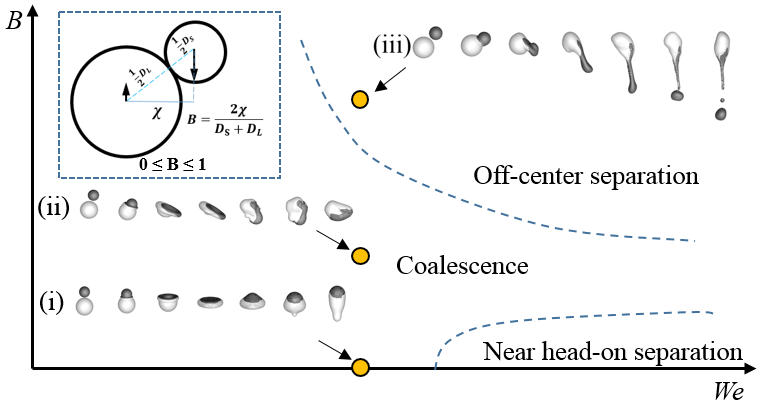

Figure 3.1 Schematic of droplet collision regimes in the $We - B$ parameter space: (i) head-on coalescence, (ii) off-center coalescence, and (iii) off-center separation. Droplet bouncing occuring at smaller Wes and droplet splashing at higher Wes are not shown for clarity.

Figure. 3.1 shows the droplet collision nomogram in the $We - B$ parameter space. The outcomes of droplet collision at fixed We and Δ but different Bs are schematized in Cases (i), (ii) and (iii). For head-on collision shown in Case (i), the two colliding droplets

exhibit axisymmetric impaction and oscillation, and result in permanent coalescence. With increasing B to affect the off-center collision shown in Case (ii), the coalesced droplets exhibit increasingly asymmetric impaction and stretching. At sufficiently large B shown in Case (iii), the intensely stretched droplet is eventually separated into two major droplets with a certain number of tiny satellite droplets.

The mixing of two colliding droplets is an important aspect of binary droplet collision and has recently gained increasing interests for its practical relevance in microfluidics and GHP systems. In consideration of that the head-on collision of identical droplets produces minimal mixing owing to its intrinsic "symmetry" in geometry and physical properties, researchers have employed "symmetry breaking" to enhance mixing by introducing size disparity[7, 37, 46, 48], non-Newtonian effect [45, 59], and Marangoni effect [60, 61] to droplet collision. Off-center collision, which breaks the geometric symmetry of head-on collision, has however not been sufficiently studied for its influence on droplet mixing, probably because the characterization and quantification of its intrinsically three-dimensional nature is challenging for both experiment and simulation.

In the early experimental study of Ashgriz and Poo [7], the inter-droplet mass exchange was observed after the stretching separation. Inamuro *et al*. [62] used the lattice Boltzmann method (LBM) to simulate the equal-size droplet collision at $We = 80$ and

various Bs. By tracing massless colored particles originally embedded in the two droplets, they defined a mixing rate as the percentage of the number of particles of a color in the total number of particles in a droplet. The mixing rate was found to non-monotonically vary with *B,* and the maximum mixing rate is about 30% at about $B = 0.2$. In another LBM study of Sakakibara and Inamuro [63] on the collision of unequal-size droplets, they observed mixing enhancement by increasing We at $\Delta = 2$ and $B = 0$, but did not report any results on the mixing rate for off-center collision.

Sun et al. [64] numerically studied the off-center collision of two identical droplets by using the moving particle semi-implicit method. Although their results show significant discrepancies compared with the previous experiments on collision outcomes, the non-monotonic variation of the mixing rate with B was observed at $We = 1.5$. A similar result was also obtained in the Volume-of-Fluid (VOF) simulation of Chen *et al.* [65] on the energy and mass transfer between two equal-size droplets with We being up to 70. Particularly, they found that the maximum mass transfer rate appears at about B=0.3~0.4, being consistent with Inamuro *et al.*'s results.

3.1.3. Motivations and Scopes of the Present Study

The previous results on the non-monotonic droplet mixing rate with varying B inspired the authors to conduct the present experimental and numerical study on the off-center collision of TMEDA and WFNA droplets of unequal sizes. There are a few remarks about the motivations and scopes of the present study.

First, the non-monotonic variation of the droplet mixing rate with B implies that there might exist a corresponding non-monotonicity of hypergolic ignition delay. The present study aims to not only contribute a worthy, significant enrichment to the previous experimental observations limited to head-on collisions, but also embrace complex, interesting fluid physics that demands additional computational investigations.

Second, to avoid the unnecessary complexity of phenomenological description and to facilitate the comparison with head-on collision, the present experimental study was first focused on the representative situation with $We = 60.9$, $\Delta = 1.6$ but with various B, and then extended to other Wes and Δs. The Ohnesorge number, which measures the relative importance of droplet viscous force compared with droplet inertia and surface tension, was still fixed at $Oh = 2.5 \times 10^{-3}$ in the present study by fixing the size of the WFNA droplet. The influence of Ohnesorge number, or more generally, the droplet size effects, merit future studies but will not considered in the present one.

Third, to help understand the present experimental observations, we conducted the VOF simulation of the off-center collision of non-reacting droplets, with emphasis on investigating the influence of B on droplet mixing. Similar simulations have been reported in literature for either equal-size droplets or head-on collisions, but not for the off-center collision of unequal-size droplets. It should be noted that we had no intention to simulate the extremely complex and tangled physicochemical processes of hypergolic ignition of TMEDA and WFNA droplets, including the fluid-dynamical processes of droplet collision and mixing, the transport processes of mass diffusion and droplet heating, the phase change process of droplet vaporization, and the chemical processes in liquid and gas phases. Based on the results from the previous study [66], the hypergolic ignition delay concerned in the present problem dominantly depends on the early stage of droplet interaction characterized by the fluid-dynamical processes of droplet collision and mixing. Consequently, the present VOF simulation, which has been sufficiently validated against available experiments in literature, is able to provide useful information about the early stage of droplet interaction, when the physical transport, phase change and chemical reactions have not fully emerged yet.

Based on the above considerations, we present the present study as follows. The experimental apparatus and methodology are described in Section 2, followed by the

expatiated VOF method and experimental validation, in Section 3. Internal mixing and hypergolic ignition of TMEDA and WFNA droplets under slightly off-center conditions are presented and analyzed, with the help of the VOF simulation, in Section 4. As increasing the impact parameter to effect droplet stretching separation, the moderately off-center and nearly grazing collisions are presented and analyzed, in Section 5. The correlation between the quantitative mixing index and the ignition delay time is presented, in Section 6, followed by the discussion about We and Δ effects, in Section 7.

3.2. Experimental Specifications

The schematic of the experimental apparatus used in the present study has been expatiated in Chapter 2 and therefore will not be repeated here. Some specifications about the setup and operations are provided as follows.

Particularly, the dispensing method and frequency for TMEDA and WFNA droplets are the same with those in the experiments in Chapter 2. Diversity of impacting parameters are realized by precisely changing one trajectory of the TMEDA droplet in the collision plane. The high speed camera is still the main measurement method and the data analysis is still based on the grayscale level analysis under the same accuracy.

3.3. Numerical Methods and Experimental Validations

As declaimed before, this simulation part of work was executed by my college Mr. He with whom I am always grateful. The numerical setup is depicted detailedly in [66] and will be not be repeated herein.

3.4. Hypergolic ignition by slightly off-center droplet collision

3.4.1 Phenomenological description of hypergolic ignition

The hypergolic ignition by the slightly off-center collision are phenomenologically described for a representative case of $We = 60.9, \Delta = 1.6$, and $B = 0.3$. The shadowgraph images at selected physical times are shown in Fig. 3.2(a), which are compared with the head-on case ($B = 0.0$) at same We and Δ from Chapter 2, as shown in Fig. 3.2(b). The non-dimensional times scaled by using the characteristic oscillation time fixed at $t_{\mathrm{osc}} =$ 8.83 ms in the present study are also given in the figures. Considering that the problem is not merely surface-tension driven, the characteristic inertia time, defined as $t_{\mathrm{ine}} = D_L/U$, is also presented for comparison. The stretching deformation and rotation of the merged droplet are described by an arrow pointing from the mass center of the larger WFNA droplet to that of the smaller TMEDA droplet.

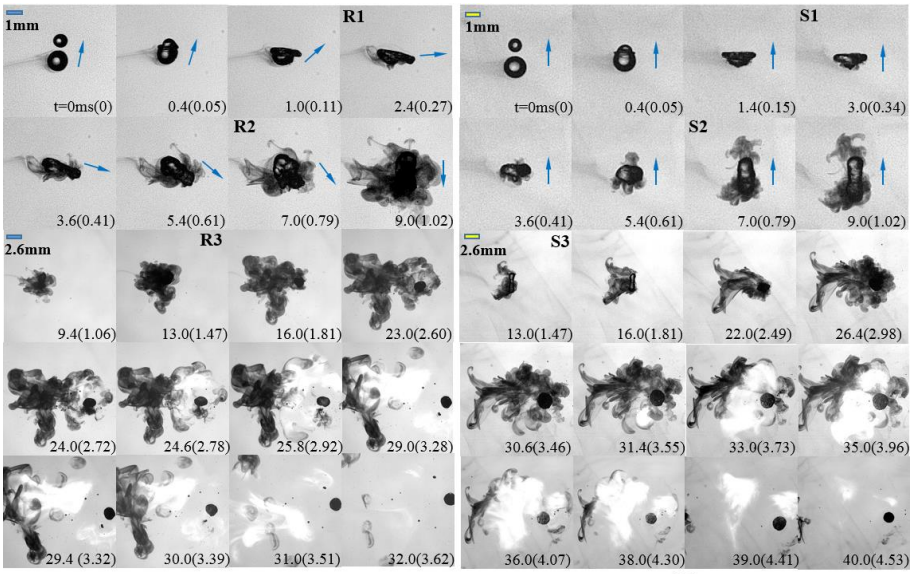

(a) (b)

Figure 3.2. Shadowgraph images of the hypergolic ignition at selected times for two representative cases with the same $We = 60.9$, $\Delta = 1.6$, but different (a) $B = 0.3$ and (b) $B = 0.0$ (adapted from Zhang et al. [17]). $t_{ine} = 1.19\ ms$, $t_{osc} = 8.83\ ms$.

Similar to the head-on collision of TMEDA/WFNA droplets, the entire process of the slightly off-center collision with $B = 0.3$ can be divided into five distinct stages. Different reference lengths from 1.0 mm to 2.6 mm were used in the figures for better visualization of these stages.

Stage I (0 ms – about 3.6 ms): droplet coalescence and deformation. The shape of the merged droplet can be clearly seen during this stage, and a slightly dark "tail" behind the WFNA droplet is the fuming. The minor vapor is negligible in this stage because the heat release from exothermic liquid-phase chemical reactions is not substantial to vaporize the droplet but only makes its surface increasingly blurry. The arrow denoting the mass center vector rotates nearly 90 degrees at 3.6 ms for $B = 0.3$, while it remains almost

unchanged for $B = 0.0$. This implies that the significant droplet stretching effects may increase the contact surface of two droplets.

Stage II (about 3.6 ms – about 9 ms): droplet heating and vaporization. The droplet is being heated up from the inside to the surface by the liquid-phase reactions. This is inferred by the observation that the opaque vapor starts to expand as the result of the increasing droplet temperature. The merged droplet keeps rotating and the mass center vector turns nearly 180 degrees at 9 ms, meanwhile the droplet is significantly stretched.

Stage III (about 9 ms – about 24 ms): rapid vaporization and reactions. The droplet shape is almost concealed by the rapid expansion of opaque vapor probably because the droplet is totally heated up and results in large amount of vaporization.

Stage IV (about 24 ms – about 29 ms): ignition in gas phase and flame propagation. A bright kernel implying the over-exposed luminous flame within the opaque area is observed at 24.6 ms for $B = 0.3$ as the occurrence of hypergolic ignition, which is about 6 ms earlier than that for $B = 0.0$. Furthermore, the luminous flame propagates rapidly as illustrated by the expansion of the bright kernel while simultaneously reduction of the opaque region.

Stage V (after about 29 ms): combustion and flame extinction. When the gaseous species are consumed exhaustively, a nonflammable condensed-phase product is left

behind and will preserve its solid-like appearance until the flame extinction, which is consistent between the observations for head-on droplet collision.

3.4.2 Quantitative analysis of the hypergolic ignition

As expatiated in Chapter 2, the analysis of the grayscale levels of the shadowgraph images can be used to systematically determine the ignition delay time with high accuracy. The opaque vapor (or the luminous flame) area can be evaluated by counting the total pixel numbers N_d (or N_b) with a grayscale level G below (or above) the threshold value of $G_{\mathrm{low}} = 5$ (or $G_{\mathrm{high}} = 250$) in the entire image. While the background grayscale level is set to an intermediate value of $G = 100$. Then two time-dependent ratios can be defined as

$$r_d = N_d(t|G < G_{low})/N, \quad r_b = N_b\big(t|G > G_{high}\big)/N \tag{3.3}$$

where N is the total pixel numbers in the entire image; the subscripts “d” and “b” denote dark and bright.

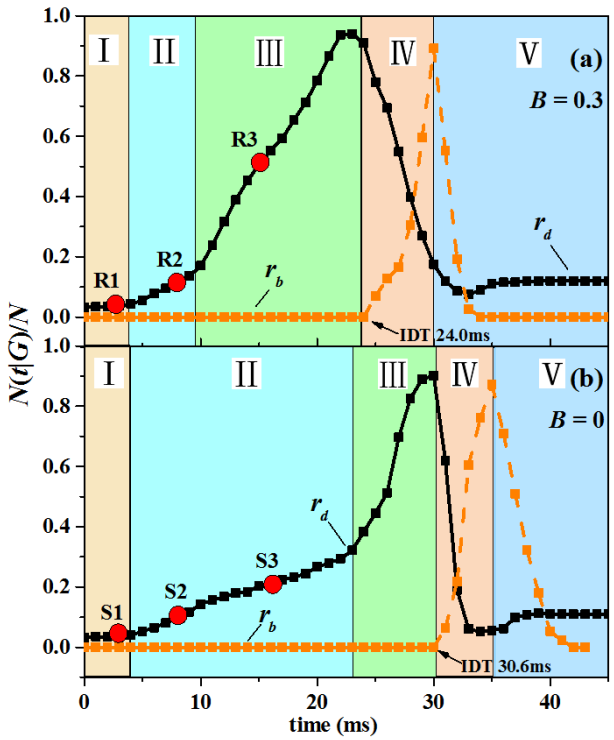

Figure 3.3. Evolution of $r_d = N_d(t|G < G_{low})/N$ (solid lines) and $r_b = N_b(t|G > G_{high})/N$ for the two representative cases shown in Fig. 3.2, (a) B = 0.3 and (b) B = 0.0.

Figure 3.3 shows the evolution of the two ratios for the two representative cases discussed in Section 3.4.1. The division of the entire process being into five stages is substantiated by the greyscale analysis. Specifically, r_d remains a small value in Stage I, experiences an approximately linear increase in Stage II, and shows another approximately linear increase with a larger slope in Stage III. The different change rates of r_d underlie the above division of droplet heating with slow vaporization from the droplet rapid vaporization. Meanwhile, r_b stays at nearly zero in the first three stages because ignition has not occurred. During Stage IV, a rapid decrease of r_d and a sharp increase of r_b happen simultaneously because of the consumption of opaque gaseous species and the expansion

of luminous flame. The ignition delay time (IDT) can be therefore defined as the turning point of r_b between Stage III and Stage IV. In Stage V, r_b decreases to its initial value because the propagating flame finally extinguishes after consuming all the gas-phase combustible, while r_d remains nearly constant of a small value because of the opaque non-flammable condensed-phase product. Although the trends of r_d and r_b are similar for $B = 0.3$ and $B = 0.0$, they have significant differences on the time evolution.

First, the time duration of Stage II for $B = 0.3$ (about 7ms) is substantially shorter than that for $B = 0.0$ (about 20 ms), indicating that the merged droplet by slightly off-center collision is easier to be heated up than by the head-on collision. This can be attributed to the enhanced internal mixing by droplet stretching at $B = 0.3$.

Second, the time duration of Stage III for $B = 0.3$ is moderately longer than that for $B = 0.0$. This can be understood by that, on the one hand, to reach the approximately equal peak value of r_d, the initial amount of opaque vapor commencing the rapid vaporization for $B = 0.3$ is lower than that of $B = 0.0$; on the other hand, the lope of r_d for $B = 0.3$ is smaller because the combustible gaseous mixture has been expanded to a larger area and probably subjected to an increased heat loss.

Third, it is clearly seen from the turning point of r_b that the accurately identified IDT for $B = 0.3$ (24.0 ms) is 6.6 ms shorter than that for $B = 0.0$ (30.6 ms). In stage IV,

the slope of r_d for $B = 0.3$ is smaller than that for $B = 0.0$ because the combustible gaseous species for the former case is spread out in a broader area and is consumed more slowly by the flame propagation.

Overall, compared with the head-on collision, the slightly off-center collision results in faster droplet heating and vaporization, and thereby leading to a shorter IDT. It was hypothesized that this result is caused by the enhanced internal mixing by droplet stretching. Consequently, the droplet internal mixing will be discussed in the following section with the help of numerical simulation.

3.4.3 Mixing enhancement by slightly off-center droplet collision

Figure 3.4 [66] shows three sets of experimental shadowgraph images and simulation results that were selected and compared at three representative moments, indicated in Fig. 3.4 by "R" for $B = 0.3$ and "S" for $B = 0.0$. The column (a) is the experimental images amplified for a clearer illustration, in which the droplet outer profiles (on the x-z plane) are delineated in red. The columns (b)-(d) are the corresponding simulation results viewed from three different directions, where the red denotes the fluid mass from the TMEDA droplet and the gray the WFNA droplet. The column (e) shows pressure contours and streamlines on slice cut by the x-z plane. It is reemphasized that the

impact velocity is along the x-direction and the droplets deviate from head-on situation in the z-direction, thus the x-z plane is the symmetric plane of the collision system.

The first representative instant, indicated as R1 for $B = 0.3$ and S1 for $B = 0.0$, was selected from their corresponding Stage I. The slightly off-center collision causes the merged droplet to rotate and stretch so that the droplet resembles an asymmetric "spoon", while the head-on collision results in an axisymmetric saucer-like droplet shape. The enhanced stretching effects around the contact surface of two droplets can be further verified by the streamline in Fig. 3.4(e).

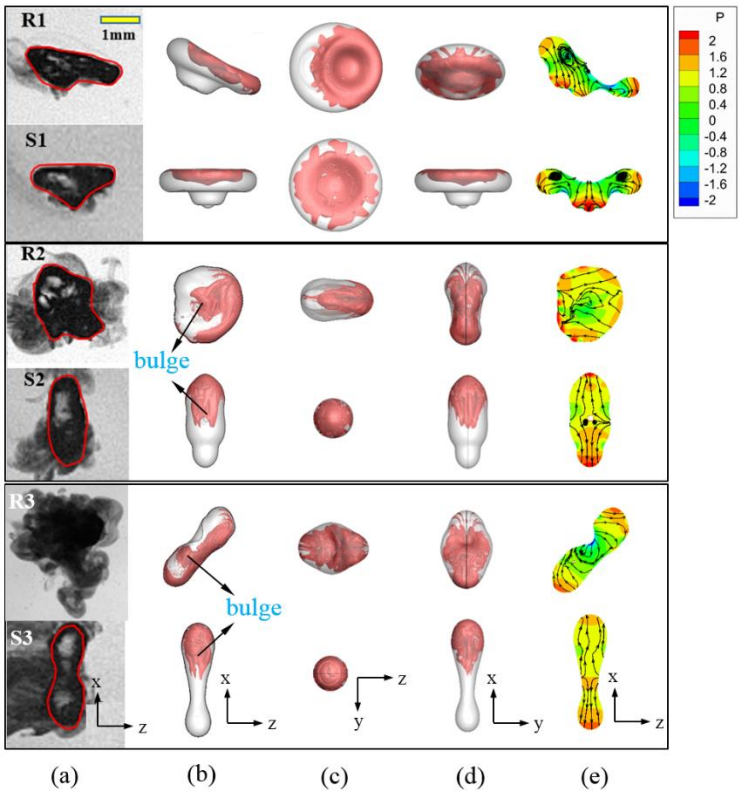

Figure 3.4. Comparison between $B = 0.3$ (denoted by "R") and $B = 0.0$ (denoted by "S") for three representative moments indicated in Fig. 3.3. (a) the experimental shadowgraph images, (b)-

(d) the simulation results viewed from three different directions, and (e) the pressure contours and streamlines.

The second representative instant, indicated as R2 for $B = 0.3$ and S2 for $B = 0.0$, was selected from their corresponding Stage II. The direct observation indicates that the internal mixing for R2 seems stronger than that for S2, because additional mass is spread out close to the droplet surface besides the bulge-like formation emerged in both cases.

The third representative instant R3 for $B = 0.3$ was selected form Stage III, while S3 for $B = 0.0$ was still in Stage II. It is noted that the merged droplet has been completely concealed by the opaque vapor for R3 while it can be seen for S3. The bulge-like formation could still be seen clearly in both cases, specifically for the slightly off-center collision with $B = 0.3$, the more intense interminglement of the liquid mass within the merged droplet is evidently seen and could lead to a more uniform droplet vaporization. While for head-on collision with $B = 0.0$, as the streamline shown in Fig. 3.4(e), the separation tendency could suppress the mass interminglement between two droplets.

3.5. Hypergolic ignition by stretching separated droplet collisions

To further increase the impact parameter, the stretching inertia becomes larger and would be dominant over reflexive inertia to result in stretching separation, which weakens

the mass interminglement between two droplets and thereby leads to a completely different hypergolic ignition process to that of the slightly off-center case.

3.5.1 Hypergolic ignition by moderately off-center droplet collision

The shadowgraph images and the grayscale level analysis of the hypergolic ignition by moderately off-center droplet collision at $We = 60.9, \Delta = 1.6, B = 0.6$ are illustrated in Fig. 3.5(a) and Fig. 3.6(a), respectively. Although the phenomenal five stages resembling to the two representative cases in Section 3.4.1 can still be observed, they display different characteristics.

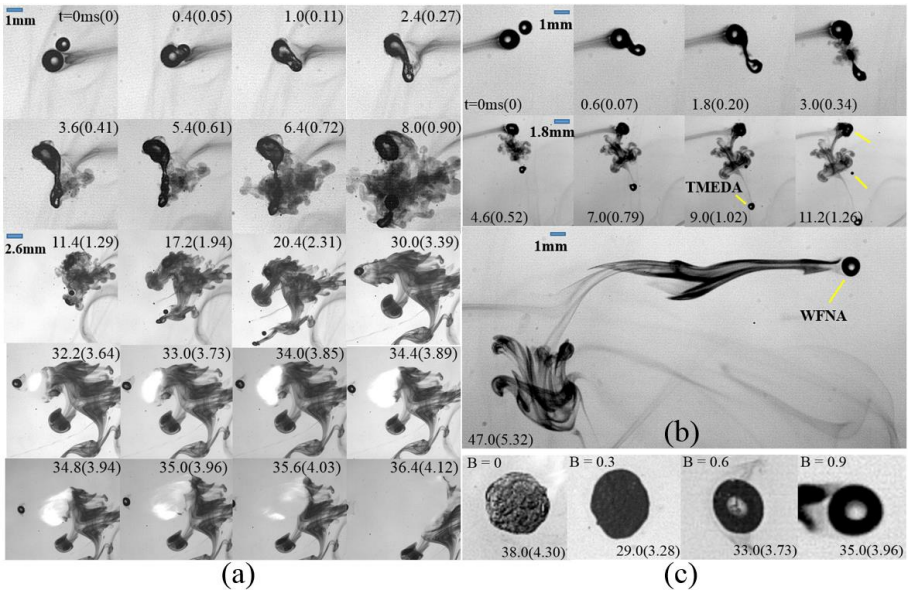

Figure 3.5. Shadowgraph images of the hypergolic ignition at selected times for two representative cases with the same $We = 60.9$, $\Delta = 1.6$, but different (a) $B = 0.6$ and (b) $B = 0.9$. $t_{ine} = 1.19\ ms$, $t_{osc} = 8.83\ ms$. (c) the surface appearance of the nonflammable products by off-center droplet collision for various Bs.

As shown in Fig. 3.5(a), the droplet stretching deformation for $B = 0.6$ is enlarged when compared to the slightly off-center collision in stage I (0 – about 3.6 ms). Then, filament is formed with minor vaporization around at about 5.4 ms and the stretching separation is about to occur at 6.4 ms. At last at about 8.0 ms, the separated TMEDA droplet moving away from the larger WFNA droplet is observed, with a satellite droplet between them and surrounded by large amount of opaque vapor. It is inferred that the opaque vapor must be vaporized from the separated satellite droplet containing both TMEDA and WFNA fluid mass with a sufficient interaction. The satellite droplet is quickly concealed by the expansion of opaque vapor and disappears to form the gaseous species and some smaller satellite droplets at about 20.4ms due to the explosion of the major satellite droplet with violent chemical reactions.

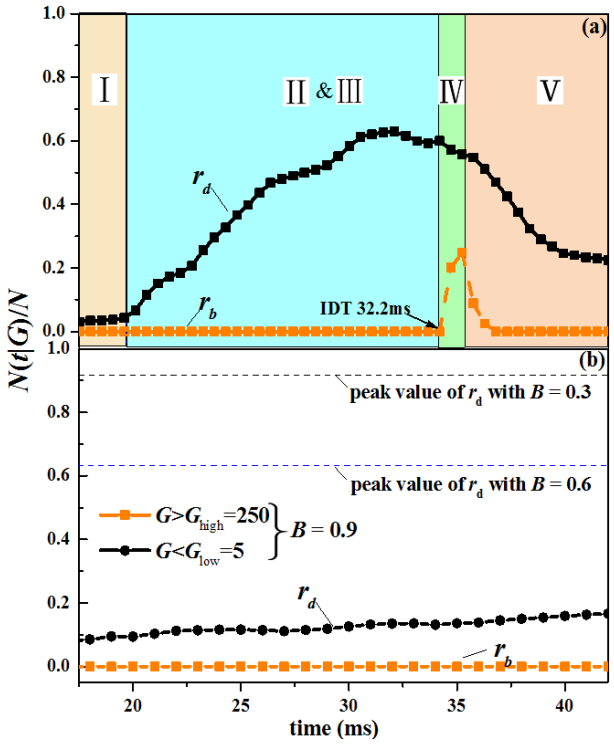

Figure 3.6. Grayscale level analysis of r_d and r_b for the representative two cases shown in Fig. 3.5(a) and Fig. 3.5(b).

The ignition occurs at about 32 ms as the emergence of a bright kernel, however, the luminous flame only propagates in a small area restricted in the upper left of the image and extinguishes at about 37 ms with an amount of unburned gaseous species left, which is also can be seen by a small r_b in stage IV and a large r_d at the end of stage V in Fig. 3.6(a). It indicates that the unburned gaseous species is not well-mixed TMEDA/WFNA mass but might be either one single phase vapor. Consequently, owing to the insufficient interaction mass participating the reaction, the ignition would be delayed, resulting in a longer ignition delay time (32.2 ms) compared to both $B = 0.3$ (24.0 ms) and $B = 0.0$ (30.6 ms). It is also noted that the ignition delay time is not coherent with the peak value

of r_d, because the consumption of the limited flammable mixtures requires a period to release sufficient heat for the hypergolic ignition by the weak exothermic reactions.

Regardless of the above differences, a most distinctive characteristic for $B = 0.6$ is that there are no any distinguished slow and rapid vaporization periods any more but showing an approximately linear increase of r_d with a certain slope during the entire process. It seems the droplet heating process has been skipped. That can be understood as that, the locally formed filament and separated satellite droplets have a large surface/volume ratio so that they could be heated up easily and generate rapid vaporization at the first beginning. However, the initial rapid vaporization for $B = 0.6$ has not developed more opaque vapors than that of $B = 0.3$ and $B = 0.0$ at last, because the major droplet mass for each fluid consisting of the most part of vapors has been moved away by the stretching separation, which reduces the possibility to form the gaseous mixture and thereby suppresses the gas-phase reactions and further vaporization.

3.5.2 Hypergolic ignition by nearly grazing droplet collision

The shadowgraph images and the grayscale level analysis of the hypergolic ignition by nearly grazing droplet collision at $We = 60.9, \Delta = 1.6, B = 0.9$ are illustrated in Fig. 3.5(b) and Fig. 3.6(b), respectively. It can be treated as a similar case to that of $B = 0.6$

except that the enhanced stretching effects lead to more substantial stretching deformation, less amount of mass interminglement, and thereby no hypergolic ignition.

More specifically, the nearly grazing colliding droplets show a more substantial stretching deformation than that of moderately off-center collision, which forms a thinner filament that readily to separate, as shown by the shadowgraph image at 3.0 ms in Fig. 3.7. The locally enhanced mass interaction in the filament or satellite droplets can also lead to some vaporizations, however, the interaction mass is too less to release sufficient heat for further droplet vaporization and hypergolic ignition. Except the opaque vapor generated from the thin filament or satellite droplets, there are another amount of opaque vapor can be seen around the larger separated WFNA droplet, as seen at 9.0 ms. Meanwhile, the surface of separated WFNA droplet is blurred while the surface is smooth for separated TMEDA droplet. This can be understood as that, the separated WFNA droplet grasps few mass of TMEDA fluid after the stretching separation, which leads to the inner exothermic liquid-phase reactions heating up the WFNA droplet surface to appear as blurred. Similarly, the remnant TMEDA mass in separated WFNA droplet is too less to result in vast vaporization and hypergolic ignition.

It is further proved by the grayscale level analysis in Fig. 3.6(b) that r_d experiences a negligibly slight increase at the entire process and much less than the peak value of $B =$

0.3 and $B = 0.6$. While r_b remains zero all the time because no hypergolic ignition is observed.

In terms of the non-ignitability, Fig. 3.5(c) illustrates the nonflammable products after droplet collision for various Bs. The solid-like surface appearance of the condense-phase product after sufficient reactions is observed for slightly off-center droplet collision with $B = 0.3$, resembling to that for head-on collision with $B = 0.0$ as depicted by Zhang *et al.*[66]. While the product surface appearance for moderately off-center collision with $B = 0.6$ is distinct appearing to the unreacted droplet except little turbidity in the center area because of the partially mass interaction and hence incomplete chemical reactions. Furthermore, the product for nearly grazing collision with $B = 0.9$ is completely a single-phase unreacted droplet which holds the smooth surface appearance.

3.6. Correlation of internal mixing and IDT for off-center droplet collision

For the representative cases with $We = 60.9, \Delta = 1.6$ for various Bs, the simulation results involving the internal flow visualization have provided a qualitative explanation about the effects of non-monotonic variation of internal mixing on the non-monotonic variation of observed IDT with varying from head-on to nearly grazing collision of

TMEDA/WFNA droplets. To further correlate the internal mixing and IDT, a mixing index is going to be introduced to strengthen the previous discussions quantitatively.

The time-dependent mixing index M [48, 73] varying from 0 to 1 can be defined as

$$M = \frac{\int_V |C - C_\infty| H(f-1) \mathrm{d}V}{\int_V |C_0 - C_\infty| H(f-1) \mathrm{d}V} \tag{3.4}$$

Where f is the volume-of-fluid function having $f = 1$ for fluid, $f = 0$ for gas, and $0 < f < 1$ for the free interface; $H(f-1)$ is the Heaviside step function restraining the mixing calculation only within the droplets; V is the total volume of fluid droplets; C is the spatially and temporally varying "concentration" to indicate the ratio of dyed mass to whole fluid mass, while C_0 and C_∞ are the "concentration" constants defined in the initially unmixed droplet and fully mixed situation, respectively. They are defined by

$$C_0 = \begin{Bmatrix} 0, & \phi = 0 \\ 1, & \phi > 0 \end{Bmatrix}, C_\infty = 1/(1+\Delta^3), C = \frac{|\phi - 0.5|}{0.5} C_0 \tag{3.5}$$

Where ϕ is the mass dye function, having $\phi = 1$ in the initial smaller droplet otherwise $\phi = 0$.

Figure 3.7[66] shows the internal mixing index and numerical collision outcomes between two reaction-free TMEDA and WFNA droplets at $We = 60.9, \Delta = 1.6$ for various Bs up to one non-dimensional time $T = 1.0$.

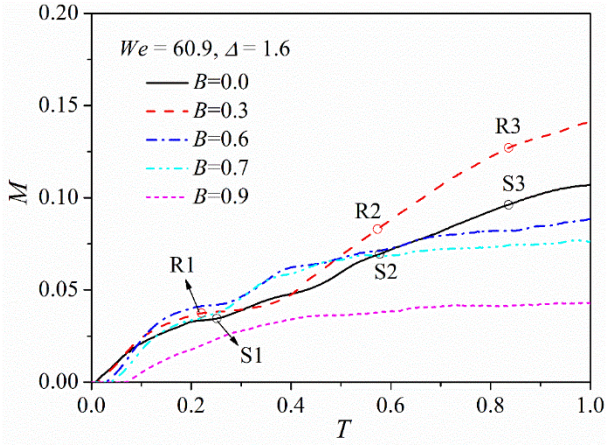

Figure 3.7[66] Variation of mixing index for various impact parameters $B = 0.0, 0.3, 0.6, 0.7$ and 0.9 at $We = 60.9, \Delta = 1.6$.

The three representative moments discussed in Section 3.4.3 are also illustrated on the mixing index curve in Fig. 3.7. The results show that the mixing index line of $B = 0.3$ is nearly always above that of $B = 0.0$, except a slight oscillation between R1 and R2 because the coalesced droplet has reached the maximum deformation and starts to turn back under the surface tension, indicating that the internal mixing is indeed enhanced for $B = 0.3$ as discussed before.

In terms of the moderately off-center droplet collision, the rapid increase of mixing index for $B = 0.6$ in earlier stages attributes to the formed filament and satellite droplets with locally well mixing, however, the mixing index cannot keep increasing rapidly because of the suppression of the stretching separation and limited mass interminglement, leading to the mixing index lower than that of both $B = 0.3$ and $B = 0.0$ at the later stages. It means the hypergolic ignition not only relies on the internal mixing but also depends on

the amount of interaction mass participating the reactions. To show the transition to nearly grazing droplet collision with $B = 0.9$, one more case with $B = 0.7$ is added deliberately, showing that the mixing index monotonically decreases as increasing the impact parameters from 0.6 to 0.9. Consequently, the lowest mixing index of $B = 0.9$ would lead to no hypergolic ignition.

3.7. The combination (We, Δ, B) effects on the IDT and ignitability

As the problem simplifications presented in Section 3.3.1, only three controlling non-dimensional parameters, namely, We, Δ and B, need be considered in the present study. The We and Δ effects for head-on collision between TMEDA and WFNA droplets had been discussed in Chapter 2 that the IDT tends to decrease for smaller Δs and larger Wes in an overall tendency except some local oscillations in a certain parameters range. In the present study, the B effects have been investigated by the representative cases at $We = 60.9, \Delta = 1.6$ for various Bs, showing that the IDT increases first and then decreases experiencing a non-monotonic variation as increasing B. However, the B effects for various Wes and Δs on ignition delay time have not been discussed, which might be interesting and enrich the phenomena observations and understandings.

3.7.1 B effects for various Wes and Δs on determining the IDT

Based on the representative cases at $We = 60.9, \Delta = 1.6$ for various Bs, Fig. 3.8(b) shows two more cases with different size ratios, namely $\Delta = 1.3$ and $\Delta = 2.0$. Furthermore, more cases involving We effects are shown in Fig. 3.8(a) with $We = 41.0$ and Fig. 3.8(c) with $We = 83.0$. A criticism needs to be clarified is that the difficulty of strongly corrosive droplet generation at some parameter ranges because of the manufactured in-house needle-shape nozzle, leads to a defective data base missing $\Delta = 1.6$ for $We = 41.0$ in Fig. 3.8(a) and $\Delta = 1.3$ for $We = 83.0$ in Fig. 3.8(c). However, they are physically available for studying the B effects on the hypergolic ignition problem.

The results show that the non-monotonic variation of IDT with increasing B from 0.0 to 0.7 is a general characteristic that can be observed for most of the cases. For example, for size ratios of 1.3 and 1.6, the IDT first decreases to a minimum value with B reaching at about 0.3, and then increases as increasing B, although the B having the shortest IDT might slightly vary for different cases. It is also noted that $\Delta = 2$ at small Weber numbers, namely $We = 41.0$ and 60.9, the IDT decreases monotonically as increasing B from 0.2

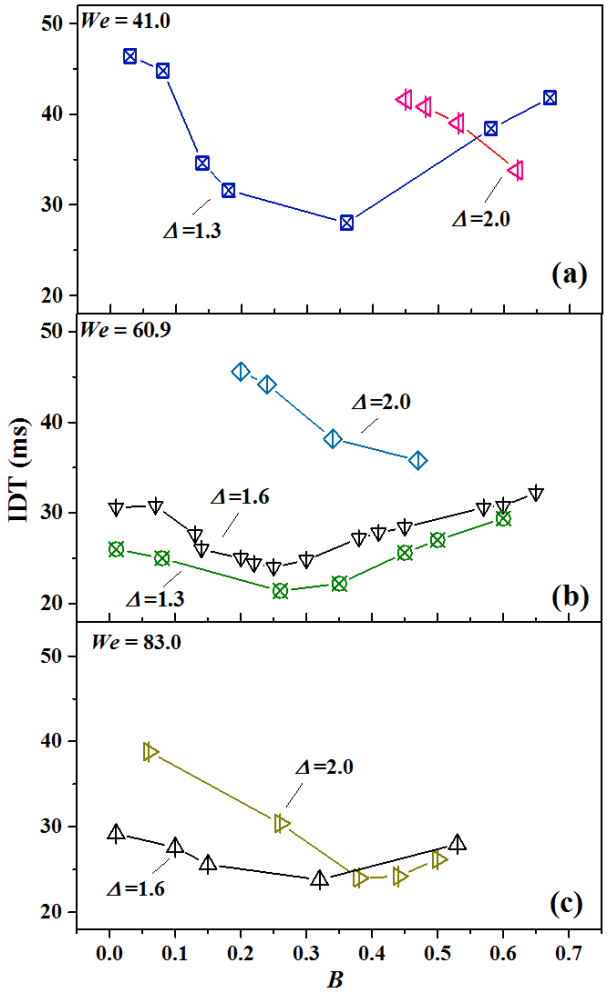

Figure 3.8. Dependence of IDT on impact parameter for various Wes and Δs with (a) $We = 41.0, \Delta = 1.3$ and $\Delta = 2.0$; (b) $We = 60.9, \Delta = 1.3, 1.6$ and $\Delta = 2.0$; (c) $We = 83.0, \Delta = 1.6$ and $\Delta = 2.0$.

to 0.6. However, the non-monotonicity can be observed again when increasing the We to 83.0. This can be understood as that, on the one hand, the large size ratio of 2.0 has been quite deviated from the chemical stoichiometry of the liquid-phase reactions that tend to be non-ignitable; on the other hand, too large B leads to the stretching separation and less mass interaction so that the hypergolic ignition cannot happen as well, however, the liquid-phase reactions accompanied by the internal mixing can be enhanced by increasing We,

which makes the non-monotonic variation of IDT reoccur for $\Delta = 2$ at larger We as increasing B. In fact, the IDT of non-ignitable cases can be treated as infinitely long, therefore we can argue that the non-monotonic variation of IDT with varying B is a general characteristic for all off-center droplet collisions once the ignitable preconditions are satisfied.

3.7.2 Regime nomogram of Ignitability

In order to study the B effects on the hypergolic ignitability of off-center droplet collision, a large number of experiments have been conducted and presented in the $We - B$ parameter space for two size ratios $\Delta = 1.6$ and $\Delta = 2.0$, as shown in Fig. 3.9.

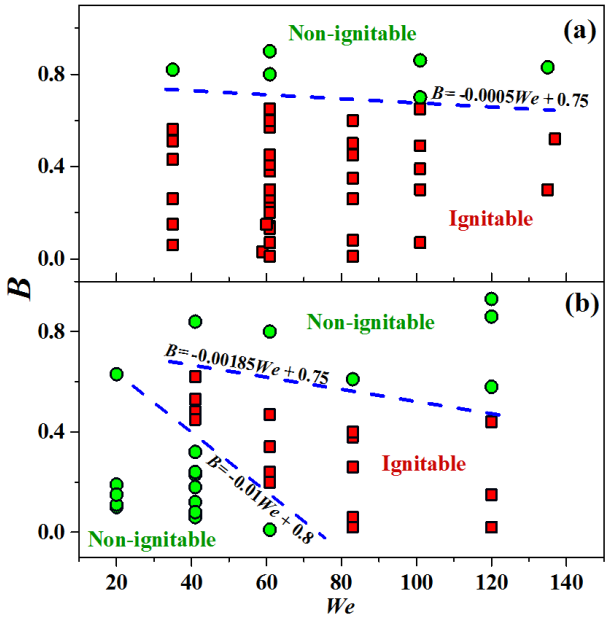

Figure 3.9. Ignitability regime nomogram in $We - B$ parameter space with (a) $\Delta = 1.6$ and (b) $\Delta = 2.0$.

For $\Delta = 1.6$ in Fig. 3.9(a), an approximately straight line, fitted as $B = -0.0005We + 0.75$, separates the $We - B$ subspace of $We = 20 - 140$ and $B = 0.0 - 1.0$ into two regimes: the ignitable regime below the line and the non-ignitable regime above it. The negative slope of the fitted regime boundary line shows that increasing We at a certain large B tends to result in non-ignitability, which is different to the regime nomogram in the $We - \Delta$ parameter space for head-on droplet collision [66] that the hypergolic ignitability favors small Δs and large Wes. That is because increasing We for head-on droplet collision promotes the internal mixing and reactions while increasing We for off-center collision with large B weakens the mass interaction and reactions by the stretching separation. The different ignitability regime relies on the competence between the above two factors.

For $\Delta = 2.0$ in Fig. 3.9(b), except a similar regime as $\Delta = 1.6$ divided by an approximately straight line fitted as $B = -0.0018We + 0.75$, another approximately straight line, fitted as $B = -0.01We + 0.8$, is observed with the contrary results that the ignitable regime above the line and the non-ignitable regime below it. This regime line is located at small B and small We area, which means increasing B and We for slightly off-center droplet collision would promote the hypergolic ignition.

3.8. Concluding Remarks

Hypergolic ignition of the head-on collision between a smaller TMEDA and a larger WFNA droplet at various Wes and Δs had been studied systematically in authors' previous work, indicating the ignitability and ignition delay times are critically rely on the heat release from the liquid-phase reactions accompanied by the effective droplet internal mixing during earlier stages. Regardless of We and Δ effects, the previous results show that the non-monotonic droplet mixing rate could be observed for off-center collision of significant practical relevance with varying B. With this motivation, the experiments have been extended from head-on collision to off-center collision for various B by focusing on understanding the influence of B on the ignition delay time and ignitability. The present study was performed experimentally by using a collision apparatus equipped with a time-solved shadowgraph on a representative case at $We = 60.9, \Delta = 1.6$ for various B with a fixed $Oh = 2.5 \times 10^{-3}$. The ignition delay time is identified, with an uncertainty of less than 0.2 ms, by the grayscale level analysis on the shadowgraph images.

Compared with the head-on collision between TMEDA/WFNA droplets, the hypergolic ignition of slightly off-center collision is distinguished and clearly seen in the phenomenon description of shadowgraphs. The grayscale level analysis accurately shows that both rapid vaporization stage and subsequent hypergolic ignition for $B = 0.3$ are

advanced based on the explanation of enhanced internal mixing. The enhancement of mixing can be understood as that, the impact inertia for slightly off-center collision can be divided into two parts, namely reflexive and stretching inertias. As increasing the impact parameter, the stretching inertia increases while the reflexive inertia decreases with the translational energy transferring into the rotational energy. Once the stretching effects have increased to comparable to that of reflexive effects, the droplet would prefer to coalescence for promoting the long-time internal mixing.

With further increasing B, the stretching inertia keeps increasing and dominant over reflexive inertia, leading to stretching separation and completely different hypergolic ignition. The locally well mixed area around the filament and satellite droplets could result in fast vaporization at the beginning, however, the subsequent stretching separation restrains the amount of interaction mass to release sufficient heat for the further vaporization, leading to the increase of IDT for moderately off-center collision with $B = 0.6$ and final non-ignitability for nearly grazing collision with $B = 0.9$.

The effects of impact parameter on hypergolic ignition can be understood as the competence between stretching and reflexive impact inertia. The stretching effect promotes the internal mixing and shorten the IDT for slightly off-center droplet collision, but it turns to suppress the interaction mass and internal mixing at large B, resulting in the non-

monotonic variation of internal mixing and IDT as increasing B from 0 to 1. The correlation between internal mixing and IDT was further verified by the definition of mixing index quantitatively.

Besides, the experiments have been extended to other Weber numbers ($We =$ $41.0, 60.9$ and 83.0) and size ratios ($\Delta =$ $1.3, 1.6$ and 2.0), showing that the non-monotonic variation of IDT with varying B is a general phenomenon as the IDT can be treated as infinitely long for some cases involving non-ignitability at large B. The ignitability nomogram in $We - B$ parameter space illustrates the hypergolic ignition in favors of small Bs, and increasing We promotes ignition at small B because of the enhanced mixing while suppresses ignition at large B owing to the stretching separation.

The impact parameter effects enrich the observations that missed by head-on collision between TMEDA/WFNA droplet, however, the present study only focused on the impact parameter effects for limited Weber numbers and size ratios. The above considerations urge a future systematic study on the We and Δ effects for off-center collision. Besides, the Ohnesorge number is fixed so that the effects of viscosity remain to be characterized.

4. Droplet size effects on multiple time scales during the hypergolic ignition

4.1. Introduction

In order to focus on quantifying the effects of droplet collision and mixing dynamics [8, 37, 42] on the hypergolic ignitability and IDT and to avoid dealing with many factors at one time, the previous work of the authors deliberately limits its scope to studying the effects of We and Δ by fixing d_O=1.45mm in Chapter 2 and Chapter 3. The ignitability regime nomogram in the parameter space of $We-\Delta$ shows that the hypergolic ignition favors large We (for enhanced droplet mixing which facilitates the subsequent heating and vaporization processes) and small Δ (for more adequate liquid-phase reactions which required appropriate fuel/oxidizer volume ratio). For the same reason, the IDT has an overall tendency of decreasing with increasing We, although it exhibits a non-monotonic variation at intermediate We, hypothetically being attributed to the non-monotonic emergence of jet-like mixing pattern with increasing *We* [48]. The effects of Δ on IDT can be understood from two aspects: increasing of Δ facilitates the internal mixing and hence favors the ignition; increasing of Δ deviates the binary system cubically from the chemical stoichiometry of the liquid-phase reaction thus suppresses the ignition.

In spite of the above worthy results, which reveal the controlling effects of collision dynamics and intermixing on the hypergolic ignition of TMEDA/WFNA, the effects of droplet size (other than those of the size ratio) were not considered, and therefore the correctness of the above results under more general and practically useful situations merits the present study. In the previous study, interesting preliminary results have been reported that no ignition was observed for smaller WFNA droplets ($d_O = 0.3\,mm$) while other parameters retained unchanged. To explain the phenomenon, a hypothesis was made but not verified that, if the droplet sizes are too small, the liquid-phase reactions may not generate sufficient amount of heat to vaporize the liquids. In addition, it was further hypothesized that the large surface-volume ratio of smaller droplets increases the heat loss to the environment, again slowing down the liquid vaporization. It is noted that the hypergolic ignition by droplet collision occurs in cold environment, the merged droplet is heated from its interior instead of from a hot environment. The physical understandings to the classical "d^2-law" droplet vaporization and burning cannot be directly applied to the present problem.

4.2. Experimental specification

The schematic of the experimental apparatus used in the present study has been expatiated in Chapter 2 and therefore will not be repeated here. Some specifications about the setup and operations are provided as follows. Particularly, the dispensing method and frequency for TMEDA and WFNA droplets are the same with those in the experiments in Chapter 2. The high speed camera is still the main measurement method and the data analysis is still based on the grayscale level analysis under the same accuracy. The uncertainty of droplet trajectories from head-on collision is measured by the impact parameter, $B = x/L < 0.1$, where x is the projection of the separation distance L between the droplet centers in the normal direction to the relative velocity.

Diversity of WFNA droplet sizes are realized by precisely adjusting the dispensing pressures in which the smallest droplet size is generated by the breakup of the liquid jet with a diameter slightly larger than the nozzle orifice. The TMEDA droplet sizes are mainly controlled by the orifice of the micro-valves and slightly dependent on the dispensing conditions, i.e. dispensing frequency and pressure. In order to avoid the interaction between the neighboring ignitions, the frequency for dispensing TMEDA droplet were controlled no more than 3Hz.

In the present study, the size of WFNA droplets can vary from 0.9 mm to 1.5mm instead of being fixed at 1.45mm as in Chapter 2 and Chapter 3. Such a variation of WFNA droplet size was found to be sufficiently large to produce distinct phenomena to be presented and analyzed in the following sections, while it is sufficiently small to rule out the possible influence of Ohnesorge number, $Oh = \mu_O/\sqrt{\rho_O \sigma_O d_O}$, a dimensionless measure of droplet viscosity (μ). It is recognized that the fluid-dynamic influence of viscosity on the droplet coalescence and mixing and in turn the hypergolic ignition is not negligible [66]. However, Oh is substantially small as being of $O(10^{-3})$ in the present problem and varies too slightly (by less than 30%) to cause any significant difference.

4.3. Phenomenological descriptions of hypergolic ignition

Figure 4.1 shows the time-resolved shadowgraph images of the hypergolic ignition induced by binary collision of droplets for various d_O =1.3mm, 1.1mm and 0.9mm. In the three cases, $We = 61$ and $\Delta = 1.5$ are fixed so that comparison can be made with the representative case described in detail in the previous study [66], where We and Δ are the same but $d_O = 1.45$ mm. It is noted that different reference lengths were employed in the images for a clear presentation of the entire processes, which spatially expand from

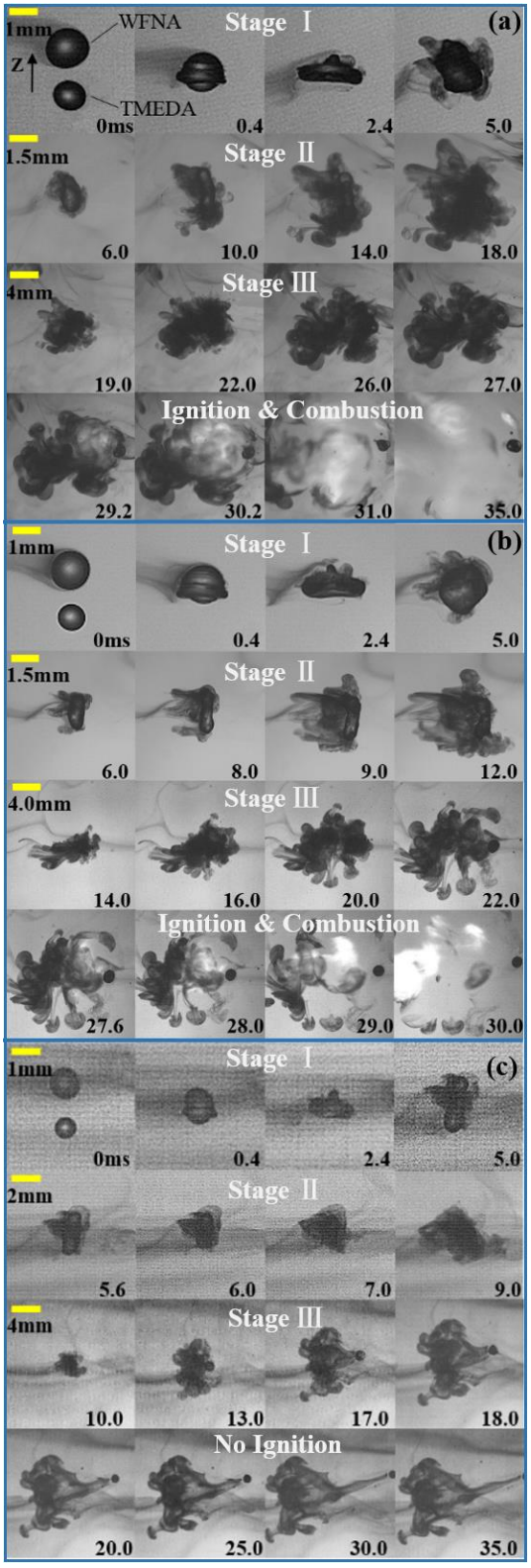

Figure 4.1. Shadowgraph images of the hypergolic ignition by droplet collision at *We* = 61 and $\Delta = 1.5$. WFNA droplet diameter d_O is (a) 1.3mm, (b) 1.1mm, and (c) 0.9mm.

$O(10^{-1})$ mm to $O(10)$ mm. In spite of the size variation, the three pre-ignition stages summarized in the Introduction can still be observed:

In Stage I, the two droplets collide and deform with clear droplet surfaces that are similar to those exhibited in collision of nonreactive droplets [37]. Moreover, the time duration is almost the same for Stage I, which ends at near 5.0 ms for all three cases. This implies that the dynamics of droplet collision and mixing in Stage I follows the fluid dynamic similarity, and droplet sizes enter the problem through the non-dimensional parameters such as We and Δ.

In Stage II, as the merged droplet being heated up by the exothermic liquid-phase reactions, opaque vapor is emitted outwardly from the droplet surface, which is gradually concealed, as shown from 6.0ms to 18.0ms in Fig. 4.1(a). An interesting observation is that, for the case of d_O= 0.9mm shown in Fig. 4.1(c), the droplet surface has already been mostly blurred at 9.0ms, which is earlier than the 12ms for the case of d_O = 1.1mm in Fig. 4.1(b) and than the 18ms for the case of d_O = 1.3mm in Fig. 4.1(a). This indicates that decreasing the size results in faster Stage II, probably because the smaller droplet is more readily to be heated up.

In Stage III, the droplet vaporization becomes significantly faster for all the three cases. Compared with those in Stage II, the shadowgraph images in Stage III must be

zoomed out by about three times to show the entire process. The size effect on the duration of the stage is not evident but the eventual ignition, characterized by the emergence of luminous flame kernel, occurs at 27.6 ms for the case of $d_O = 1.1$mm, being earlier than that for the case of $d_O = 1.3$mm. In addition, the ignition does not occur for the case of $d_O = 0.9$mm, showing that the small reduction of the droplet size by 30% is enough to bring the system from ignitability to non-ignitability.

4.4. Size effect on hypergolic ignitability

Comprehensive parametric study was conducted over wide ranges of We from 20 to 100 and of d_O from 0.9mm to 1.5mm, for Δ being 1.3 and 1.5. A regime nomogram for hypergolic ignitability in $We - d_O$ space is shown in Fig. 4.2.

For $\Delta = 1.3$, a fitted curve divides the $We - d_O$ parameter space into two regimes with the ignitable regime being above the curve and the non-ignitable regime below. According to the nomogram, it is evident that the ignition favors higher We as the size d_O decreases, implying that reducing the droplet size tends to suppress the ignition and therefore a larger *We* is required to promote the intermixing and reactions between the fuel and oxidizer droplets. For $\Delta = 1.5$, the same observations can be made to the size effect

on the ignitability. At the larger size ratio, the non-ignitable regime is slightly extended to higher We, which is consistent with the previous results.

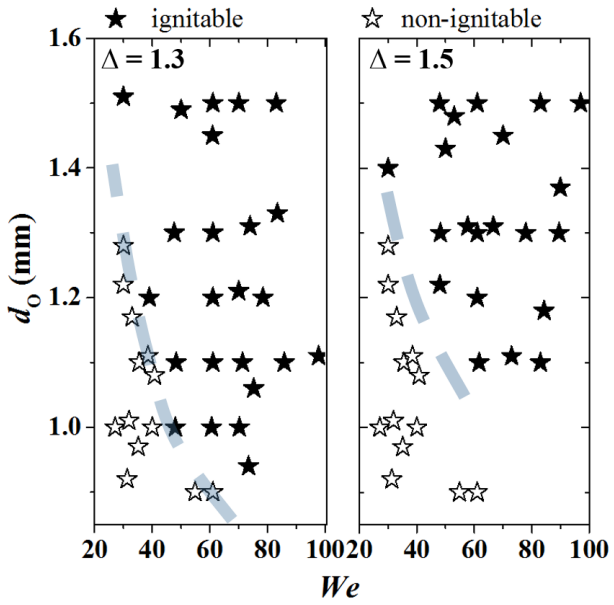

Figure 4.2 Ignitability regime nomogram in $We - d_O$ parameter space for Δ = 1.3 and Δ = 1.5.

4.5. Size effect on hypergolic Ignition Delay Time

4.5.1 Precise Determination of IDT by grayscale analysis

A certain degree of arbitrariness always exists in the definition of an ignition delay time, and the "go, no-go" definition [5], based on the emergence of luminous ignition kernel, is not precise enough for our purpose of quantifying the size effect. To accurately determine the ignition delay time, a method based on the analysis of grayscale levels on the shadowgraph images, which has already been employed and verified in our previous study[66], is adopted and briefly summarized as follows.

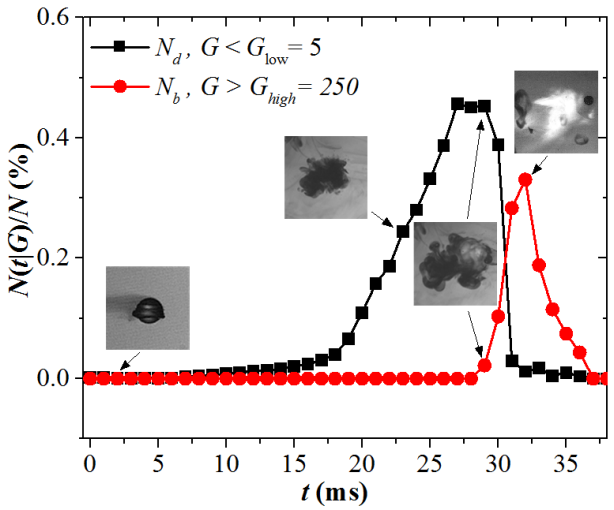

Figure 4.3 Precise determination of IDT by grayscale level analysis for the case (a) in Fig. 4.1.

The grayscale in a shadowgraph image can be divided into 256 levels denoted by G, in which $G = 0$ corresponds to the completely opaque and $G = 255$ to the completely bright. Following the same criterion adopted in our previous study [66], the grayscale of the image background is defined by $G = 100$, the luminous ignition kernel by $G > G_{\text{high}} = 250$, and the opaque vapors by $G < G_{\text{low}} = 5$. The total number of pixels on an image is counted as N, that of the luminous kernel as N_b, and that of the opaque vapors as N_d. Therefore, the ignition occurrence is identified by an abrupt rise of N_b/N with time, as shown in Fig. 4.3. As an example, the IDT for the case (a) in Fig. 4.1 can be unambiguously determined as 29.0ms, when N_b/N starts to rapidly rise while N_d/N starts to suddenly drop. The grayscale analysis method has been verified by the measurements of infrared

radiation and visible light intensity to be insensitive to the thresholds, G_{high} and G_{low}, with the uncertainties no more than 0.2ms [66].

4.5.2 Decrease of IDT with droplet size reduction

Figure 4.4 shows the variation of IDT with We at $\Delta = 1.3$ and 1.5 and for various d_O. Consistent with the previous findings [66], the IDT generally tends to decrease with increasing We, because of the mixing enhancement of TMEDA and WFNA within the merged droplet. Furthermore, the slightly non-monotonic variation of IDT over We for the case of $d_O = 1.5$mm can be inferred as the non-monotonic emergence of the "jet-like" internal flow within the merged droplet[48].

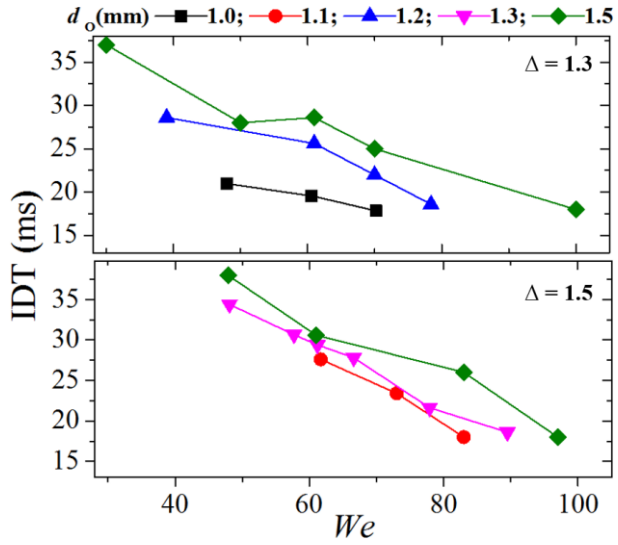

Figure 4.4 Variation of IDT (in ms) with We at Δ = 1.3 and Δ = 1.5 and for various d_O of 1.0mm, 1.1mm, 1.2mm, 1.3mm and 1.5mm.

As shown in Fig. 4.4, at a first glance, the shrinking of the droplet size tends to reduce the IDT as indicated by the falling of the curves characterizing dependence of IDT upon We as decreasing d_O. Nevertheless, it should be recalled that the ignition cannot be achieved for the case of $\Delta = 1.5$ with $d_O = 1.0$ mm, verifying that the reduction of droplet size tends to suppress the ignition as indicated in the regime diagram of Fig. 4.3. It is recognized that the above seemingly conflicting size effects on the ignition delay time and the ignitability are caused by using dimensional times (in ms), which may distort the correct physical pictures of flow similarity. The various pre-ignition processes occur on different time scales, as have been described in Section 4.3, and consequently their dependences on the droplet size are controlled by different physicochemical laws. In the following section, we shall conduct a time scale analysis to the pre-ignition processes to resolve the size effects.

4.6. Time scaling analysis of pre-ignition processes

4.6.1 Characteristic time scales of pre-ignition stages

As discussed in Section 3, Stage I is dominated by the fluid dynamic processes of droplet collision, deformation and intermixing, the thermal and chemical processes being negligible. The characteristic time scale for Stage I, denoted by τ_I or τ_{impact}, can be

formally written as a function of the controlling flow similarity parameters, such as We and Δ in the present problem,

$$\tau_I = \tau_{\text{impact}} = f(We, \Delta) \tag{4.1}$$

It is seen that τ_I is the same for a given set of these non-dimensional parameters, through which d_O exerts its influence.

Stage II is dominated by the thermophysical process that the heat generated by the liquid-phase reactions is transferred from the interior to the surface, thus the characteristic time scale for this stage, denoted by τ_{II} or τ_{heating} is estimated by

$$\tau_{II} = \tau_{\text{heating}} \sim d_O^2/\left(\lambda_l/\rho_l c_{v,l}\right) \tag{4.2}$$

where λ_l is the heat conductivity, ρ_l the density, and $c_{v,l}$ the constant-volume heat capacity of the liquid phase.

Stage III is characterized by the rapid vaporization, which results in a considerable regression of the droplet surface, and therefore the characteristic time scale of vaporization, denoted by τ_v, is estimated by [5]

$$\tau_v \sim d_O^2/\left(\lambda_g/\rho_l c_{p,g}\right) \tag{4.3}$$

Where λ_g is the heat conductivity and $c_{p,g}$ the constant-pressure heat capacity of the gas phase. We hypothesized that the heat loss, such as convective cooling, is significant with

decreasing the droplet size and hence increasing the surface-volume ratio. Therefore we can estimate the time scale characterizing the cooling process, denoted by τ_c, in the form of [5]

$$\tau_c \sim \frac{c_{p,g}\rho_g}{(S/V)h} \tag{4.4}$$

where ρ_g is the density of the gas phase, $S/V \sim 6/d_O$ the surface-volume ratio of the droplet considered, and h the phenomenological convection heat transfer coefficient, which is correlated with the Nusselt number through $h = Nu\lambda_g/d_O$. By approximating the droplet as a sphere, the Nusselt number is related to the Reynolds number, $Re = \rho_g U_l d_O/\mu_g = O(10) - O(10^2)$, by $Nu \sim Re^{1/2}$ [5], where U_l refers to the velocity of the merged droplet in the gas phase, μ_g the dynamic viscosity of the gas phase. Therefore, the coefficient h depends on the droplet size as $h \sim \lambda_g\left(U_l/d_O\nu_g\right)^{1/2}$, substituting of which into Eq. (4) we obtained

$$\tau_{\mathrm{c}} \sim \frac{\rho_g c_{p,g}}{6\lambda_g}\left(\frac{\nu_g}{U_l}\right)^{1/2} d_O^{3/2} \tag{4.5}$$

To account for the heat loss in Stage III, the characteristic time scale of the stage can be estimated by means of geometric average of the characteristic time τ_v and τ_c, i.e.

$$\tau_{\mathrm{III}} \sim \sqrt{\tau_{\mathrm{v}}\tau_{\mathrm{c}}} \sim \frac{c_{p,g}}{\lambda_g}\sqrt{\frac{\rho_l}{6}}\left(\frac{\rho_g^2\nu_g}{U_l}\right)^{1/4} d_O^{7/4} \tag{4.6}$$

To sustain the vaporization with heat loss, the vaporization rate should be larger than the cooling, requiring $\tau_v < \tau_c$. Therefore, the geometric average results in $\tau_{III} > \tau_v$, indicating that the vaporization slows down due to the heat loss.

By use of Eq. (6), we can estimate the surface regression rate, K_r, characterizing the vaporization process as

$$K_r \sim \frac{d_O^2}{\tau_{\mathrm{III}}} \sim \frac{\lambda_g}{c_{p,g}} \sqrt{\frac{6}{\rho_l}} \left(\frac{U_l}{\rho_g^2 \nu_g} \right)^{1/4} d_O^{1/4} \sim d_O^{1/4} \tag{4.7}$$

It is noted that the contribution of natural convection to the cooling effect was assumed to be negligible compared with that of the forced convection where $Re = O(10) - O(100)$ where in the above scaling analysis. Because of the small droplet size (about 1mm) and small temperature rise $\Delta T/T = O(10^{-1}) - O(1)$ prior to ignition, the Grashof number $Gr = \left(g d_O^3/\nu_g^2\right)(\Delta T/T) = O(10^{-1}) - O(1)$, which has insignificant influence on the convection [5],

4.6.2 Size effects during pre-ignition stages

As discussed in Section 4.5, the number of pixels with $G < G_{\mathrm{low}}$, N_d, can be approximately regarded as the occupied area of the vapor. Consequently, the volume occupied by the vapor can be estimated by $\alpha_N N_d^{3/2}$, where α_N characterizes the geometry

effect, and $(N_d/N)^{3/2}$ can be used to approximately measure the total volume of the accumulated vapor around the merged droplets as the result of vaporization.

To elucidate the size effects on the time scales of the pre-ignition processes and accordingly on the IDTs, we reanalyzed the three representative cases (presented in Fig. 4.1) at We = 61 and Δ = 1.5 for different d_O by using the results from the above time scaling analysis. As seen in Fig. 4.5(a), if the physical time scale is adopted, the time lapses of Stage I for different droplet sizes are almost the same, as have been discussed in Section 3. The size effect in Stage I is through the flow similarity parameters, such as We and Δ, which are fixed for the three cases. The obvious deviations of the three cases in Stages II and III can be understood by that the physical time scales change with the droplet sizes.

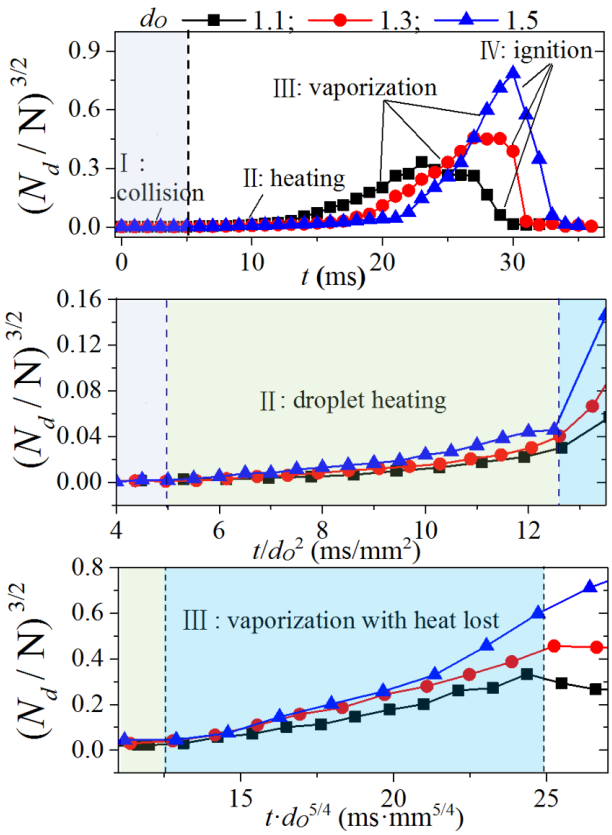

Figure 4.5 Size effects on the time scales of the pre-ignition processes at *We* = 61 and Δ = 1.5 for various d_O of 1.1 mm, 1.3mm and 1.5mm.

In Stage II, $(N_d/N)^{3/2}$ has a slight increase for all the three cases, as shown in Fig. 4.5 (a), because the heat generated by the liquid-phase reaction is being transferred to the surface, where the temperature is not sufficiently high for vaporization. It is seen that the time lapse of Stage II is shorter for the smaller droplet, which can be hypothetically contributed to the shorter characteristic time for heating, as indicated $\tau_{II} \sim d_O^2$ in Eq. (2). To verify this hypothesis, we replotted Stage II in Fig. 4.5(b) by using scaled time, t/d_O^2, according to Eq. (2). As we anticipated, all the curves corresponding to different droplet

sizes almost collapse into one curve, substantiating the correctness of the time scaling estimation.

In Stage III, $(N_d/N)^{3/2}$ has a sudden increase due to rapid vaporization, which is characterized by a large slope of the curves in the physical time, as shown in Fig. 4.5(a). The accumulation rate of the vapor, $\dot{m}_g$, which can be described in terms of the surface regression rate of the droplet, is estimated by $\dot{m}_g = -(6\rho_l/\pi)(\mathrm{d}/\mathrm{d}t)(d_O)^3 \sim K_r d_O$, which, together with Eq. (7), yields, $\dot{m}_g \sim d_O^{5/4}$, indicating that the characteristic time, τ_g, for vapor accumulation could be scaled by $d_O^{-5/4}$, which is verified by the collapsed curves of $(N_d/N)^{3/2}$ for all the three cases, as shown in Fig. 4.5(c).

Based on the above discussion, we can conclude the size effects on the IDTs by examining and comparing the effects on each pre-ignition process. First, the time duration of Stage I is determined by the non-dimensional collision parameters, We and Δ, through which the droplet sizes affect the entire hypergolic processes. Second, the time duration of Stage II is additionally affected by the physics of droplet heating, which give rise to a size-dependent time scale, $\tau_{II} \sim d_O^2$, to the problem. For smaller droplets, the reduced droplet heating time tends to cause a shorter IDT. Third, the time duration of Stage III is controlled by the droplet vaporization accompanied by heat loss due to convective cooling, whose time scale is a weaker function of the droplet size, $\tau_g \sim d_O^{-5/4}$. For smaller droplets, the

decreased vaporization rate results in a prolonged vaporization stage, and hence tends to cause a larger IDT. Consequently, with fixed We and Δ, decreasing d_O would cause a substantially shorter Stage II and moderately longer Stage III, which combined to result in a shorter IDT. However, further decreasing d_O to sufficiently small value would significantly increase the heat loss in Stage III, which results in insufficiently accumulated vapor in gas phase, leading to non-ignition.

4.7. Concluding remarks

Droplet size effects on the hypergolic ignition by head-on collision of TMEDA and WFNA droplets was experimentally studied and theoretically analyzed. The hypergolic ignitability of the system is characterized by a regime nomogram in the $We - d_O$ parameter space, indicating that decreasing the droplet size (d_O) seems to suppress the ignition so that a larger We or a smaller Δ or both together is favored for ignition. However, the experimentally observed ignition delay time at fixed We and Δ decreases with the droplet size, seemingly implying an opposite size effect on the ignition.

Time scaling analysis to the three pre-ignition stages reveals that the first stage of droplet collision does not attribute to the observed size effects because it is dominantly affected by We and Δ; the second stage of droplet heating is quadratically shortened by

reducing the droplet size, consequently causing a shorter ignition delay; the third stage of droplet vaporization with heat loss is prolonged by reducing the droplet size though a scaling of $d_O^{-5/4}$ if d_O is not too small to cause non-ignition by the substantially increased heat lost.

5. Hypergolic ignition induced by droplet collision of hydrogen peroxide and ethanolamine solution of sodium borohydride

5.1 Introduction

Being indispensable in space missions, the propulsion system in modern rocket engines has been required to be able not only to fulfill the propulsive task, but also to reduce the cost, lead time and risk [21]. Under such consideration, selecting and operating appropriate propellants for modern rocket become more and more essential and necessary, as the conventional utilized propellants, such as hydrazine and its derivate, usually cause serious technical problems and request complicate the design of the rocket engine due to the high level of toxicity [74]. A number of alternative have been developed and tested [74], for example, TMEDA, which has been well studied in terms of the droplet collisions in previous chapters. Nevertheless, the corresponding oxidizer WFNA is extremely corrosive to facilities and dangerous to the human beings.

Drawing great attention for the space propulsion, the non-toxic hypergolic bipropellants has been regarded as a fundamental solution to the seemingly insurmountably technical difficulties when using conventional fuels and oxidizers. One promising candidate of non-toxic oxidizer is the hydrogen peroxide (H_2O_2), which was well applied to the aerospace propulsion system long before[22, 75]. It then had been replaced by the higher performing chemistries such as the conventional hypergolic chemicals, hydrazine and its variants due to the decomposition of H_2O_2 and the relatively low specific impulse. However, recent test data of H_2O_2 has shown that the chemical is indeed appropriate for use as a propellant fluid and it is suggestive that the stability of it could be improved by improving the purity and adopting more compatible materials for the containers [22].

Together with H_2O_2, a non-toxic energetic fuel also is in desire. Up to date, the non-toxic propellant fuel corresponding for H_2O_2 could be made either by adding catalyst agent to the fuel or by blending a light metal hydride between which and H_2O_2 the violent reduction-oxidation reaction would release large amount of heat and hence trigger the ignition[76]. In the latter method, the metal hydride in fact serves as an ignition source. Compared with the catalyst, the light metal hydrides become more promising as an alternative for advanced propulsion system because it could provide higher specific impulse and relatively short ignition delay.

A variety of strongly reducing agents could be nominated as the ignition source, such as lithium hydrides, lithium-aluminum hydrides, and sodium borohydrides[76]. Among them, sodium borohydrides ($NaBH_4$) is regarded as an attractive one since the utilization will benefit a lot [77]. First, with a relatively low molecular weight, $NaBH_4$ is most economic type of metal hydrides. Furthermore, there are various kinds of compatible hydrocarbon solvents with this type of ignition source. In addition, it is safer and easier for handling compared to others.

The solvent for $NaBH_4$ particles in the present study was selected to ethanolamine under the following reasons. First, ethanolamine itself is a propellant fuel that has been well used in rocket propulsion missions [78]. Second, as already been tested, $NaBH_4$ has a considerable solubility (10% for maximum) in ethanolamine [79]. Third, the dark vapors shown in ignition by WFNA and TMEDA droplet are dramatically suppressed due to the low vaporization pressure of ethanolamine, so that the interaction between the fuel and oxidizer droplets can be clearly seen, which is of great benefit for the investigation of ignition process, as depicted in the flowing sections.

5.2 Experimental Specifications

The experiment of hypergolic ignition induced by the binary collision of droplets of H_2O_2 and ethanolamine mixed with sodium borohydride was conducted on the same experimental setup as depicted in Chapter 2. However, because of the physical property and the ignition characteristics of this combination of hypergolic propellants are quite different with that in WFNA/TMEDA, several modifications were made at the preparation of the fuel and oxidizer and the experimental operations.

"Rocket grade" hydrogen peroxide (RGHP) with purity as high as 92% had been adopted in the present experiment. The RGHP was stored carefully in containers so that the self-decomposing reaction in the tank is negligible. To avoid the self-decomposition during the transportation and dispensing through the micro valves, the testing liquid tank for RGHP was kept in ice-water bath throughout the experiment where the temperature of RGHP at the outlet of the micro-valve is no larger than ten degrees centigrade.

Due to the high deliquescence of sodium borohydride at the ambient condition, it was stored in drying cabinet at a favorably constant temperature. The sodium borohydride powder was directly dissolved into the ethanolamine at 8.6 wt% in desiccant environment. The sodium-borohydride/ethanolamine was stored for two weeks before usage to ensure a complete dissolution.

As the viscosity of ethanolamine (24.1 cP) is much larger than that of TMEDA and WFNA, the droplet was generated downwardly applying the method used for WFNA but under a much higher driven pressure (80~100kPa). The size of ethanolamine droplet will decrease if the driving pressure increase, however, the uniformity of the generating droplet sizes cannot be guaranteed any more due to the instability of the jet broken-up, which would absolutely add dilemma into the experiment. In addition, since the generation frequency of fuel droplet is promoted, the frequency for generating the oxidizer droplet was controlled elaborately to prevent the interference between the neighboring ignition events. The generating frequency of ethanolamine solution droplet is around 10Hz, while that for H_2O_2 droplet is limited within 2~3Hz.

5.3 Phenomenological description of hypergolic ignition

By applying the above experimental setup, a number of groups of tests in which RGHP and ethanolamine solution of sodium borohydride mix with each other in terms of their freely motional droplet collisions have been conducted. The collision We varies from 20 to 100, based on the physical properties of RGHP, and the fuel/oxidizer droplet size ratio $\Delta = 1.0 - 2.2$, in which the diameter of RGHP droplet is fixed at 0.8mm. Lager fuel

droplet than oxidizer droplet is under the consideration of the stoichiometric ratio between the RGHP and ethanolamine.

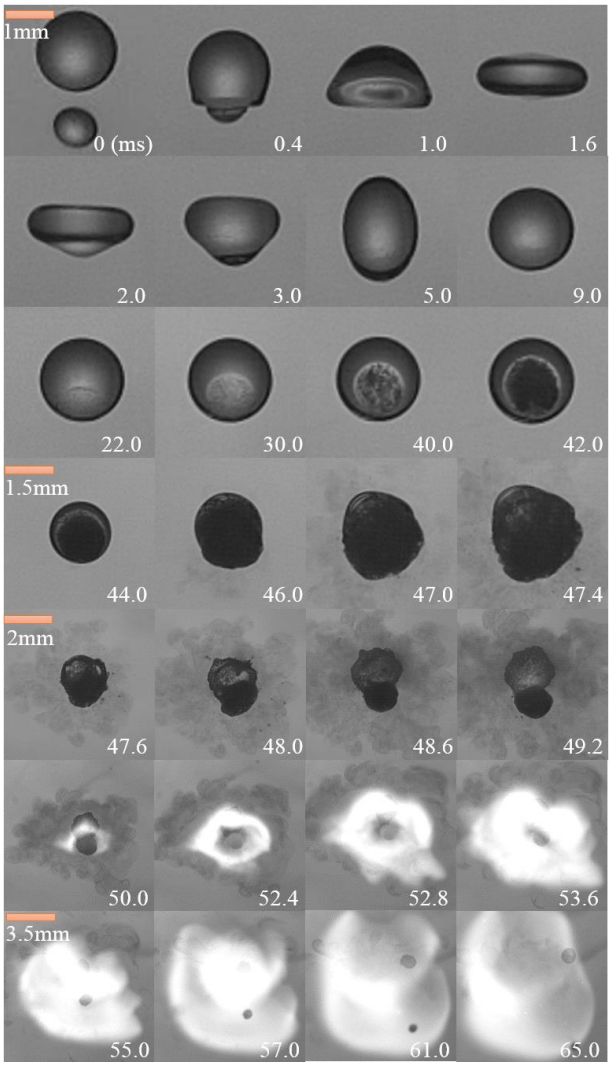

Figure 5.1 Shadowgraph images of the hypergolic ignition by droplet collision of H_2O_2 and $NaBH_4$ at *We* = 31 and $\Delta = 1.75$.

Similar to Chapter 2, the shadowgraph images of a benchmark case are first presented at $We = 31$ and $\Delta = 1.75$, as shown in Fig. 5.1. Conventionally, multi-length reference was also applied herein. Although distinction exist in the hypergolic ignition

process by RGHP and ethanolamine droplets, it is still applicable to describe the ignition herein by using the five stages similar to those adopted for ignition of TMEDA/WFNA.

Stage I: (0ms – around 9.0ms), the droplet collision and deformation period. This stage mainly features collision, deformation and oscillation of the two droplets, which is similar to the interaction of two nonreactive droplets. Specifically, after impacting on each other, the combined droplet mass deform into a 'saucer' shape, as seen at 1.6ms, under the impacting kinetic energy. While a springback under the surface tension could be observed to stretch the droplet mass to separate in the direction the two droplets initially collide. Separation does not occur eventually because of the viscous dissipation within the combined droplet mass. The maximum deformation of the springback is as seen at 5.0ms, and the deformed combined mass is hauled back again under the surface tension. The two colliding droplets merge into a larger one after several oscillations through which the kinetic energy is totally dissipated. As seen at 9.0ms, the deforming merged droplet has already regressed to regular spherical shape. However, despite the large level of oscillation during Stage I, no features related to chemical reactions could be observed.

Stage II, droplet heating and internal reaction. The merged droplet is heated by the thermal energy released from the exothermic condensed phase reaction between the fuel and oxidizer. Unlike the heating stage in TMEDA/WFNA where the configuration of the

merged droplets is gradually concealed by the opaque vapors, the configuration as well as the internal reaction features can be clearly seen for RGHP and ethanolamine solution of sodium borohydride because of the high latent heat for vaporization. It is therefore beneficial for studying the mixing and reaction mode during the ignition process in the present combination of hypergolic propellants.

As shown at 22.0ms, one regime line can be identified that the interior of the merged droplet is divided into two sub-regimes in which the reactive sub-regime is near the polarity where the smaller oxidizer droplet impact into the larger fuel droplet. The region other than the reactive sub-regime characters the same as does the merged droplet in Stage I. Subsequently, the reactive sub-regime expands inside the merged droplet and the regime line becomes clearer, as shown at 30.0ms. The merged droplet continues being heated such that the chemical reactions within it become more and more violent. As shown at 40.0ms and 42.0ms, the reactive sub-regime occupies the nearly half of the interior of the merged droplet and turns to be lightproof because of the accumulation of the opaque products. It is notable that there is a sheeny ring encompassing the dark area of reactive sub-regime, as indicated on the image. One probable reason of the formation of this sheeny ring is that, in addition to the opaque product, there should also be gaseous products, i.e. oxygen from the decomposition of H_2O_2 and the hydrogen from the oxidizing reaction of

sodium borohydride, generated during the heating stage. These gas phase products would enhance the transmission of the background light. Throughout the whole Stage II, the merged droplet remains spherical indicating that the chemical reaction is still moderate.

Stage III: evaporation and breakup of the merged droplet. The merged droplet continues being heated and the chemical reaction rate promotes dramatically due to the increasing temperature. Particularly, as shown at 44.0ms, the opaque products have already occupied most of the interior area of the merged droplet. When it goes to 46.ms, the configuration of the merged droplet has been broken because of the accumulation of the products. The configuration of the droplet becomes more irregular as time goes on. Opaque product evaporates outwardly from the droplet when the surface of the droplet fractures, as shown at 47.6ms. An interesting phenomenon is that, along with the vaporization, the condensed phase product tends to be separated into two parts, as shown from 48.0ms to 49.2ms, in which one is totally lightproof and the other is much brighter. It is obvious that the lightproof part is occupied by the opaque condensed phase product, while for the bright part, one probability is the small amount of unreacted fuel that inflate with the gaseous products such as oxygen and hydrogen.

Stage IV: Ignition in gas phase. Ignition described as the luminous pixels on the shadowgraph image can be observed in this stage, as shown at 50.0ms. It is noted that flame

kernel emerges initially at the interface of the two parts and revolve around this area. The flame kernel rapidly expends outwardly overwhelming the merged droplet as shown at 53.6ms.

Stage V: Flame propagation. After being ignited, the flammable vapors are consumed speedily with an exhibition of the propagation of the flame along the vapor. In fact, more gas phase fuel and oxidizer would be released from the droplet after ignition to sustain the flame for a certain period. Two nonflammable products are eventually left originating from the two parts of the merged droplet exhibiting in Stage III.

5.4 Weber number effect on hypergolic ignition

In order to study the collision We effect on the ignition, more experiments were conducted at the same Δ but various Wes. Figure 5.2 and Fig. 5.3 are showing the shadowgraphs of the ignition process at the $\Delta = 1.75$ and $We = 41$ and 61 respectively. Compared with benchmark case, the collision Stage I for case $We = 41$ and $We = 61$ are similar that the main characteristic is just as that in droplet collision without any chemical reactions.

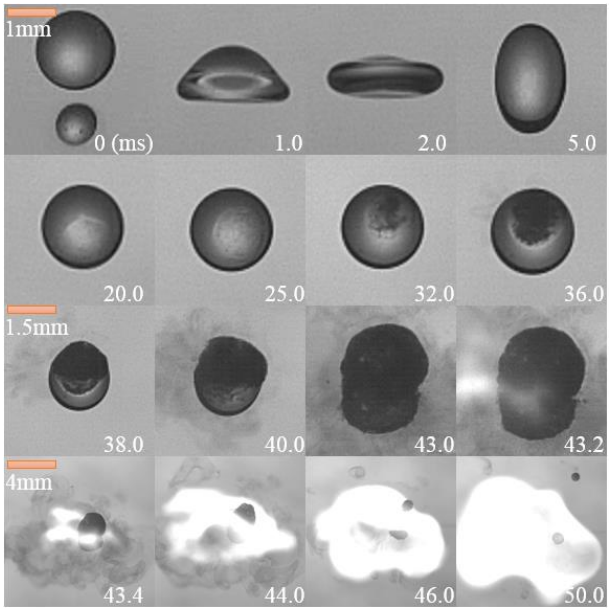

Figure 5.2. Shadowgraph images of the hypergolic ignition by droplet collision of H_2O_2 and $NaBH_4$ at *We* = 41 and $\Delta = 1.75$.

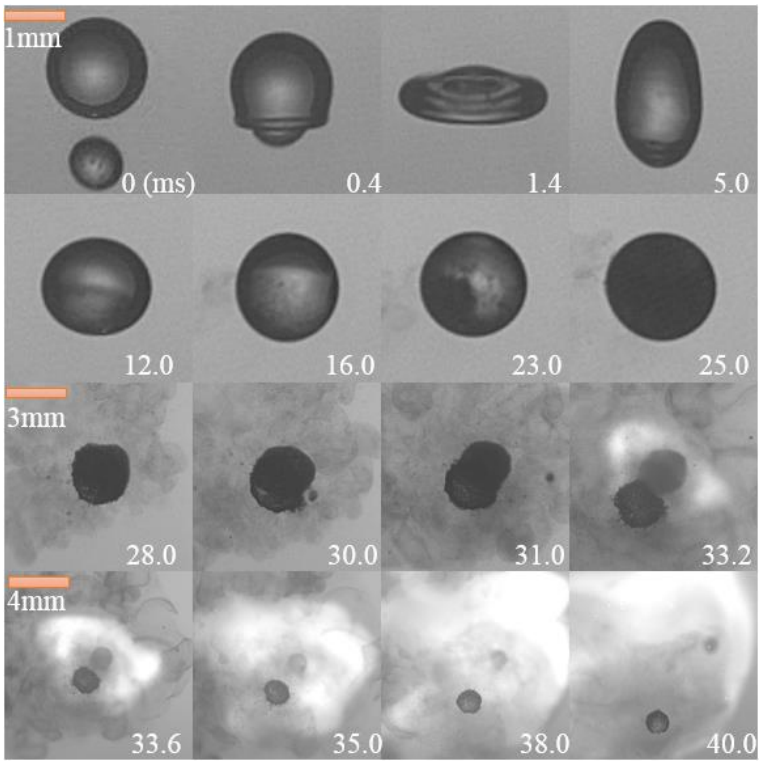

Figure 5.3 Shadowgraph images of the hypergolic ignition by droplet collision of H_2O_2 and $NaBH_4$ at *We* = 61 and $\Delta = 1.75$.

However, difference exhibits when it goes to Stage II. Particularly, the reactive sub-regimes defined in Stage II for case $We = 61$ occurs at earlier instant (as shown at 12.0ms in Fig.3) than it does in case $We = 41$, as shown at 20.0ms in Fig.2, which is in turn earlier than that in the benchmark case (22.0ms in Fig.5.1). The underlying reason is that, for larger impacting energy, the mixing between the fuel and oxidizer droplets will be so enhanced that the merged droplet is heated up at a faster rate due to the facilitated chemical reactions. Another evidence of the enhancement of the reaction is that the opaque part inside the merged droplet in case $We = 61$ has covered up the entire droplet area at 25.0ms.

The rapid vaporization and surface breakup Stage III, the ignition Stage IV and flame propagation Stage V for these two cases are similar with that in the benchmark case. The merged droplet was separated into two parts in both the two cases in both two cases. However, it is noted that the luminous flame kernel could be observed earlier with larger We, i.e. for $We = 61$, ignition appears at 33.2ms earlier than 43.2ms in case $We = 41$.

5.5 Droplet size ratio effect on hypergolic ignition

As already been verified in Chapter 2, the droplet size ratio also is an important parameter affecting the hypergolic ignition process by the droplet collisions in two aspects: firstly, from the viewpoint of dynamics of the droplet collision, the mixing pattern between

the colliding droplets will be different under diverse Δs; secondly, from the viewpoint of chemical reaction, altering the size ratio of interacting fuel and oxidizer droplet will change the equivalence ratio during the pre-ignition process. Under such consideration, we have also conducted the experiments focusing on the study of size ratio effect on the ignition induced by the RGHP and ethanolamine solution droplet collisions.

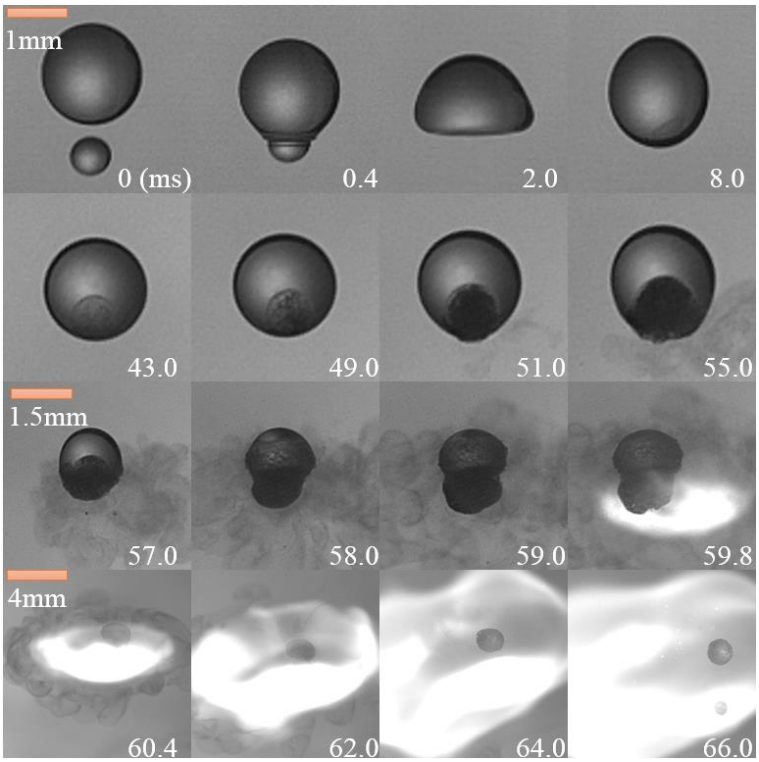

Figure 5.4. Shadowgraph images of the hypergolic ignition by droplet collision of H_2O_2 and $NaBH_4$ at *We* = 31 and Δ= 2.3.

Figure 5.4 and Fig.5.5 are showing the ignition process with $We = 31$, the same as in benchmark case, but various Δs of 2.3 and 1.3 respectively. Again, the features of Stage I in these two cases are similar with that in collisions with no reactions.

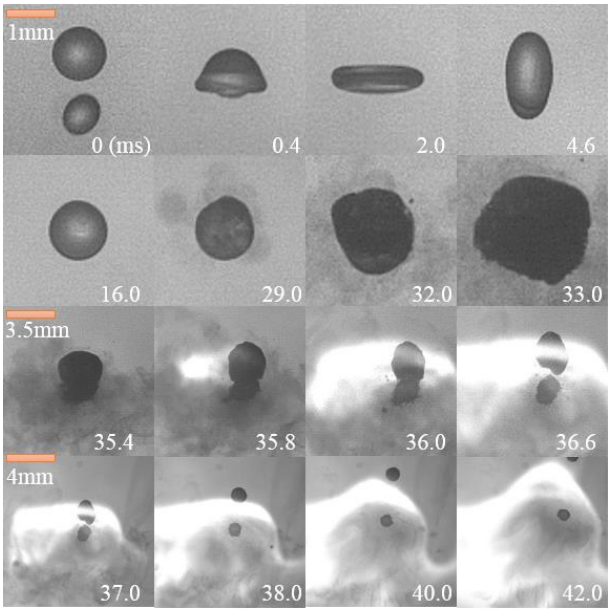

Figure 5.5 Shadowgraph images of the hypergolic ignition by droplet collision of H_2O_2 and $NaBH_4$ at We = 31 and $\Delta = 1.3$.

After several oscillation periods, the two droplets merged and the opaque product inside the droplet start to emerge as depicted in Stage II for the benchmark. Nevertheless, distinction still exists that, for collision with larger Δ, as shown in Fig. 5.4, the occupation area of the opaque product inside the merged droplet is smaller than that in benchmark, which is in turn smaller than that in case $We = 61$ in which the dark area covers up the entire droplet area as shown at 29.0ms in Fig. 5.5. The reason is obvious that in the present study only fuel rich cases are considered, so the larger Δ means that there is more excess fuel needs to be heated up. As already been verified that the equivalence ratio is a function of cubic of droplet size ratio, therefore, although enhance the diversity of size might increase the mixing between droplets through the internal mixing, the simultaneously

induced fuel rich effect on the reaction will be so more severe that the ignition will be prolonged when the size ratio is enlarged, as the comparison of 59.8ms and 35.8ms in case of $\Delta = 2.3$ and 1.3 repectively.

5.5 Dependence of IDT on We and Δ

By employing the grayscale level analysis depicted in Chapter 1, the ignition delay time (IDT) in the present study also could be identified by tracking the luminous flame kernel. The dependence of IDT on We, varying from 25 to 100, and Δ, from 1.1 to 2.2, is studied and corresponding results are shown in Fig. 5.6(a) and Fig. 5.6(b).

It is notable that the IDT becomes shorter with increasing We, such as 1.55, 1.75 and 2.05, as shown in Fig.5.5(a). It is because of the enhancement of mixing in large impacting kinetic energy as explained above. An interesting phenomenon is that the IDT along with We is decreasing monotonically herein, quite unlike that by WFNA and TMEDA droplets as shown in Chapter 2. The underlying reason is that the viscosity of ethanolamine is much larger than that of both TMEDA and WFNA. The large level of viscosity dissipation will diminish internal mixing between the droplets to suppress the occurrence of the so called ‘jet-like’ mixing, which was regarded as the main mechanism

to cause the non-monotonic dependence of IDT on We in TMEDA/WFNA droplet collision.

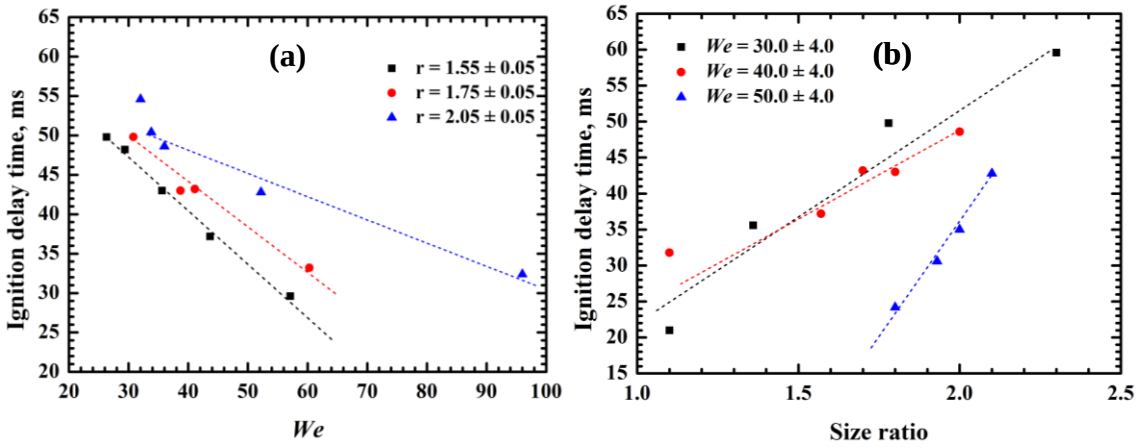

Figure 5.6 Dependence of IDT on (a) We with $\Delta = 1.5, 1.75\ and\ 2.1$, and (b) Δ with $We = 31, 41\ and\ 61$.

The dependence of IDT on Δ is shown in Fig.5.6(b) at three different We of 30, 40 and 50 respectively. It is noted that the IDT will be prolonged when Δ is getting larger. The underlying mechanism has already been explained that the fuel rich effect will increase cubically when Δ increases. Reaction is then weakened dramatically since a poor reaction condition and also an extra amount of fuel to be heated.

6. Dynamics of binary collision of shear thinning non-Newtonian droplets

6.1 Introduction

Collisions of liquid droplets in gaseous environments are of relevance to many natural and industrial processes comprising dispersed gas-liquid two-phase flows, such as raindrop formation in clouds, atmospheric aerosol circulation, ink-jet printing, spray combustion, and various spraying processes used in metallurgical, chemical and pharmaceutical engineering.

A large number of studies on the collision of binary droplets of Newtonian liquids have been reported and summarized in a few excellent reviews. The majority of these studies was focused on identifying and interpreting various outcomes of droplet collision, i.g. coalescence, bouncing and separation, because they strongly influence the number density, velocity and size distributions of droplets, and in turn affect the efficiency of a concerned process.

Motivated by the need to understand dense spray of liquid fuels in engines, Law and coworkers systematically studied hydrocarbon (such as heptane, decane, dodecane, tetradecane and hexadecane) droplet collisions in various gaseous environments (nitrogen, helium and ethylene) under reduced and elevated pressures in the range of 0.6~12 atm. A unified description of the collision outcomes in *We-B* parameter space was proposed for

water and hydrocarbons and subsequently confirmed for ethanol: (I) coalescence after a minor deformation, (II) bouncing, (III) coalescence after substantial deformation, (IV) coalescence followed by separation for near head-on collision, (V) coalescence followed by separation for off-center collision. Furthermore, the boundaries between the collision regimes can be significantly affected by the fluid properties of the ambient gas and the droplets[8]. For example, increasing gas pressure promotes bouncing while increasing surface tension promotes coalescence. Consequently, bouncing can be observed for water droplets at higher pressures although it is absent at atmospheric pressure. Similarly, while bouncing was observed for alkane droplets at atmospheric pressure, it was absent at lower pressures[8].

In recent years, collision dynamics of binary droplets of non-Newtonian fluids in gaseous environment has gained increasing interest[36, 80, 81]. Its practical relevance includes, for example, the prediction of properties of particulate products formed in spray processes of polymeric solutions for chemical, pharmaceutical or medical applications, and the facilitation of liquid-phase reaction in propulsion systems utilizing gelled hypergolic propellants (GHP) [14-16]. Because of the reduced vapor pressure of propellants by gelling, the ignition of GHPs can be only triggered in liquid phase after a succession of fluid-

dynamical processes: the collision, the coalescence and the mixing of the fuel and oxidizer droplets.

Whereas there has been recognized that many liquids of practical and industrial interest do not conform to the simple Newtonian fluid behavior [82], it is surprising to find that investigations on droplet collision of non-Newtonian liquids are severely scarce in the literature. To the knowledge of the author, the only existing experimental results were published by Motzigemba et al. [83] for the collision of droplets of 2.8wt% aqueous solution of carboxymethylcellulose for We = 766, 1980 and 2625. The solution exhibits shear-thinning (or pseduoplastic) behavior that the apparent viscosity (shear stress divided by shear rate) decreases with increasing shear rate.

Regardless of these worthy, albeit scattered advances, our understanding of collision dynamics of non-Newtonian droplets in gaseous environment is far from being satisfactory and this field of research is "still at its beginning". Consequently, the present study will be focused on the collision of binary droplets of shear-thinning fluids in atmospheric air based on the following considerations. First, the simplest and also the commonest type of non-Newtonian fluids is shear-thinning and almost all non-Newtonian fluids display shear-thinning behavior under appropriate circumstances. Many experimental data and mathematical models from the literature for the rheology of shear-

thinning fluids can be used to validate the results to be obtained in the proposed study. Second, the ambient gas and its pressure have been found in the previous studies to strongly influence the collision outcomes of Newtonian droplets and seem very likely to have the same influence on shear-thinning droplets. However, only the standard atmospheric air will be considered in the proposed problem to avoid the added complication of different gaseous environments, which nevertheless merit future studies.

6.2 Experimental Setup and specification

Practically, the experimental difficulty of the proposed study is to generate spatially and temporally stable droplets of shear-thinning fluids which have very large zero-shear-rate viscosity. This may also be the reason for lack of experimental results on non-Newtonian liquid droplet collisions. Many previous experiments on Newtonian droplets adopted the ink-jet printing technique, in which a liquid jet is produced from a nozzle connected to a pressured liquid reservoir and regular disturbances are generated by using piezoelectric pulses to break up the liquid jet into droplets. Our preliminary investigation shows that there is an increasing difficulty of generating stable droplets with enhanced non-Newtonian behavior. For example, an intensely elongated liquid column of 0.25wt% aqueous solution of Carbomer was formed without being broken into droplets by using the

ink-jet printing technique. As such, in the present study, we still adopted the micro electromagnetic valve as employed in the previous hypergolic ignition experiments to generate the non-Newtonian droplets.

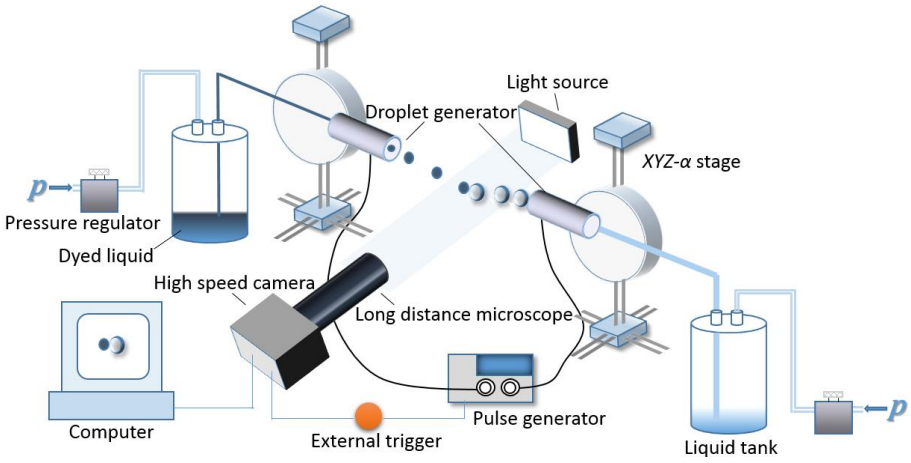

Figure 6.1. Schematic of the experimental apparatus for binary collision of non-Newtonian droplets.

Since the goal of present experiment is to achieving the binary collision of non-Newtonian shear thinning droplets and investigating the non-Newtonian effect on the droplet collisions, we have chosen the aqueous solution of Carbomer, of which the constitutive relation could be directly changed by simply altering the amount of Carbomer dissolved into the water, as the testing non-Newtonian fluid. The experimental setup is as that used in the previous experiments, as depicted in Chapter 2, but just replace the nozzle for generating WFNA droplet by another micro valve generating the TMEDA droplet. The schematic of the experimental apparatus is as shown in Fig. 6.1. Nevertheless, since the liquid employed in the present experiment is quite different with that of the hypergolic

propellants and the focus now turns to be the behavior of the two colliding droplets with no chemical reactions, the operational details and measurement setup is of certain difference from that in the previous experiments.

Particularly, as the viscosity of the static non-Newtonian fluid is quite large, the dispensing pressure was promoted to about 100 kPa, much higher than that employed in WFNA/TMEDA experiments(10~20kpa). Attentions therefore must be paid that instability caused by the pressure fluctuation when switch on/off the micro-valve should be avoid. In addition, since the whole collision process herein may happen in a much shorter period and a smaller space, another set of high speed camera from Photron Co. integrated with one set of long distance microscope was applied in the present experiment. The recording speed herein is 20000 fps with exposure time of 2 μs under the amplification factor of 4~7.

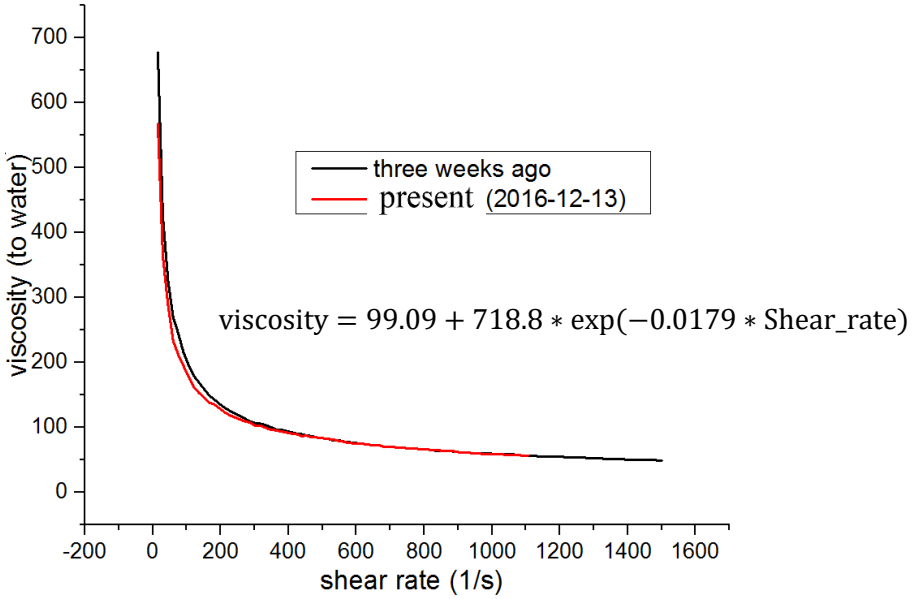

Figure 6.2 Rheology of the testing sample of aqueous solution of Carbomer with 0.5 wt%.

A BROOKFIELD RST rotational rheometer system (shear stress: $0.1\sim2.1\times10^5$ Pa, shear rate: $0\sim5.1\times10^4$ s^{-1}) and a KRŰSS K20 digital tensiometer system were used to quantify the rheology and surface tension of the concerned shear-thinning fluids respectively. The aqueous solution adopted in the present study contains 0.5 wt% Carbomer U20, and the sample had been standing for almost one month before being used to ensure the absence of sediment. The specific rheological characteristic is shown in Fig. 6.2, form which one can see that the viscosity decreases continuously with the shear rate, charactering the typical property of shear thinning liquid and this rheology can retain for a sufficiently long time. Moreover, because the solutions can exhibit apparent deviation from the simple Power-law behavior, the so called upper and lower Newtonian regions or even a yield stress will emerge. The relative density and surface tension of the sample compared to those of pure water are 0.825 and 0.7 respectively.

6.3 non-Newtonian effect on droplet collision in various We

The features of droplet collision of shear thinning fluid would be quite different and complicated compared with that of Newtonian fluids, because the viscosity affecting significantly in parameters such as We and Oh now is no longer constant but a function of the shear rate that is temporally related to the local velocity field within the interacting

droplets. Therefore, to better investigate the mechanism during the droplet collision process, a measurement of the velocity field within the droplet is favored. However, it will with no doubt gain more difficulties to the experiment. By applying the limited experimental facilities, the author still tried to figure out some physical characters of collision process that may be explicitly or implicitly explained by the non-Newtonian effect.

To avoid pushing the problem too intricate, only equal (or near equal) size droplet collisions were considered in the present experiments. Two main goals herein are to study the collision outcomes and features of head-on collision of the non-Newtonian droplets and to study the droplet collision under various impact parameters.

In order to enable the shear thinning character well emerged, a large We rang was considered and achieved from $O(1)$ to $O(100)$. Figure 6.3 shows the head-on collision of the shear thinning droplets at various Wes of 4, 50, 290 and 500.

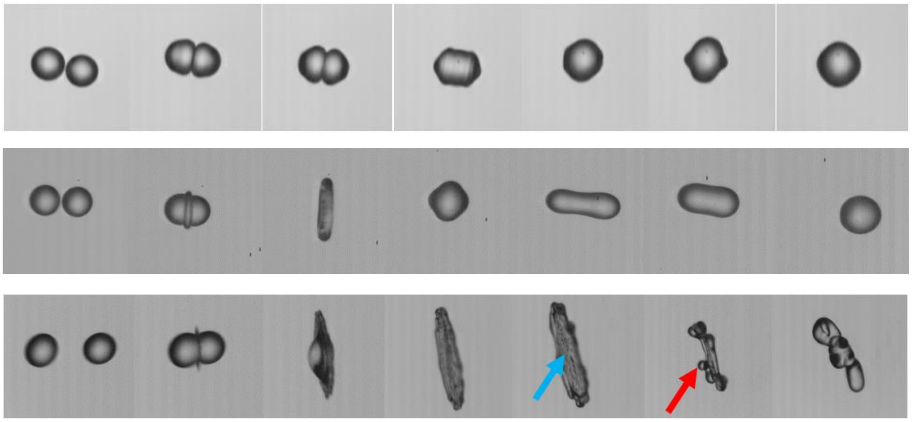

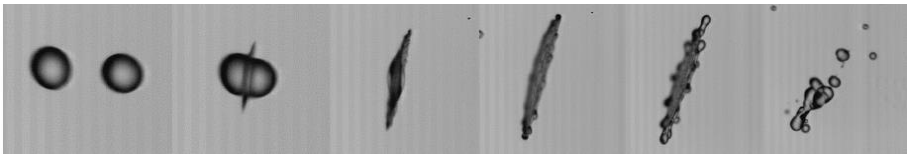

Figure 6.3 Shear thinning droplet collision process at (a) $We = 4$, (b) $We = 50$, (c) (a) $We = 290$ and (a) $We = 500$.

With the comparison from Fig. 6.3a and Fig. 6.3b, the features for non-Newtonian droplet collision at small or moderate We such as 4 and 50 are similar with the configurations of droplets in pure water. Actually, the deformation of the non-Newtonian droplets during collision is a little weaker than that of pure water because of the large level of viscosity dissipation. Furthermore, it seems that the non-Newtonian character does not emerge under such level of impacting kinetic energy.

Nevertheless, if the We goes as large as, say 290, as shown in Fig. 6.3c, in which the camera was slide about 5 degrees deviating to the perpendicular plane where the collision happens, distinguish features exhibits. Specifically, after impacting with each other, a thin liquid film is observed as indicated by the blue arrow on the image. The liquid film in non-Newtonian fluid is much more unsmooth than that emerging in collision of pure water. This is because of the uneven shear rates distributed on the surface. Moreover, in additional to the liquid film, the edge area also was exposed under the unbalanced surface tension force and therefore, some liquid globules are formed and unevenly distributed along the edge as indicated by the red arrows. Owing to the large viscosity under small

shear rate at the edge area, these liquid globules did not separate from each other but merged back instead forming an extremely irregular shape of liquid mass eventually. In addition, when the We goes further up to 500, the distributed liquid globules at the edge area can not be held together any longer so that some of them separate forming several satellite droplets, as shown in Fig. 6.3d.

Throughout the present experiments, reflective separation was not observed, which however would occur at $We = 19$ for collisions of pure water. It can be explained by Qian [8], that the transition We between the coalescence and reflective separation should be proportional to the Ohnesorge number. Since the average viscosity of the sample liquid is much larger than that of pure water, the reflective separation must be suppressed.

6.4 non-Newtonian effect on droplet collision in various Δ

In order to study the performance of droplet collision of shear thinning fluid at various impact parameter, Bs, a large number of experiments were conducted with B varying from 0 to 0.9 under three Wes of 4, 19 and 33.

A variety of outcomes exhibit under such collision dynamic conditions. For example, the two droplets may bounce away without any mass transformation after they impact onto each other; or they merge into one droplet after several oscillation periods; or

they stretch away after interacting with moderate mass transformation as depicted in Chapter 2. The outcome regime nomogram in $We - B$ parameter space is shown in Fig. 6.4 with several representative collisions (a)~(h) to help illustrate the corresponding interaction mode shown in Fig.6.5.

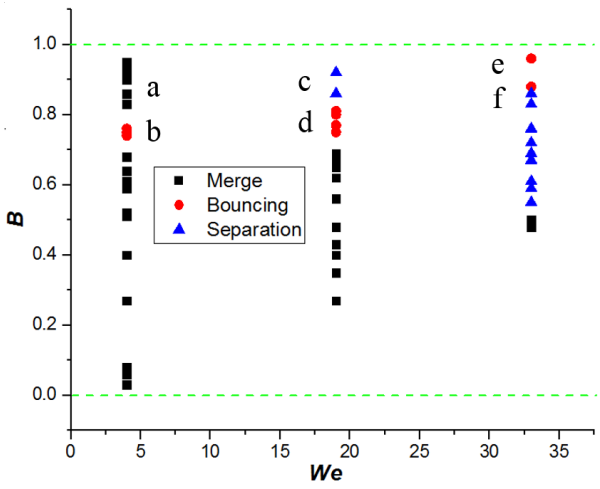

Figure 6.4, Outcome regimes of merge, bouncing, separation at the various Wes of 4, 19 and 33 respectively.

6.4.1 Ribbon-shape regime of bouncing at large level of B

The two interacting droplets favor to merge into one droplet at moderate B in all three Wes. However, interaction mode within the coalescence with B other than 0 is distinct with that for $B = 0$. Comparison can be made with the collision (g) and the collisions in Fig. 6.5a, in which $We = 4.0$ but $B = 0.35$ and $B = 0$ respectively. As shown on these images, the off-center collision (g) exhibits a centrally symmetric

configuration of the merged droplet, while an axial symmetric feature could be observed in the head-on

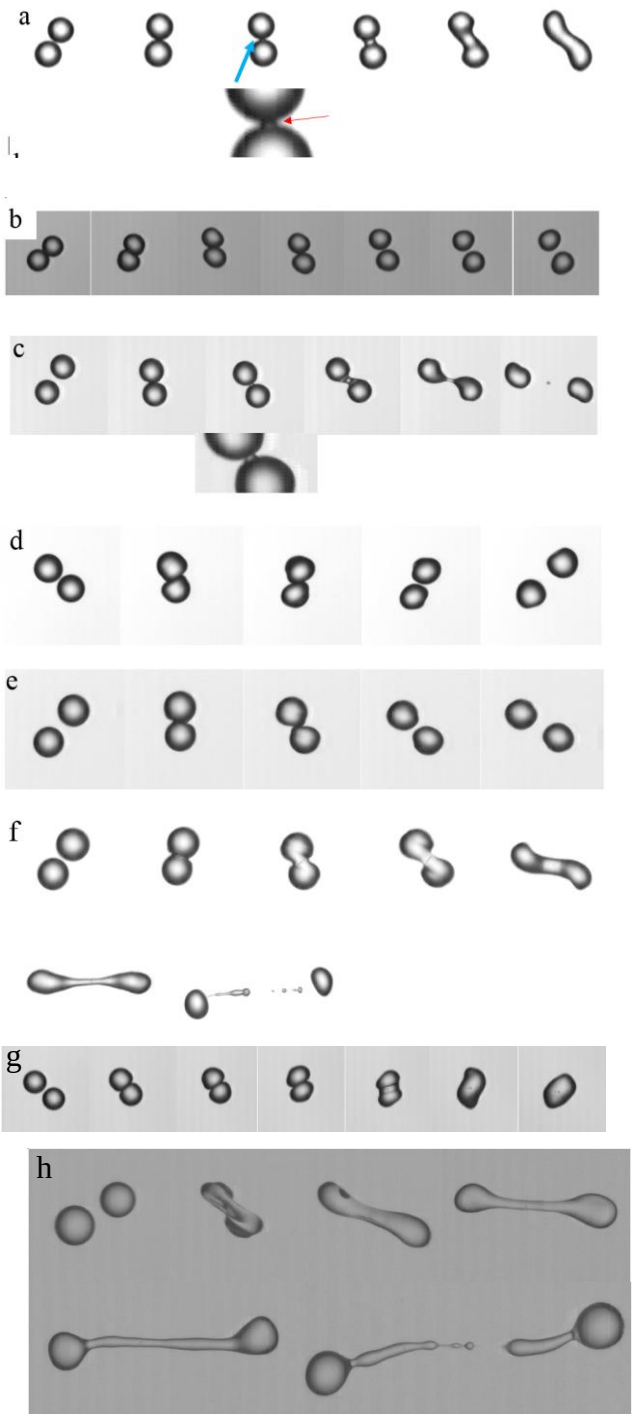

Figure 6.5 Collisions (a)~(h) corresponds to those indicated on Fig. 6.4.

collision. As already been illustrated in Chapter 2, this is because that for off-center collision, there should be reflective and stretching effect that are affecting the collision, while merely reflective effect exists in the head-on collision.

If B enlarges to high level, say 0.8, bouncing outcome could be observed, as shown in collision (b), which is similar with the collision of pure water droplets. However, an interesting phenomenon is that the coalescence outcome will re-appear following the bouncing events when B continues increasing to extremely large level, say 0.9, as shown in collision (a). As shown on the images, at the beginning of the contact of the two colliding droplets, almost no deformation exhibits due to the little portion of directly interacting mass. A tiny liquid ligament , as indicated by the red arrow, has however still been formed under the surface tension force during the deformation. More liquid drain from both droplets parts to strengthen the liquid ligament as shown in the subsequent image. The two spherical droplets finally deform out of shape and eventually merge into one larger droplet. It is obvious that the formation of the tiny liquid ligament is the key of the merging event. In fact, owing to the high viscosity dissipation under diminutive shear stress, the two droplets during the collision deform negligibly, which in turn benefits the merging in two ways. First, as there is little deformation, the interface area will diminish substantially to minimize the repelling force from the air between the two droplets when they are

approaching to each other. Second, the insignificant deformation of the droplet will also drain the air easily during the approaching period which in turn make the gap between the two droplets easily to reach the level the coalescence event requires.

6.4.2 Stretching separation at medium level of B

For collisions at $We = 19$, instead of merging, stretching separation now occurs following the bouncing events at extremely large B. One such representative case is shown in collision (c). With the help of the amplified figure, it is easy to find that the thin liquid ligament, as that in collision (a), is still formed. Nevertheless, the tiny liquid ligament, instead of becoming stronger as it does in collision (a), is stretched by the two droplets because of the large amount of stretching kinetic energy. The liquid ligament now becomes thinner and eventually breaks into smaller satellite drops. If the Weber number continues enlarging to, say 33.0, the liquid ligament cannot be observed any more. As shown in collision (e), the two collided droplets exhibit considerable deformation even when B is larger than 0.9 and bounce away from each other without any mass transfer. At such We, the stretching separation is favored at a large range of B as shown on the outcome regime nomogram, in which collision (f) and (h) are the presentative cases. An interesting phenomenon exhibiting in collision (h) when compared with the off-center collision of

Newtonian droplets shown in Fig.5 is that instead of being pinched off at both edges sides, the separation for collision of non-Newtonian droplets happens at the central area of the liquid ligament as shown at 1.2ms in collision (h). The underlying reason is that when the two interacting droplet masses stretch with each other, a ligament will be formed with different shear rates at different positions. Specifically, the central area of the ligament should be encountering stronger shear effect than it is at the edge areas that are connecting the bulk drop mass. Therefore, the edge part of liquid ligament is more likely to stick onto the bulk drop mass, acting as a solid-like feature, as shown in the red circle area in collision (h). While the central part is more vulnerable to be broken up if they are imposed by torque force.

6.5 Outcome regimes in $We - \Delta$ parameter space

More experiments have also been conducted to study the outcome regime in $We - \Delta$ parameter space, in which We varying from $O(1)$ to $O(100)$, and $\Delta = 0 \sim 0.9$. As shown in Fig. 6.6 and Fig. 6.7, generally for head-on collisions, no reflective separation is observed even when the Weber number goes as large as the value of several hundreds. Irregular interaction mode in fact exhibits at the We larger than 200 because of the instability that is caused by the large level of kinetic energy at the edge area of the complex

droplet mass. If Weber number goes larger, the complex droplet would scatter into some satellite droplets.

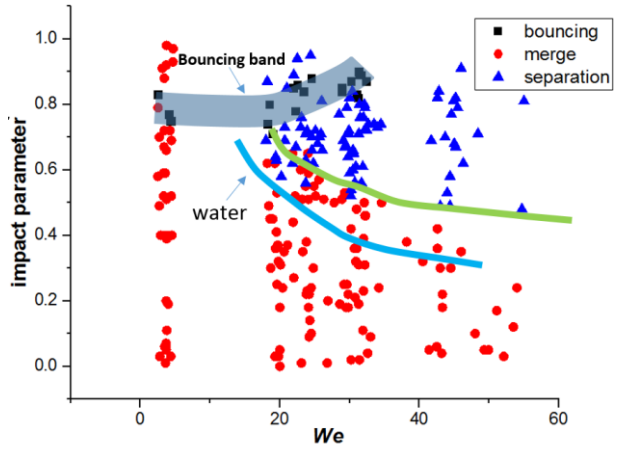

Figure 6.6, Outcome regimes of shear thinning droplet collisions at the medium We in $We - \Delta$ parameter space.

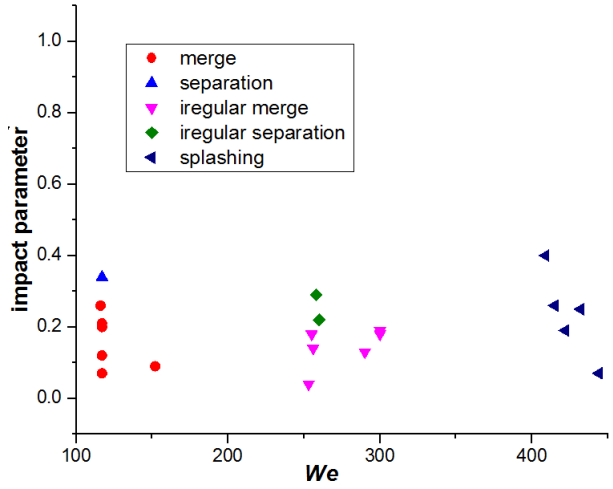

Figure 6.7, Outcome regimes of shear thinning droplet collisions at the large We in $We - \Delta$ parameter space.

For the off-center collisions, compared with data of pure water (blue regime line), it is found that the stretching separation regime line for this non-Newtonian fluid material (in green color) locates at higher *B*. This is because that the separation of the non-

Newtonian droplets is suppressed by the large level of viscosity dissipation. Another interesting phenomenon is that at large impact parameters there is a bouncing strap area in which the two droplets will merely bounce away after collision at the range of $We = 4 \sim 30$, as indicated by the gray strip in Fig. 6.6. The reason of this special bouncing regime has already been illustrated in preceding sections.

7. Concluding remarks

Hypergolic ignition induced by droplet collisions of propellants of WFNA/TMEDA and H_2O_2/ethanolamine solution of $NaBH_4$, and the dynamics of droplet collision of the shearing thinning gelling agent liquid have been experimentally studied in the present thesis. Due to the strong corrosivity of fuming nitric acid and high viscosity of the shear thinning Carbomer solution, two special types of droplet generators were employed and integrated into a newly designed experimental apparatus equipped with a precise pressure regulating system. A grayscale level analysis method based the grayscale of pixels on the shadowgraphs of the collision process was developed to calculate the collision parameters such as droplet size, relative speed and so forth. It has also been used to depict the ignition process and define an ignition delay time based on development of the dark vapor and the luminous flame kernel in high accuracy.

For propellants of WFNA/TMEDA, the hypergolic ignition by droplet collision has been systematically studied in viewpoint of collision dynamics and the heat and mass transfers. Collison We, Δ and B are mainly considered, in the present study, as collision controlling parameters. Droplet size effect is also studied and considered to be influencing the heating, vaporization of the droplets. All the factors above are proved to play essential roles in the hypergolic ignition process.

Particularly, we first studied the hypergolic ignition by head-on collision of TMEDA and WFNA droplets, as presented in Chapter 1. In this part of work, a detailed description of the ignition process has been given in order of five stages defined based on the phenomena exhibiting during the ignition period.

With a precise definition of ignition delay time, the We effects on the hypergolic ignition was well studied. A monotonic dependence of IDT on We has been identified and explained that it is because of the non-monotonic occurrence of jet-like internal mixing pattern along with the growth of We within the collision of unequal size droplets, as reported by Tang [48]. When the We goes so large that splashing happens, it was found the IDT now will be independent with We, because the droplets have already been well mixed immediately after impacting and the chemical reaction should take place of the physical mixing effect to the ignition process. Second, the droplet size ratio was discovered

to affect the ignition in two aspects. On the one hand, the interaction and mixing pattern will be altered by changing Δ; on the other hand, distinct Δ means different equivalence ratios.

The off-center collision of TMEDA and WFNA droplets has also been studied with the focus on its effect on the hypergolic ignition. By analyzing the experimental data employing the grayscale level analysis method and together with the numerical simulation in VOF method, it is found that the off-center collision would affect the ignition in two contradictory ways. Specifically, in other words, the effects of impact parameter on hypergolic ignition can be understood as the competence between stretching and reflexive impact inertia. The stretching effect promotes the internal mixing and shorten the IDT for nearly head-on droplet collision, while it turns to suppress the interaction of mass and internal mixing at large B when stretching separation happens.

Droplet size effects on the hypergolic ignition was also experimentally studied and theoretically analyzed through multiple time scaling analysis. The hypergolic ignitability of the system is characterized by a regime nomogram in the $We - d_O$ parameter space, indicating that decreasing the droplet size (d_O) seems to suppress the ignition so that a larger We or a smaller Δ or both together is favored for ignition. However, the experimentally observed ignition delay time at fixed We and Δ decreases with the droplet

size, seemingly implying an opposite size-effect on the ignition. These contradict mechanisms could be explained that droplet heating is quadratically shortened by reducing the droplet size, consequently causing a shorter ignition delay; while droplet vaporization with heat loss is prolonged by reducing the droplet size though a scaling of $d_O^{-5/4}$ if d_O is not too small to cause non-ignition by the substantially increased heat lost.

As one candidate of the green propulsion propellants, hypergolic ignition by the droplet collision of hydrogen peroxide and ethanolamine solution of sodium borohydride has also been experimentally studied. This pair of hypergolic fuel and oxidizer has its significant potential for the practical usage. Moreover, they are also a proper option for studying the interactions of the fuel and oxidizer droplets during the pre-ignition period because of the suppressed generation of opaque vapor. It has been found that the five stages defined in the collision of TMEDA/WFNA droplets are still applicative herein. Opaque products will first be generated and accumulated inside the merged droplet. Then, as the expansion of these products, the surface of the droplet will breakup leading to the ignition event. IDT for this pair of propellant droplets was found to monotonically decrease with *We*, because of the large *Oh* number. Size ratio now affect mainly through the change of equivalence ratio between the fuel and oxidizer.

The droplet collision of the gelled shear thinning droplets were also studied. Since the non-Newtonian effect will gain the complication of the collision process, and the interaction mode between the droplets in such kind of liquid is quite unknown to the date, the present thesis only focus on the non-reactive binary collisions of gelled droplets by Carbomer U20. It was found that when the collision We ranges among moderate values, the shear thinning effect might be overwhelmed by the viscosity effect, and if We goes as large as when splashing happens, the non-Newtonian effect could exhibit apparently. If the impact parameter, *B*, goes larger, interesting phenomenon could be observed that one strap-shape bouncing regime exhibits in the outcome nomogram in $We - \Delta$ parameter space. Besides, owing to the shear thinning effect, the characteristics of stretching separation is quite different from that in the Newtonian droplet collisions.

In future, the hypergolic ignition induced by the collision of the gelled fuel and oxidizer droplets, which is more approaching to the practical situations, merits more effects. In addition, more options of 'green' hypergolic propellants should be explored and tested corresponding to the requirement of the concept of reusing rocket launching systems. Furthermore, the work of mixing between the fuel and oxidizer in terms of more realistic ways, such as spray and jet impinging, also draw attentions.

Reference

[1] R.J.M. Eric A. Hurlbert, Propellant Ignition and Flame Propagation, in: V. Yang, M. Habiballah, J. Hulka, M. Popp (Eds.), Liquid Rocket Thrust Chambers: Aspects of Modeling, Analysis, and Design, American Institute of Aeronautics and Astronautics, Inc., Virginia, 2004.

[2] S.M. Davis, N. Yilmaz, Advances in Hypergolic Propellants: Ignition, Hydrazine, and Hydrogen Peroxide Research, Adv. Aerosp. Eng. 2014 (2014) 1-9.

[3] E.A. Fletcher, G. Morrell, Ignition in liquid propellant rocket engines, in: M.G. J. Ducerme, A. H. Lefebvre (Ed.), Prog. Combust. Sci. Tech. Volume I, Pergamon, Oxford. London. New York. Paris, 1960, pp. 183-215.

[4] G.P. Sutton, O. Biblarz, Rocket propulsion elements, 8 ed., John Wiley & Sons, Hoboken, New Jersey, 2010.

[5] F.A. Williams, Combustion Theory , Cummings Publ. Co, (1985).

[6] Y.J. Jiang, A. Umemura, C.K. Law, An Experimental Investigation on the Collision Behavior of Hydrocarbon Droplets, J Fluid Mech 234 (1992) 171-190.

[7] N. Ashgriz, J. Poo, Coalescence and separation in binary collisions of liquid drops, J Fluid Mech 221 (1990) 183-204.

[8] J. Qian, C.K. Law, Regimes of coalescence and separation in droplet collision, J Fluid Mech 331 (1997) 59-80.

[9] T. Suzuki, J.-y. Kohno, Simultaneous Detection of Images and Raman Spectra of Colliding Droplets: Composition Analysis of Protrusions Emerging during Collisions of Ethanol and Water Droplets, J. Phys. Chem. B 118 (2014) 5781-5786.

[10] J.-y. Kohno, M. Kobayashi, T. Suzuki, Protrusion formation during the collisional process of ethanol and water droplets: Capillary wave propagation on the water droplet, Chem. Phys. Lett. 578 (2013) 15-20.

[11] Y. Takano, S. Kikkawa, T. Suzuki, J.-y. Kohno, Coloring Rate of Phenolphthalein by Reaction with Alkaline Solution Observed by Liquid-Droplet Collision, J. Phys. Chem. B 119 (2015) 7062-7067.

[12] R. Schliebs, Hydrazine and its Derivatives. Preparation, Properties, Applications. Von EW Schmidt. Wiley, Chichester Angewandte Chemie 97 (1985) 360-360.

[13] G.P. Sutton, History of liquid propellant rocket engines, AIAA, 2006.

[14] F.A. Williams, Simplified theory for ignition times of hypergolic gelled propellants, J Propul Power 25 (2009) 1354-1357.

[15] K.Y. Cho, T.L. Pourpoint, S.F. Son, R.P. Lucht, Microexplosion Investigation of Monomethylhydrazine Gelled Droplet with OH Planar Laser-Induced Fluorescence, J Propul Power 29 (2013) 1303-1310.

[16] J.D. Dennis, T.D. Kubal, O. Campanella, S.F. Son, T.L. Pourpoint, Rheological Characterization of Monomethylhydrazine Gels, J Propul Power 29 (2013) 313-320.

[17] G.d. Silva, Hypergolic systems: a review in patents, J. Aerospace Technol. Management 4 (2012) 407-412.

[18] L.A. Paquette, D. Crich, P. Fuchs, G. Molander, A.R. Van Dyke, T. Jamison, Encyclopedia of reagents for organic synthesis, Van Dyke, AR; Jamison, TF, 2009.

[19] R. Simberg, Elon Musk on SpaceX's Reusable Rocket Plan, Popular Mechanics, (2012).

[20] P.B. De Selding, SpaceX cuts flight-to-reflight time for Falcon 9 fisrt stage, Space Intel Report, (2017).

[21] A.S. Gohardani, J. Stanojev, A. Demairé, K. Anflo, M. Persson, N. Wingborg, C. Nilsson, Green space propulsion: Opportunities and prospects, Progr. Aerosp. Sci. 71 (2014) 128-149.

[22] P. Mark Ventura, E. Wernimont, S. Heister, P. Steve Yuan, Rocket grade hydrogen peroxide (RGHP) for use in propulsion and power devices-historical discussion of hazards, (2007).

[23] C.D. McKinney Jr, M. Kilpatrick, An Apparatus for Measuring the Rates of Some Rapid Reactions, Rev. Sci. Instrum. 22 (1951) 590-597.

[24] M. Kilpatrick, L.L. Baker. A study of fast reactions in fuel-oxidant systems: Anhydrous hydrazine with 100 per cent nitric acid. Symp. (Int.) Combust, (1955)196-205.

[25] R.L. Schalla, E.A. Pletcher. The Behavior of The System Triethylamine—White Fuming Nitric Acid Under Conditions of Rapid Mixing, Symp. (Int.) Combust, (1957) 911-917.

[26] R.L. Schalla, The Ignition Behavior of Various Amines with White Fuming Nitric Acid, ARS Journal 29 (1959) 33-39.

[27] J.D. Dennis, S.F. Son, T.L. Pourpoint. Critical Ignition Criteria for Monomethylhydrazine and Red Fuming Nitric Acid in an Impinging Jet Apparatus, 48th AIAA/ASME/SAE/ASEE Joint Propulsion Conference & Exhibit, (2012) 4325.

[28] S. Wang, S.T. Thynell, A. Chowdhury, Experimental study on hypergolic interaction between N, N, N′, N′-tetramethylethylenediamine and nitric acid, Energy & Fuels 24 (2010) 5320-5330.

[29] J.D. Dennis, T.L. Pourpoint, S.F. Son, Ignition of Gelled Monomethylhydrazine and Red Fuming Nitric Acid in an Impinging Jet Apparatus, 47th AIAA/ASME/SAE/ASEE Joint Propulsion Conference & Exhibit, Joint Propulsion Conferences, California, 2011.

[30] J. Forness, T.L. Pourpoint, S.D. Heister, Experimental Study of Impingement and Reaction of Hypergolic Droplets, 49th AIAA/ASME/SAE/ASEE Joint PropulsionConference, 2013, pp. 3772.

[31] E.M. Dambach, Y. Solomon, S.D. Heister, T.L. Pourpoint, Investigation into the Hypergolic Ignition Process Initiated by Low Weber Number Collisions, J Propul Power 29 (2013) 331-338.

[32] E. Dambach, K. Cho, T.L. Pourpoint, S.D. Heister, Ignition of advanced hypergolic propellants, AIAA Paper, (2010).

[33] E.M. Dambach, B.A. Rankin, T.L. Pourpoint, S.D. Heister, Temperature estimations in the near-flame field resulting from hypergolic ignition using thin filament pyrometry, Combust. Sci. Technol. 184 (2012) 205-223.

[34] T. Kubal, R. Arnold, T. Pourpoint, O. Campanella, W. Anderson. Rheological Characterization of Hydroxypropylcellulose/Monomethylhydrazine and Silica/Red Fuming Nitric Acid Gels, 46th AIAA/ASME Joint Propulsion Conference. 2010.

[35] K.-L. Pan, P.-C. Chou, Y.-J. Tseng, Binary droplet collision at high Weber number, Phys. Rev. E 80 (2009) 036301.

[36] N. Ashgriz, Handbook of atomization and sprays: theory and applications, Springer Science & Business Media, 2011.

[37] C. Tang, P. Zhang, C.K. Law, Bouncing, coalescence, and separation in head-on collision of unequal-size droplets, Phys Fluids 24 (2012).

[38] C. Gotaas, P. Havelka, H.A. Jakobsen, H.F. Svendsen, M. Hase, N. Roth, B. Weigand, Effect of viscosity on droplet-droplet collision outcome: Experimental study and numerical comparison, Phys. Fluids 19 (2007) 102106.

[39] Y. Pan, K. Suga, Numerical simulation of binary liquid droplet collision, Phys Fluids 17 (2005) 082105.

[40] M. Orme, Experiments on droplet collisions, bounce, coalescence and disruption, Prog. Energy Combust. Sci., 23 (1997) 65-79.

[41] P. Zhang, C.K. Law, An analysis of head-on droplet collision with large deformation in gaseous medium, Phys Fluids 23 (2011) 042102.

[42] C. Rabe, J. Malet, F. Feuillebois, Experimental investigation of water droplet binary collisions and description of outcomes with a symmetric Weber number, Phys Fluids 22 (2010).

[43] K. Willis, M. Orme, Binary droplet collisions in a vacuum environment: an experimental investigation of the role of viscosity, Exp Fluids 34 (2003) 28-41.

[44] M. Dai, D.P. Schmidt, Numerical simulation of head-on droplet collision: Effect of viscosity on maximum deformation, Phys Fluids. 17 (2005) 041701.

[45] K. Sun, P. Zhang, C.K. Law, T. Wang, Collision Dynamics and Internal Mixing of Droplets of Non-Newtonian Liquids, Phys. Rev. Appl. 4 (2015) 054013.

[46] D. Liu, P. Zhang, C.K. Law, Y. Guo, Collision dynamics and mixing of unequal-size droplets, Int. J. Heat Mass Transfer 57 (2013) 421-428.

[47] F. Blanchette, T.P. Bigioni, Dynamics of drop coalescence at fluid interfaces, J Fluid Mech 620 (2009) 333-352.

[48] C. Tang, J. Zhao, P. Zhang, C.K. Law, Dynamics of Internal Jets in the Merging of Two Droplets of Unequal Sizes, J Fluid Mech 795 (2016) 671-689.

[49] C.K. Law, Fuel options for next-generation chemical propulsion, AIAA, 50 (2012) 19-36.

[50] K. Sun, T. Wang, P. Zhang, C.K. Law, Non-Newtonian flow effects on the coalescence and mixing of initially stationary droplets of shear-thinning fluids, Physical Review E 91 (2015) 023009.

[51] A. Anilkumar, C. Lee, T. Wang, Surface‐tension‐induced mixing following coalescence of initially stationary drops, Phys Fluids 3 (1991) 2587-2591.

[52] M.J. McQuaid, W.H. Stevenson, D.M. Thompson, Computationally Based Design and Screening of Hypergolic Multiamines, DTIC Document, 2004.

[53] M. McQuaid, Notional Hydrazine-Alternative Hypergols: Design Considerations, Computationally-Based Property Determinations, and Acquisition Possibilities, US Army Research Laboratory, (2006).

[54] W.-G. Liu, S. Dasgupta, S.V. Zybin, W.A. Goddard III, First Principles Study of the Ignition Mechanism for Hypergolic Bipropellants: N, N, N′, N′-Tetramethylethylenediamine (TMEDA) and N, N, N′, N′-Tetramethylmethylenediamine (TMMDA) with Nitric Acid, J. Phys. Chem. A 115 (2011) 5221-5229.

[55] P. Zhang, L.D. Zhang, C.K. Law, Density functional theory study of the reactions of 2-azido-N,N-dimethylethanamine with nitric acid and nitrogen dioxide, Combust Flame 162 (2015) 237-248.

[56] S. Wang, S. Thynell, An experimental study on the hypergolic interaction between monomethylhydrazine and nitric acid, Combust Flame 159 (2012) 438-447.

[57] J.F. Driscoll, C.C. Rasmussen, Correlation and analysis of blowout limits of flames in high-speed airflows, J Propul Power 21 (2005) 1035-1044.

[58] W.M. Pitts, The global equivalence ratio concept and the formation mechanisms of carbon monoxide in enclosure fires, Prog. Energy Combust. Sci. 21 (1995) 197-237.

[59] C. Focke, D. Bothe, Computational analysis of binary collisions of shear-thinning droplets, J Non-Newton Fluid 166 (2011) 799-810.

[60] F. Blanchette, Simulation of mixing within drops due to surface tension variations, Phys Rev Lett 105 (2010) 074501.

[61] K.-L. Pan, Y.-H. Tseng, J.-C. Chen, K.-L. Huang, C.-H. Wang, M.-C. Lai, Controlling droplet bouncing and coalescence with surfactant, J Fluid Mech 799 (2016) 603-636.

[62] T. Inamuro, S. Tajima, F. Ogino, Lattice Boltzmann simulation of droplet collision dynamics, Int. J. Heat Mass Transfer 47 (2004) 4649-4657.

[63] B. Sakakibara, T. Inamuro, Lattice Boltzmann simulation of collision dynamics of two unequal-size droplets, Int. J. Heat Mass Transfer 51 (2008) 3207-3216.

[64] Z. Sun, G. Xi, X. Chen, Mechanism study of deformation and mass transfer for binary droplet collisions with particle method, Phys Fluids 21 (2009) 032106.

[65] X. Chen, D. Ma, P. Khare, V. Yang. Energy and mass transfer during binary droplet collision. Proceedings of 49th AIAA Aerospace Sciences Meeting Including the New Horizons Forum and Aerospace Exposition; 2011. p.

[66] D. Zhang, C. He, P. Zhang, C. Tang, Mass Interminglement and Hypergolic Ignition of TMEDA and WFNA Droplets by Off-center Collision, Combust. Flame (under revision).

[67] D. Zhang, P. Zhang, Y. Yuan, T. Zhang, Hypergolic ignition by head-on collision of N, N, N′ , N′ − tetramethylethylenediamine and white fuming nitric acid droplets, Combust Flame 173 (2016) 276-287.

[68] S. Popinet, Gerris: a tree-based adaptive solver for the incompressible Euler equations in complex geometries, J. Comput. Phys. 190 (2003) 572-600.

[69] S. Popinet, An accurate adaptive solver for surface-tension-driven interfacial flows, J. Comput. Phys. 228 (2009) 5838-5866.

[70] X. Chen, D. Ma, P. Khare, V. Yang. Energy and mass transfer during binary droplet collision. 49th AIAA Aerospace Sciences Meeting Including the New Horizons Forum and Aerospace Exposition; 2011. p. 771.

[71] X. Chen, V. Yang, Thickness-based adaptive mesh refinement methods for multi-phase flow simulations with thin regions, J. Comput. Phys. 269 (2014) 22-39.

[72] S. Popinet, Numerical Models of Surface Tension, Annu. Rev. Fluid Mech. 50 (2018) 1-28.

[73] S. Tanguy, A. Berlemont, Application of a level set method for simulation of droplet collisions, Int. J. Multiphase Flow 31 (2005) 1015-1035.

[74] S.-I. Yeh, W.-F. Fang, H.-J. Sheen, J.-T. Yang, Droplets coalescence and mixing with identical and distinct surface tension on a wettability gradient surface, Microfluidics and nanofluidics 14 (2013) 785-795.

[75] L. Liou, J.W. Dankanich, L.L. Alexander. NASA in-space advanced chemical propulsion development in recent years. IEEE Aerospace Conference, Big Sky, MT; 2010.

[76] A. Musker, J. Rusek, C. Kappenstein, G. Roberts, Hydrogen peroxide-from bridesmaid to bride, (2006).

[77] H. Kang, J. Won, S.W. Baek, S. Kwon, Autoignition and combustion characteristics of sodium borohydride-based non-toxic hypergolic fuel droplet at elevated temperatures, Combust Flame 181 (2017) 149-156.

[78] J. Yamamoto, Sodium borohydride digest, Rohm and Haas, USA, (2003).

[79] B.V.S. Jyoti, M.S. Naseem, S.W. Baek, H.J. Lee, S.J. Cho, Hypergolicity and ignition delay study of gelled ethanolamine fuel, Combust Flame 183 (2017) 102-112.

[80] B. Jyoti, M.S. Naseem, S.W. Baek, Hypergolicity and ignition delay study of pure and energized ethanol gel fuel with hydrogen peroxide, Combust Flame 176 (2017) 318-325.

[81] R.P. Chhabra, Bubbles, drops, and particles in non-Newtonian fluids, CRC press2006.

[82] H. Liu, Science and Engineering of Droplets:: Fundamentals and Applications, William Andrew, 1999.

[83] C. Focke, D. Bothe, Computational analysis of binary collisions of shear-thinning droplets, J Non-Newton Fluid 166 (2011) 799-810.

[84] M. Motzigemba, N. Roth, D. Bothe, H. Warnecke, J. Prüss, K. Wielage, B. Weigand, The effect of non-Newtonian flow behaviour on binary droplet collisions: vof-simulation and experimental analysis, Zaragoza 9 (2002) 11.